# Zirconium carbide (ZrC) synthesised via chemical vapour deposition (CVD) and spark plasma sintering (SPS) and phase formation of iridium (Ir) films deposited on ZrC at relatively low temperatures

By

**Bilal Abbas Bilal Alawad**

A thesis submitted in fulfilment of the requirements for the degree of

**DOCTOR OF PHILOSOPHY (PHD) IN PHYSICS**

Faculty of Natural and Agricultural Sciences

University of Pretoria

Hatfield Pretoria

December 2019

**Supervisor: Prof. J. B. Malherbe**

**Co-Supervisor: Prof. P.L. Crouse**

**Co-Supervisor: Dr. H. Bisset**

**Co-Supervisor: Prof. T. T. Hlatshwayo**

**Co-Supervisor: Dr.E. G. Njoroge**

## Declaration

I, hereby declare that the matter embodied in this thesis entitled “Zirconium carbide (ZrC) synthesised via chemical vapour deposition (CVD) and spark plasma sintering (SPS) and phase formation of an iridium (Ir) films on ZrC at relatively low temperatures” is the result of investigations carried out by me under the supervision of Prof. J. B. Malherbe, in the Physics Department at the University of Pretoria South Africa and that it has not been submitted elsewhere for the award of any degree or diploma. In keeping with the general practice in reporting scientific observations, due acknowledgement has been made whenever the work described is based on the findings of other investigators.

Signature: BAB Alawad Date: 5 December 2019

# Summary


**Zirconium carbide (ZrC) synthesised via chemical vapour deposition (CVD) and spark plasma sintering (SPS) and phase formation of iridium (Ir) films deposited on ZrC at relatively low temperatures.**

**By**

**Bilal Abbas Bilal Alawad**

Submitted in partial fulfilment of the requirements for the degree of (PhD) in Physics in the Faculty of Natural and Agricultural Science, University of Pretoria.

Supervisor/Promoter: Prof. J. B. Malherbe
Co-supervisors: Prof. P. L. Crouse
Dr. H. Bissett
Prof. T. T. Hlatshwayo
Dr. E. G. Njoroge

High temperature gas cooled reactors (HTGRs) such as the pebble bed modular reactor (PBMR) is a suitable candidate which uses the tri-structural isotropic (TRISO) particles for containment of radioactive fission products. In the TRISO particles silicon carbide (SiC) is the main barrier for containing solid fission products. Zirconium carbide (ZrC) is a candidate material to act as an additional layer or replace the SiC layer of the TRISO particle. This is due to ZrC being a better barrier than SiC against the diffusion of Ag and also being more resistant against palladium attack. ZrC also has excellent physical properties such as low neutron capture cross section, good thermal shock resistance, excellent thermal stability, etc. However these properties rely on a

number of factors such as microstructure, morphology, chemical composition, hardness, densification, the presence of impurities, etc. Many studies have been used to grow ZrC layers. However, to growth high quality of polycrystalline ZrC layers with good stoichiometry has remained a challenge. This study will focus on two methods for manufacturing ZrC; (1) designing a chemical vapour deposition (CVD) reactor, (2) spark plasma sintering (SPS) for growing ZrC layers and studying the properties of ZrC layers grown under different conditions.

ZrC has a high affinity for oxygen and due to this property; it can be used as an oxygen getter in uranium oxide TRISO fuel particles when added as a protective layer on SiC. Oxidation of ZrC starts at temperatures close to 277 °C in lower oxygen partial pressure (1-50 kPa) environments, while significant oxidation has been observed at temperatures above 600 $^{o}$C at atmospheric pressure. In the case where the ZrC layer replaces the SiC layer as the main diffusion barrier, then it would have to be protected from oxidation since oxidation may affect its integrity.

The oxidation of ZrC can be reduced by adding an iridium (Ir) layer on ZrC. Iridium has a high oxidation resistance. Its corrosion resistance is higher than all metals and it has a high melting point of 2443 °C. Ir can react with oxygen to form iridium dioxide at a temperature of 1800 °C, which is higher than the operating temperature of HTGRs. HTGRs operate at temperatures between 950 °C and 1350 °C, Ir at these operating temperatures is not expected to react with oxygen, thus making it attractive for use as a protective layer for ZrC against oxidation at high temperatures.

In this study zirconium carbide (ZrC) layers were deposited on graphite substrates using a $ZrCl_4$+$CH_4$+$H_2$ and Ar gas mixture in a CVD reactor at temperatures ranging from 1250 °C to 1450 °C in steps of 50 °C. The deposited layers were characterised by X-ray diffraction (XRD), Raman Spectroscopy and Scanning Electron Microscopy (SEM). The deposition rate

exponentially increased with increasing temperature and its activation energy showed that the deposition mechanism was controlled by surface reactions. The XRD patterns together with a Rietveld analysis showed that the layers consisted of ZrC with graphite and carbon inclusions in the layers. Raman spectroscopy showed that the graphite was highly disordered. In contrast to the ZrC lattice parameter which remained constant at 0.46838 ± 0.00091 nm, the average sizes of ZrC crystallites (and the graphite crystallites) depended on the deposition temperature and varied between 19.90 nm to 26.18 nm for the ZrC grains and 22.50 nm to 34.5 nm for the graphite grains inclusions. The texture coefficients of the (111), (200) and (220) planes showed that at all deposition temperatures (i.e. from. 1250 $^{o}$C to 1400 $^{o}$C), all three planes showed preferred orientation. At 1450 $^{o}$C only the (220) plane grew preferentially. SEM showed that the morphology of the as-deposited layers was influenced by the deposition temperature. Clustering of the crystals occurred, resulting in a cauliflower appearance on the surface.

In this study zirconium carbide (ZrC) samples were also prepared by spark plasma sintering (SPS), at temperatures of 1700 °C, 1900 °C and 2100 °C at 50 MPa for 10 minutes. The phase and microstructure after the sintering process was investigated. The relative density of ZrC ceramic pellets formed at 1700 °C, 1900 °C and 2100 °C was measured and found to be 96.5 %, 98.9 % and 99.5 % respectively. The grain size of ZrC ceramic pellets was calculated and it was found to increase from 71.88 nm, 79.15 nm and 83.59 nm as the sintering temperature increased from 1700 $^{o}$C, 1900 $^{o}$C to 2100 $^{o}$C respectively. The hardness of ZrC ceramic pellets was found to be 7.40 GPa, 17.00 GPa to 18.40 GPa at 1700 $^{o}$C, 1900 $^{o}$C to 2100 $^{o}$C respectively. The preferred orientation of ZrC ceramic at 1700 $^{o}$C, 1900 $^{o}$C and 2100 $^{o}$C was the (200) plane. Iridium (Ir) thin films were deposited on ZrC ceramics by electron beam deposition method and annealed in vacuum at temperatures of 600 °C and 800 °C for 2h. The phase composition, solid-

state reactions and surface morphology were investigated by grazing incidence X-ray diffraction (GIXRD), and scanning electron microscopy (SEM). XRD was used to identify the phases present in the as-deposited and annealed samples. XRD analysis showed that $Ir_2Zr$ was the initial phase formed at 600 °C. At temperature 800 °C, Ir reacted with the ZrC to form IrZr. The SEM images of as-sintered samples at 1700 $^{o}$C, 1900 $^{o}$C and 2100 $^{o}$C showed that the ZrC surface was heterogeneous and uneven consisting of agglomerated granules with a few pores. The number of pores was observed to reduce with sintering temperature. After depositing Ir films on ZrC substrate, the structure of the Ir film followed that of the substrates. After annealing the Ir-ZrC samples at 600 $^{o}$C and 800 $^{o}$C, the further agglomeration of surface granules was observed.

# Acknowledgements

I would like to express my endless heartfelt gratitude to my promoter, Prof. JB. Malherbe for his unconditional patience, support and encouragement. I appreciate his determined supervision, invaluable suggestions, critical comments and cautions. Also my gratefulness goes to my co-supervisors Prof PL. Crouse, Dr. H. Bissett, Dr. E. G. Njoroge and Dr. TT. Hlatswayo for their endless support and scientific guidance which made this work to be this shape.

I would also like to acknowledge the assistance from colleagues and staff at Necsa (Applied Chemistry Division), Tshwane University of Technology (TUT) and University of Pretoria (Department of Physics and Department of Chemical Engineering).

This PhD study program was generously supported by funds from University of Pretoria and Sudan University of Science and Technology to whom I am exceedingly grateful.

Not forgetting my family for their constant love and support, especially my wife Hala, sons Mohammed, Monzer and daughter Marim, for being patient and their sacrifices. This thesis is dedicated to them.

I thank Allah who made all these possible.

# Table of Contents

# List of Tables

# List of Figures

# Chapter 1. General Introduction

## 1.1 Background

The next generation of nuclear reactors would need to have a higher degree of safety and efficiency. In a modern high temperature gas cooled reactors (HTGRs) such as the pebble bed modular reactor (PBMR) safety and efficiency are improved by the use of tri-structural isotropic (TRISO) particles as the nuclear fuel containing unit. A schematic diagram of the typical coated TRISO fuel particle is shown in Figure 1-1.

The basic design includes a fuel kernel of either uranium oxide ($UO_2$) or uranium carbide covered with four layers. The first inner layer is a porous, low-density buffer layer composed of carbon whose main functions include attenuating fission products (FPs) recoils and providing expansion volume for fission gases. The second layer is the inner pyrolytic carbon (IPyC) layer. This layer provides a base for silicon carbide (SiC) and during operation it can retain gaseous FPs and help keep the SiC layer in compression. The third layer is the SiC layer which lies between IPyC and outer pyrolytic carbon (OPyC), which provides structural support for the fuel particle and is the primary barrier against FPs release. The OPyC layer compresses the SiC layer and provides a final barrier against the release of gaseous fission products[1,2]. The fuel kernel is 0.5 mm in diameter, the buffer layer is 95 μm thick, IPyC and OPyC are each 40 μm thick and the SiC is 35μm thick [1].

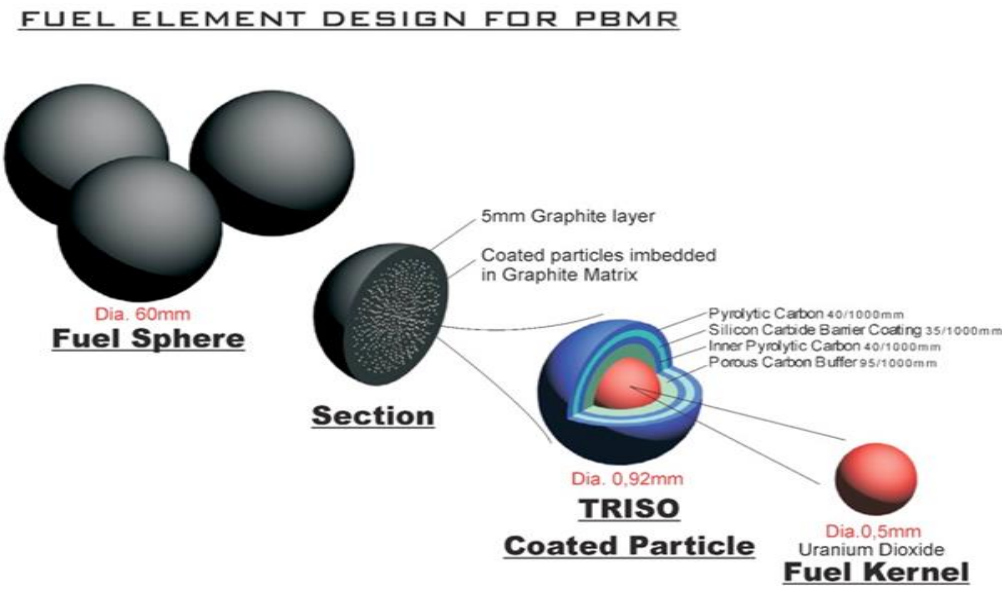


*Figure 1-1: Schematic diagram of the TRISO coated fuel particle for the pebble bed modular reactor*[3].

HTGRs operate at temperatures of about 950 °C [4]. During normal operation conditions, the SiC layer in the TRISO particle retains most of the important FPs with the exception of silver (Ag), strontium (Sr) and Europium (Eu) [2,5]. Palladium which is also a FP has been reported to attack the SiC layer leading to the formation of nodules of palladium silicides. The formation of the palladium silicides leads to the thinning of the SiC layer and assists in the release of silver through SiC layer [6]. Therefore, these affect the integrity of SiC to act as the main diffusion barrier in TRISO particles [7].

ZrC has been suggested as an additional layer to SiC or as a material to replace SiC in the TRISO fuel system [2]. This is because ZrC is a better diffusion barrier against FPs such as Ag compared to SiC and it is significantly more resistant to Pd attack [8,9].

## 1.2 Zirconium carbide (ZrC)

Zirconium carbide (ZrC) is a group IV transition metal carbide with a NaCl structure where the Zr or C atoms have a face centered cubic (fcc) close packed structure[10] as seen in

Figure1-2. Its appearance is dark-grey in colour with a lattice parameter of about 4.698 Å reported in ref. [10]. ZrC is thermally stable with very low vapour pressure but decomposes at very high temperatures of about 3420 $^{o}$C [10].Compared to other carbides like tungsten carbide (WC) which has density of 15.8 g/cm$^3$, titanium carbide (TiC) with a density of 4.91 g/cm$^3$ and hafnium carbide (HfC) with a density of 12.67 g/cm$^3$, ZrC has a relatively low density of 6.59 g/cm$^3$[10]. ZrC also has relatively low Vickers Hardness of 25.5 GPa compared to HfC which has a Vickers Hardness of 26.1 GPa, and TiC which has a Vickers Hardness of around 28-35 GPa [10]. Table 1-1lists additional physical properties of ZrC as reported in ref.[10].

ZrC has several applications in industry such as: (a) thermo-photovoltaic radiators and field emitter tips and arrays, (b) as a diffusion barrier for fission products for nuclear fuel TRISO particle, (c) as a cutting and drilling tool material and as a wear resistant coating etc.

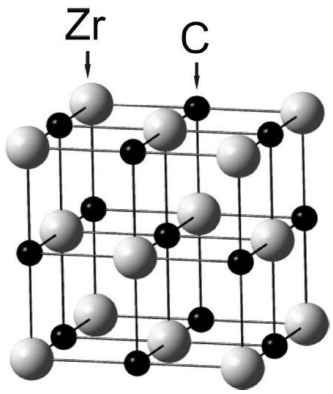


*Figure1-2: The NaCl (rock salt) structure of ZrC. Taken from*[11].

Due to the properties mentioned above, ZrC can be used as replacement for SiC coatings in TRSIO particles. The reasons for selecting ZrC reported in ref.[12] are; (a) it has a higher melting temperature stability compared to silicon carbide (3540 $^{o}$C versus 2700 $^{o}$C), (b) ZrC has been found to have better resistance to chemical attack than silicon carbide, (c) ZrC has a

low neutron capture cross section compared with silicon carbide, (d) ZrC has good thermal shock resistance, relatively low density, excellent thermal stability and high hardness [13].The properties of ZrC depend on a number of factors such as chemical composition, crystallite size, morphology, orientation of crystal planes, structural defects, porosity, and the presence of impurities[14]. These factors are a function of the methods and conditions used in growing ZrC coatings. Two methods were used in this study to produce ZrC. The first method is chemical vapour deposition (CVD) which produces layers with very low levels of impurities and low porosity[15], which are reasons why it is the preferred method.

*Table 1-1: Characteristics and properties of ZrC. Taken from* [10].

| **Properties** | **Quantity** |
|---|---|
| Structure | Cubic closed pack (FCC) |
| Colour | Silver gray, Gray |
| Space group | Fm3m |
| Composition | $ZrC_{0.55}$ to $ZrC_{0.99}$ |
| Density ($g/cm^3$) | 6.59 |
| Melting temperature (°C) | 3420 |
| Hardness | 25.5 GPa Vickers hardness |
| Thermal conductivity | 20.5 W/m °C |
| Thermal expansion (°C) | $6.7\times10^{-6}$/°C |
| Electrical resistivity (μΩ cm) | 45±10 |
| Modulus of elasticity | 350 – 440 GPa |
| Magnetic susceptibility | $-23\times10^{-6}$ emu/mol |

Compared to SiC, few authors have published on the use of ZrC in the nuclear reactor environment. The main reason is probably that SiC has proven nuclear applications and other desirable physical properties such as a wide band gap semiconductor [14]. Another reason for this might be that it is difficult to grow good quality ZrC layers.

The second method is spark plasma sintering (SPS). This is an effective technique for preparing dense ZrC ceramics. During SPS, the rapid and thorough heat distribution throughout the specimen generated from the high frequency transformation and dispersion of the spark/Joule heat makes it possible to densify the materials at a low temperature and in a short time interval [16]. Various precursors can be used to synthesis ZrC ceramic by SPS. Sun et al. [16] reported on the preparation of ZrC by reactive spark plasma sintering using zirconium oxide and carbon black. According to reaction in equation (1.1) $ZrO_2$ and carbon black with a molar ratio of 1:3 were mixed by rolling ball milling for 24 hours. The slurry was then dried in a rotary evaporator at 80 $^{o}$C:

$$ZrO_2 + 3C \rightarrow ZrC + 2CO \qquad (1.1)$$

Sciti et al. [17] also reported on the microstructures and mechanical properties of dense ZrC composites. ZrC powders were used as raw materials sintered by SPS method at 2100 $^{o}$C for 3 min in a vacuum under an applied pressure of 65 MPa. However, a relatively high sintering temperature may still be required for ZrC densification using the SPS method[16].

### 1.3 Iridium (Ir)

Much effort has been put in controlling the oxidation of carbon structures by the use of protective coatings. Therefore, to perform this function, the protective coatings must have low volatility, be chemically stable and mechanically compatible with the ceramic material e.g. zirconium carbide [18]. Furthermore, the protective coatings must inhibit the diffusion of oxygen to the substrate and the diffusion of carbon through the coatings. These protective coatings can applied as either a single layer or multilayer coating[18].

Iridium can be used as crucible material for the growth of single crystals. Ir has considerable advantages such as, ahigh melting point of 2447 $^{o}$C, low oxygen permeability, good chemical

compatibility and superior oxidation resistance[18].Table 1-2 gives a summary of additional physical and electrical properties of Ir.

Ir is one of the most promising candidates for use as protective coating for structural ceramic materials such as ZrC against extreme environments [18]. Ir is used in many applications such as a barrier layer on structural carbon materials [19], re-rocket thrusters, heavy-metal-ion sensors, and patterned thin-film microelectrodes [20].Ir protective films or coatings can be prepared by several deposition methods such as chemical vapour deposition (CVD) [21], magnetron sputtering (MS)[22] and double glow plasma (DGP)[23]. In this study, electron beam deposition (EBD) was used and discussed in chapter 4 in detail.

*Table 1-2: Properties of iridium.*

| **Properties** | **Quantity** | **References** |
|---|---|---|
| Melting point | 2447ºC | [18] |
| Oxygen permeability | $10^{-14}$ g $cm^{-1}s^{-1}$ (2200ºC) | [24] |
| Density | 22.65 $g/cm^3$ | [24] |
| Vickers hardness | 3.2 GPa | [25] |
| Thermal expansion coefficient | ~$6.2 \times 10^{-6}$ $ºC^{-1}$ | [26] |
| Thermal conductivity (0–100ºC) | 1.48 J $cm^{-1}$ $s^{-1}$ $ºC^{-1}$ | [27] |
| Specific heat (0–100ºC) | 0.134 J $g^{-1}$ $ºC^{-1}$ | [27] |
| Electrical resistivity | 5.1 μΩ cm | [28] |
| Young's modulus | 524 GPa | [29] |
| Tensile strength (annealed), 20ºC | 490–740 MPa | [27] |
| Poisson ratio | 0.26 | [27] |

Strife et al. [30] investigated the reactions between Ir and metal carbides at high temperatures, viz. between 1650 $^oC$ and 2127 $^oC$ at inert atmosphere (argon).They reported that the interaction between zirconium carbide and iridium coatings deposited by chemical vapour deposition can be predicted from available thermodynamic data in the temperature

range of 1650 $^{o}$C and 2127 $^{o}$C. From the standard free energies, they stated that the $ZrIr_3$ compound formation was favoured.

Criscione et al. [31]investigated the reactions between Ir and zirconium carbide structures under varying high temperature conditions between 1200 $^{o}$C to 2200 $^{o}$C at helium gas pressure of up to 670 mmHg. Thermal annealing of zirconium carbide and iridium resulted in the formation of the $ZrIr_3$intermetallic phase. The results showed that, when Ir-ZrC contacts were heated at temperature1200 $^{o}$C, a reaction occurred given as:

$$3Ir(s) + ZrC(s) \rightarrow ZrIr_3(s) + C(s) \qquad (1.2)$$

No studies have been reported on the reaction between Ir and ZrC at lower temperatures (below 1000 °C). Therefore, part of this study will focus on the interaction between Ir and ZrC at temperatures ranging from 600 $^{o}$C to 800 $^{o}$C annealed in vacuum.

### 1.4 Research Motivation

ZrC either as a powder mixed with the fuel or as a thin layer on the fuel kernel has been proposed for use as an oxygen getter in the $UO_2$ kernel TRISO fuel. The high oxidation potential of ZrC (above room temperature) is perceived to act as a reducing agent for the oxygen generated from the fission process of $UO_2$. This avoids unfavourable oxidation reactions and reduces the formation of CO which are very detrimental more especially at high fuel burn-up levels.

Therefore, ZrC has a high affinity for oxygen, therefore, it can be used as an oxygen getter in uranium oxide based TRISO fuel particles when added as a protective layer on SiC [15]. Oxidation of ZrC starts at temperatures close to 277 °C in low oxygen partial pressure (1-50 kPa) environments, while significant oxidation has been observed at temperatures above 600 $^{o}$C at atmospheric pressure [15].

In the case where the ZrC layer replaces the SiC layer as the main diffusion barrier, it would have to be protected from oxidation since this may affect its integrity. The oxidation of ZrC can be hindered by adding an iridium (Ir) layer on ZrC. Iridium has a high oxidation resistance [32], Iridium exhibits the highest resistance to corrosion in molten oxides among metals [33]and has a high melting point as mentioned above in section 1.3.

Iridium is impervious to oxygen diffusion at temperatures of up to 1900 °C [34], which is higher than the operating temperature of HTGRs which is 950 °C [4]. This makes Ir attractive for use as a protective layer for ZrC against oxidation at high temperatures in TRISO nuclear fuel applications.

Since iridium does not react with oxygen at the operating temperatures of the HTGRs, it can be considered an excellent barrier to oxygen. Therefore, coating the ZrC layer with iridium could be a solution to the protection of the ZrC layer against the oxidation and thinning. The performance of the Ir protective layer on ZrC depends greatly on the stability of Ir-ZrC interface.The only limitation of using the Ir protective layers is the possibility of reactions between Ir and ZrC. If interactions occur at this interface, they can result in the protective layer failure and ultimately lead to TRISO particle failure. Solid-state reactions occurring at the Ir-ZrC interface and the resulting structures at the interface are important performance determining factors in Ir-ZrC contacts. It is therefore essential to understand the mechanism of material stability and reactivity at this interface.

Therefore, is important to investigate the stability and interactions between Ir protective layers and ZrC at different annealing temperatures. The results from this investigation will assist in determining the lowest temperature at which the material (Ir-ZrC) will start reacting and it will also assist in determining the temperature at which this material degrades.

## 1.5 Research Objectives and Aims

- To develop a deposition process for the growth of ZrC layers from Zirconium tetrachloride ($ZrCl_4$), methane ($CH_4$), hydrogen ($H_2$) and argon (Ar) precursors using induction thermal CVD at atmospheric pressure., with the following objectives:
  - To synthesis and develop a laboratory scale CVD system to produce ZrC layers of various stoichiometry at temperature from 1250 °C to 1450 °C.
  - To investigate the composition and microstructure of the ZrC layers deposited as a function of the input variables.
- To investigate ZrC ceramics synthesised by spark plasma sintering (SPS) at different temperatureswith the following objective:
  - To investigate the composition and microstructure of the ZrC layers deposited as a function of the input variables.
- To investigate possible interactions between Ir thin films and ZrC substrate at a lower temperature range of 600 °C to 800 °C in vacuum.
  - The temperature range was chosen in order to identify the possible interaction and structural changes at the temperature of application for TRISO particles in a nuclear reactor.

## 1.6 Thesis Outline

This thesis consists of 7 chapters and the outline is structured as follows: chapter 1 is the background which gives general information on TRISO-SiC, TRISO-ZrC, properties of ZrC and Ir. Chapter 2 discusses the chemical vapour deposition (CVD) and spark plasma sintering (SPS), which are techniques that were used for prepared ZrC in this study. In Chapter 3, the thermodynamic properties which include the Zr-C, Ir-C, Ir-Zr phase diagrams are discussed. Chapter 4 discusses the sample preparation by CVD, SPS and electron beam deposition techniques. Chapter 5 discusses analytical techniques used for the sample analysis. The

results are discussed in chapter 6. Conclusions are drawn from the above studies and the recommended future work are given in chapter 7.

## References


[1] N.G. Van Der Berg, J.B. Malherbe, A.J. Botha, E. Friedland, SEM analysis of the microstructure of the layers in triple-coated isotropic ( TRISO ) particles, Surf. Interface Anal. 42.6–7 (2010) 1156–1159.

[2] J.B. Malherbe, Diffusion of fission products and radiation damage in SiC, J. Phys. D. Appl. Phys. 46 (2013) 1–27.

[3] Fuel element design for PBMR, (n.d.). http://www.pbmr.co.za/contenthtml/files/Image/HowFuelLarge.jpg (accessed February 26, 2014).

[4] K. Sawa, S. Ueta, T. Iyoku, Research and development program of HTGR fuel, in: IAEA Tech. Meet. Curr. Status Futur. Prospect. Gas Cool. React. Fuels, Vienna, 2009: pp. 208–218.

[5] S.S. Dwaraknath, G.S. Was, The diffusion of cesium, strontium, and europium in silicon carbide, J. Nucl. Mater. 476 (2016) 155–167. doi:10.1016/j.jnucmat.2016.04.034.

[6] J.H. Neethling, J.H. O'Connell, E.J. Olivier, Palladium assisted silver transport in polycrystalline SiC, Nucl. Eng. Des. 251 (2012) 230–234.

[7] E. Friedland, J.B. Malherbe, N.G. van der Berg, T. Hlatshwayo, A.J. Botha, E. Wendler, W. Wesch, Study of silver diffusion in silicon carbide, J. Nucl. Mater. 389 (2009) 326–331.

[8] X.W. Zhou, C.H. Tang, Current status and future development of coated fuel particles for high temperature gas-cooled reactors, Prog. Nucl. Energy. 53 (2011) 182–188.

[9] K. Sawa, S. Ueta, Research and development on HTGR fuel in the HTTR project, Nucl. Eng. Des. 233 (2004) 163–172.

[10] H.O. Pierson, Handbook of Refractory Carbides and Nitrides: Properties, Characteristics, Processing and Applications, Noyes Publications, Park Ridge, New Jersey, 1996.

[11] S. Kim, I. Szlufarska, D. Morgan, Ab initio study of point defect structures and

energetics in ZrC, J. Appl. Phys. 053521 (2012).

[12] G.H. Reynolds, J.C. Janvier, J.L. Kaae, J.P. Morlevat, Irradiation behavior of experimental fuel particles containing chemically vapor deposited zirconium carbide coatings, J. Nucl. Mater. 62 (1976) 9–16.

[13] Y.S. Won, V.G. Varanasi, O. Kryliouk, T.J. Anderson, L. McElwee-White, R.J. Perez, Equilibrium analysis of zirconium carbide CVD growth, J. Cryst. Growth. 307 (2007) 302–308.

[14] S. Biira, Construction of a chemical vapour deposition reactor and the deposition of ZrC layers, PhD thesis, University of Pretoria, 2017.

[15] Y. Katoh, G. Vasudevamurthy, T. Nozawa, L.L. Snead, Properties of zirconium carbide for nuclear fuel applications, J. Nucl. Mater. 441 (2013) 718–742.

[16] S.K. Sun, G.J. Zhang, W.W. Wu, J.X. Liu, T. Suzuki, Y. Sakka, Reactive spark plasma sintering of ZrC and HfC ceramics with fine microstructures, Scr. Mater. 69 (2013) 139–142.

[17] D. Sciti, S. Guicciardi, M. Nygren, Spark plasma sintering and mechanical behaviour of ZrC-based composites, Scr. Mater. 59 (2008) 638–641.

[18] W.U. Wangping, C. Zhaofeng, Ir Protective Coatings for Carbon Structural Materials, J. Wuhan Univ. Technol. Sci Ed. 27 (2012) 652–656.

[19] N.I. Baklanova, N.B. Morozova, V. V Kriventsov, A.T. Titov, Synthesis and microstructure of iridium coatings on carbon fibers, Carbon N. Y. 56 (2013) 243–254.

[20] S. Kohli, D. Niles, C.D. Rithner, P.K. Dorhout, Structural and optical properties of Iridium films annealed in air, JCPDS-International Cent. Diffr. Data, Adv. X-Ray Anal. 45 (2002) 352–358.

[21] J.R.V. Garcia, T. Goto, Chemical vapor deposition of iridium, platinum, rhodium and palladium, Mater. Trans. 44 (2003) 1717–1728.

[22] M.A. El Khakani, M. Chaker, B. Le Drogoff, Iridium thin films deposited by radio-frequency magnetron sputtering, J. Vac. Sci. Technol. A. 16 (1998) 885–888.

[23] Z.F. Chen, W.P. Wu, X.N. Cong, L.B. Wang, Study on Iridium Coating Produced by Double Glow Plasma, Adv. Mater. Res. 314–316 (2011) 214–218.

[24] Z.F. Chen, W.P. Wu, L.B. Wang, Y. Zhang, Microstructure and analytic equation of conical aggregate in iridium coating prepared by double glow plasma, Surf. Eng. 27 (2011) 242–245.

[25] M.B. Weinberger, J.B. Levine, H.-Y. Chung, R.W. Cumberland, H.I. Rasool, J.-M. Yang, R.B. Kaner, S.H. Tolbert, Incompressibility and Hardness of Solid Solution

Transition Metal Diborides: Os1- x Ru x B2, Chem. Mater. 21 (2009) 1915–1921.

[26] W. Wu, X. Lin, Z. Chen, Z. Chen, X. Cong, T. Xu, J. Qiu, Microstructural characterization and mechanical property of iridium coating produced by double glow plasma, Plasma Chem. Plasma Process. 31 (2011) 465–475.

[27] L.B. Hunt, A history of iridium, Platin. Met. Rev. 31 (1987) 32–41.

[28] Y. Ritterhaus, T. Hur'yeva, M. Lisker, E.P. Burte, Iridium Thin Films Deposited by Liquid Delivery MOCVD using Ir (EtCp)(1, 5-COD) with Toluene Solvent, Chem. Vap. Depos. 13 (2007) 698–704.

[29] S.S. Hecker, D.L. Rohr, D.F. Stein, Brittle fracture in iridium, Metall. Trans. A. 9 (1978) 481–488.

[30] J.R. Strife, J.G. Smeggil, W.L. Worrell, Reaction of Iridium with Metal Carbides in the Temperature Range of 1923 to 2400 K, J. Am. Ceram. Soc. 73 (1990) 838–845.

[31] J.M. Criscione, R.A. Mercuri, E.P. Schram, A.W. Smith, H.F. Volk, High temperature protective coatings for graphite: Part II, Wright Patterson AFB, OH, 1964.

[32] W. Wu, Z. Chen, X. Lin, B. Li, X. Cong, Effects of bias voltage and gas pressure on orientation and microstructure of iridium coating by double glow plasma, Vacuum. 86 (2011) 429–437.

[33] W. Wu, Z. Chen, Iridium Coating: Processes, Properties and Application. Part I, Johnson Matthey Technol. Rev. 61 (2017) 16–28.

[34] D.E. Wright, T R, Weyand, J. D., And Kizer, Iridium Coatings for the Protection of Graphite Re-Entry Structures, in: Sp. Congr. Proc., 1967: pp. 45–54.

# Chapter 2. ZrC layers deposition by CVD and SPS techniques

The properties of ZrC depend on the technique and conditions used to manufacture ZrC. In this thesis chemical vapour deposition (CVD) and spark plasma sintering (SPS) techniques were used to manufacture ZrC. This chapter discus the CVD and SPS processes together with conditions of manufacturing ZrC.

## 2.1 Thin film deposition methods

The properties of thin films depend on the deposition techniques and parameters under which they are being deposited [1]. This study has been focused to describe and understand both the different methods of film deposition as well as the methods available for analysis and characterisation of films. The techniques used for the deposition of films include physical vapour deposition (PVD), Low-pressure CVD (LPCVD), Metalorganic CVD (MOCVD), Atmospheric-pressure CVD (APCVD), Laser-induced CVD (PCVD), Electron-enhanced CVD, chemical vapour deposition (CVD) etc., as listed in Table 2-1 [2,3]. Among these techniques, PVD and CVD are the two techniques that have been widely used to synthesise films from the vapour or the gaseous phase. However, CVD has been preferred since it produces films of superior quality as compared to PVD [2]. Therefore, this chapter will discuss the CVD and SPS techniques used in this study to synthesise ZrC layers. The techniques that were used in this study to analyse and characterise ZrC films are discussed in Chapter 4.

## 2.2 Chemical Vapour Deposition (CVD) technique

CVD of thin films and coatings include the chemical reactions of gaseous reactants on or near the vicinity of a heated substrate surface [4]. Volatile inorganic, metal-organic, or organometallic precursors in CVD process are transported through the vapour carrier gas to

the reaction chamber, where they decompose, on a heated substrate and subsequently deposit a solid film**.** After the deposition, the volatile by products are eliminated as shown in Figure (2-1) [5].

*Table 2-1: Survey and classification of thin film deposition techniques. Taken from [2].*

| **Glow discharge processes** | |
|---|---|
| **Sputtering**<br>Diode sputtering<br>Reactive sputtering<br>Bias sputtering (ion plating)<br>Magnetron sputtering<br>Ion beam deposition<br>Ion beam sputter deposition<br>Reactive ion plating<br>Cluster beam deposition (CBD) | **Plasma Processes**<br>Plasma-enhanced CVD<br>Plasma oxidation<br>Plasma anodization<br>Plasma polymerization<br>Plasma nitridation<br>Plasma reduction<br>Microwave ECR plasma CVD<br>Cathodic arc deposition |
| **Gas phase chemical processes** | |
| **Chemical Vapor Deposition (CVD)** | **Thermal Forming Processes** |
| CVD epitaxy<br>Atmospheric-pressure CVD (APCVD)<br>Low-pressure CVD (LPCVD)<br>Metalorganic CVD (MOCVD)<br>Photo-enhanced CVD (PHCVD)<br>Laser-induced CVD (PCVD)<br>Electron-enhanced CVD | Thermal oxidation<br>Thermal nitridation<br>Thermal polymerization<br><br><br><br>Ion implantation |
| **Liquid phase chemical techniques** | |
| **Electro Processes** | **Mechanical Techniques** |
| Electroplating<br>Electroless plating<br>Electrolytic anodization<br>Chemical reduction plating<br>Chemical displacement plating<br>Electrophoretic deposition | Spray pyrolysis<br>Spray-on techniques<br>Spin-on techniques<br><br><br>Liquid phase epitaxy |

According to the characteristics of the CVD processing parameters, CVD methods are generally classified into seven main types of fabrication, as illustrated in Figure 2-2. The parameters used to characterise a CVD process involve temperature, pressure, wall/substrate

temperature, precursor nature, depositing time, gas flow state and activation method[6]. CVD can also be classified using activation methods. The processes of thermal activated CVD are initiated only with the thermal energy of resistance heating, RF induction heating or by infrared radiation. In some cases enhanced CVD methods are employed, which includes plasma-enhanced CVD (PECVD), laser induced CVD (LCVD), photo CVD (PCVD), catalysis-assisted CVD, etc. In a plasma-enhanced CVD process the plasma is used to activate the precursor gas, which significantly decreases the deposition temperature[6].The CVD technique is complicated but it is the preferred technique of growing good layers and coating compared to other methods such as PVD. CVD can produce pure uniform layers and which are reproducible at relatively good deposition rates [2].

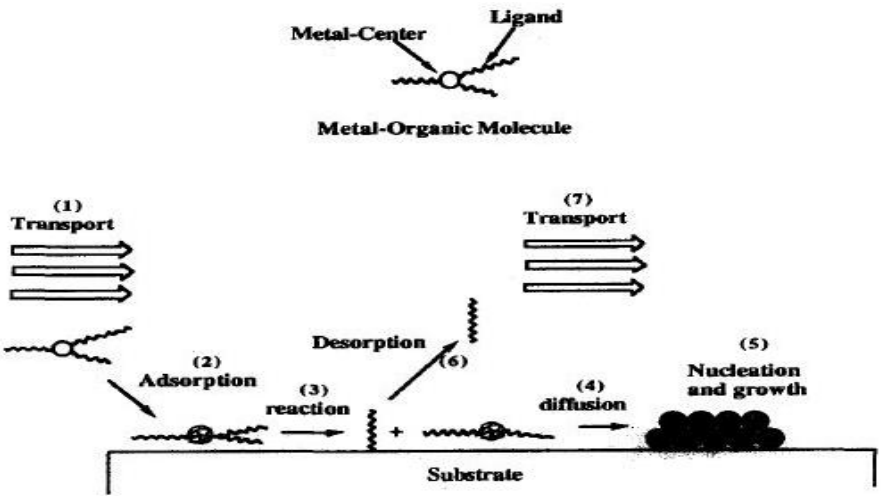


*Figure 2-1: The fundamental steps involved in the CVD of a metal-organic molecule. Taken from [5].*

This study focuses on the operation and deposition processes of the thermal CVD reactor. Thermal CVD reactor should be composed of the following fundamental units: (1) an inlet gas delivery and supply system, (2) a reaction chamber, (3) a loading/unloading system, (4) an energy system, (5) a vacuum system, (6) a process control system and (7) an exhaust gas treatment system [6].

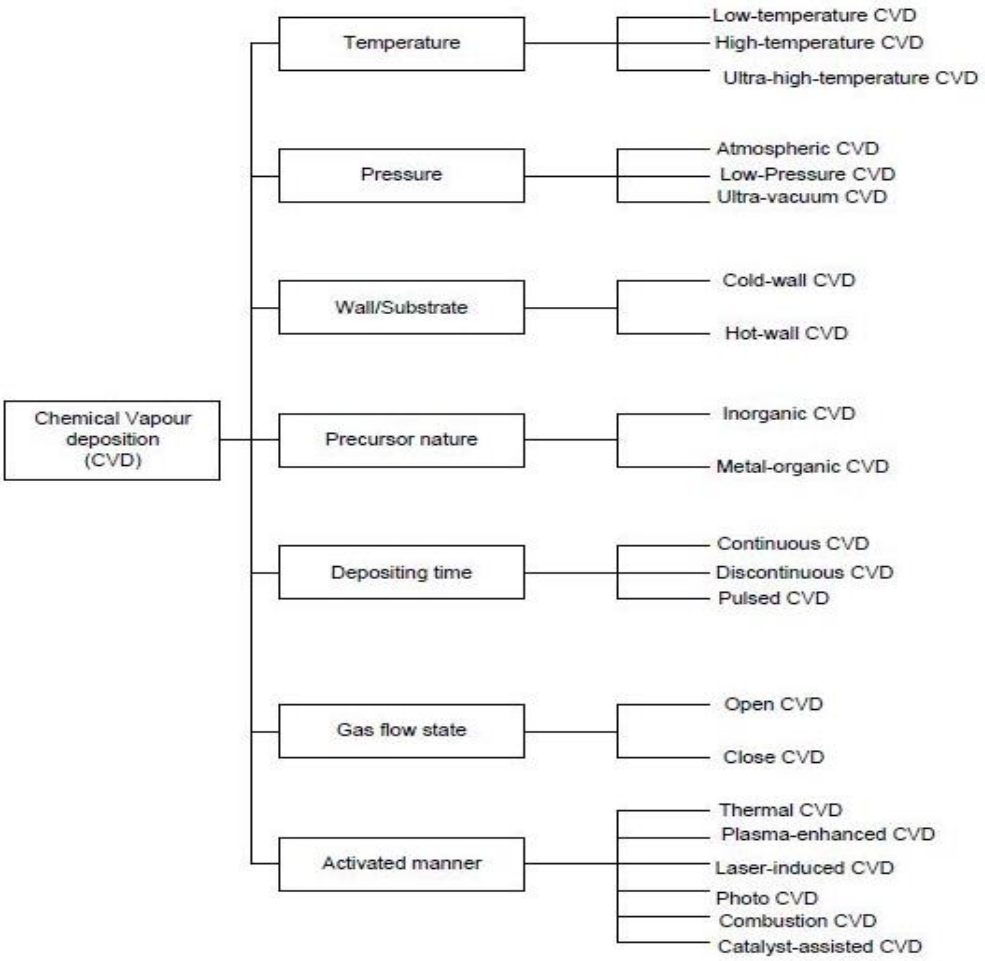


*Figure 2-2: Types of CVD process at different parameters [6].*

### 2.2.1 Thermal CVD

Thermal CVD system requires high temperatures between 800 $^{o}$C and 2000 °C [7]. This temperature can be generated by resistance heating, high frequency induction heating, radiant heating, hot plate heating, or any combination of these sources [7]. Thermal CVD system can be separated into two units system such as (a) hot-wall reactor (b) cold-wall reactor. These two reactors can be either horizontal or vertical [7]. Therefore, in this chapter focus is on hot-wall reactor, which is the technique that was used in this study.

#### 2.2.1.1 A hot-wall reactor

A hot-wall reactor is an isothermal furnace, which can be heated by resistive elements[7]. The coating layers in hot-wall reactor require that the reaction gases are usually introduced into the reactor after the temperature has been raised to the required level[7].

Figure 2-3 illustrates a thermal CVD system (hot-wall reactor) which was used for the coating of cutting tools with carbide such as TiC. This material (TiC) can be deposited alternatively under precisely controlled conditions. In some cases, the parts to be coated (such as semiconductor silicon wafers) are stacked vertically. This minimizes particle contamination and considerably increases the loading capacity (as opposed to horizontal loading)[7]. The advantage of the hot-wall reactor is close temperature control while the disadvantage is that the deposition occurs everywhere on the reactor walls, therefore these require periodic cleaning.

In this study, a vertical wall thermal CVD system was used and is discussed in chapter 4. This thermal CVD system was developed in-house at Necsa (The South African Nuclear Energy Corporation).

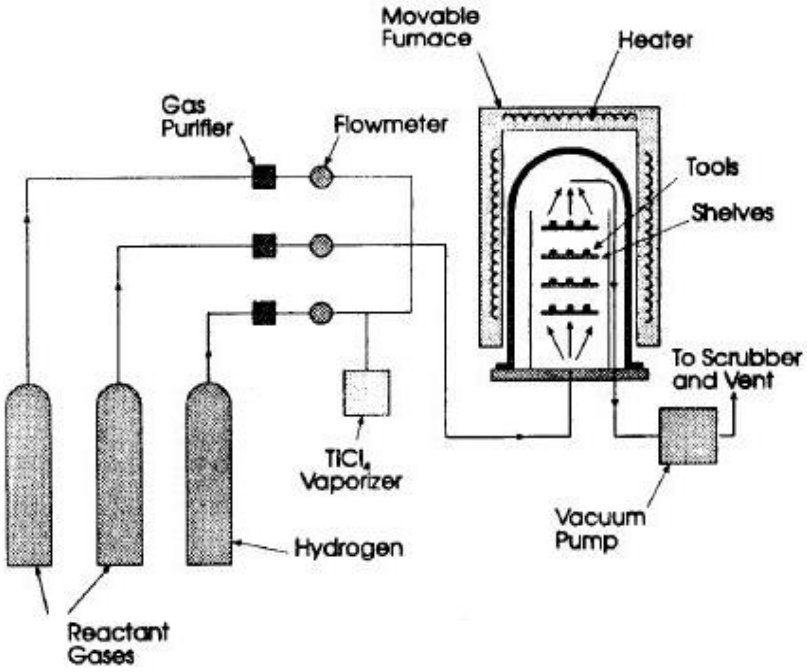


*Figure 2-3: Production thermal CVD reactor for the coating of cutting tools. Taken from [7].*

### 2.2.2 Configuration of a Chemical Vapour Deposition Apparatus

This section provide details of configurations of CVD systems which should involve four basic requirements as given below [6].

1. To deliver and control all of the precursor gas, carrier gas and the diluents gas into the reaction chamber.

2. To provide an energy source to initiate and drive the chemical reaction.

3. To remove the by-product exhaust gases from the reaction chamber and to dispose them safely.

4. To precisely control the process parameters (temperature, pressure, gas flow rate) automatically so that the quality of deposited products and the reproducibility can be maintained from run to run.

Based on these industrial requirements, a CVD system usually consists of several basic subsystems such as discussed below [6].

- **Gas delivery system**

This subsystem is used to supply the precursor in a controlled manner. After the reactant gases are mixed with carrier gas and diluent gas homogenously, the mixture gas is delivered into the reaction chamber.

- **Reaction chamber**

The reaction chamber is the heart of a CVD system where chemical vapour deposition takes place. It consists of retort, gas inlet injector, distributor and outlet exit. The quality of the deposit is mainly dependent on the design of the reaction chamber, which determines the uniformity of temperature, concentration and pressure.

- **Loading/unloading system**

This is normally a mechanical system to transport substrates, preforms, mandrels, etc. from the outside to the inside of the reaction chamber. This subsystem should be designed to reduce the labour intensity and cost.

- **Energy system**

An energy system must provide the energy required for the precursors to react at elevated temperatures, control and maintain the temperatures within the reaction chamber. When the CVD process is enhanced by some other methods such as plasma, additional energy supplies are required.

- **Vacuum system**

This consists of vacuum pumps, pipes, valves and connections, etc. This subsystem is used to evacuate the gases and control the pressure within the reaction chamber.

- **Process automatic control system**

A computer controlled system is designed and installed to automatically measure and control the deposition parameters such as pressure, flow rate, depositing temperature and time. In some cases, a gas analyser is used to monitor the CVD process. This subsystem is usually incorporated within the relevant aforementioned subsystems to ensure the quality of the deposition.

- **Exhaust gas treatment system**

This consists of a cold trap, a chemical trap, a particle trap, a wet scrubber etc. Exhaust gases for CVD are usually hazardous and toxic. Hence, they should be treated to a safe and harmless level and converted into safe compounds before being released into the atmosphere[6].

### 2.3 Synthesis of ZrC

ZrC layers can be prepared by different methods such as solid-state reactions [8], reactions using solution based precursors and through vapour phase reaction methods such a chemical vapour deposition (CVD)[9]. The characteristics of ZrC vary with the methods of preparation. These characteristics include chemical composition, microstructure and the impurities present. Therefore, when choosing a method of preparation and during the preparation of ZrC a number of factors need to be evaluated. These include: (a) chemical impurities such as oxygen and other gaseous impurities, (b) the stoichiometry of the product (i.e. carbon to zirconium ratio), (c) grain size and texture orientation, (d) the existence of secondary phases and (e) pore size, porosity and morphology[9].

#### 2.3.1 Synthesis of ZrC layers by carbothermal reduction of $ZrO_2$

The synthesis of ZrC from graphite and zirconia ($ZrO_2$) is a technique that can be used to obtain ZrC layers which has previously been reported[8]. The preparation of ZrC from $ZrO_2$ and graphite combines basically three processes: (1) hot pressing; (2) carbothermal reduction; and (3) sintering in a single process [9]. It relies on the reaction of heated graphite and $ZrO_2$ in an airtight furnace [9].The equation below shows the chemical reaction that takes place during carbothermal reduction:

$$ZrO_2\,(s) + 3C\,(s) \rightarrow ZrC\,(s) + 2CO\,(g) \qquad (2.1)$$

The temperature and duration of heating used in this method are usually from1800 °C to 2600 °C and between 16 h to 24 h [10]. The structure of ZrC produced by this method contains many impurities such as oxygen, which produces zirconium oxycarbide ($ZrC_xO_y$). To reduce

the amount of oxygen, several attempts have been used such as heating $ZrC_xO_y$ under controlled conditions so as to get a sample of the required shape, grain size, lattice parameter and density [9]. The reaction below in equation (2.2) relate to the heating of $ZrC_xO_y$ in the presence of carbon to give ZrC:

$$ZrC_xO_y + (1- x + y)\ C \rightarrow ZrC + yCO \qquad (2.2)$$

It has been reported that the complete removal of oxygen impurities from ZrC is very difficult [9]. The lowest levels of oxygen impurities were realized when the zirconium oxycarbide compound was close to its melting temperature. Although it is possible to obtain pure ZrC at the melting point of zirconium oxycarbide, reproducibility and compositional homogeneity are hard to achieve [10].

### 2.3.2 Synthesis of ZrC layers from solution-based precursors

In this method ZrC can be prepared by reacting organic compound solutions containing zirconium and carbon solutions [9]. Different liquid precursors have been used in the Sol-gel method. For example (a) single source metal-organic precursors such as tetraneopentyl zirconium $Zr[CH_2C(CH_3)_3]_4$. Healy et al. [11] reported that ZrC can be grown from metal-organic compound at relatively low temperatures, ranging from 300 °C to750 °C. However, the ZrC obtained was non-stoichiometric because of a high carbon content, with the ratio of C:Zr ranging from 2:1 to 5:1. (b) Metal alkoxides such as zirconium-n-propoxide $[Zr(OC_4H_9)]_4$ reported in ref [12].

Sol–gel processing includes the use of molecular precursors, mainly alkoxides, as starting materials. However, most alkoxides can react spontaneously with water to form a viscous precipitate. Therefore, they require to be chemically modified in order to control their hydrolysis and condensation. Therefore, in the case of ZrC, gel precursors were obtained by hydrolysis of zirconium alkoxides chemically modified by acetylacetone[13].

### 2.3.3 Synthesis of ZrC layers by vapour phase based reactions

Among the methods mentioned above, manufacturing of ZrC through the vapour phase reactions can be the preferred method applied in coating nuclear fuels. This method produces films with very low levels of impurities and porosity. That is why vapour phase synthesis is the method predominantly used for nuclear fuel coatings, since TRISO-fuel particles require uniform, dense and isotropic coatings normally produced in a fluidized bed reactor [9].

Ogawa et al. [14], Ikawaet al. [15] and Park et al. [16]reported on the synthesis of ZrC layers by a reaction between heated zirconium metal sponge and halogens (typically $I_2$, $Br_2$ and $Cl_2$) to synthesise zirconium halides ($ZrCl_4$, $ZrI_4$ and $ZrBr_4$). Thereafter, zirconium halide was then reacted with a carbon source, normally a hydrocarbon in gaseous form to produce ZrC.

In this study $ZrCl_4$ was used as Zr metal source, because it is not as dangerous as $ZrBr_4$ and can more effectively produce ZrC of good stoichiometry than $ZrI_4$[16]. CVD growth of ZrC layers from $ZrCl_4$ and $CH_4$ in the presence of $H_2$ was used in this study.

## 2.4 Spark Plasma Sintering (SPS)

### 2.4.1 Introduction

There are still challenges for processing and consolidating nanopowders and retaining the initial microstructure in the fabricated component. Therefore, the syntheses of new materials are limited on scale. Vigorous demand in market persist in driving serious attention to new consolidation techniques apart from hot pressing, high temperature extrusion, and hot isostatic pressing. This is due to longer processing times at high temperatures (1800 $^{o}$C) which often result in extraneous grain growth. Therefore, spark plasma sintering (SPS) can be used with rapid heating to sintering temperatures leading to rapid sintering of nanocomposites[17]. During the SPS process, the initial properties of the nanopowders can be retained when fabricating bulk materials. Therefore, the consolidation of metals, composites,

ceramics, intermetallics, cermets, nanocomposites, and carbon nanotube reinforced ceramics can be accomplished by spark plasma sintering[17].

### 2.4.2 Fundamental principles of SPS

Spark plasma sintering (SPS), also referred to by other names such as electric field assisted sintering (EFAS), field assisted sintering technique (FAST), plasma assisted sintering (PAS), and plasma pressure consolidation (PPC). SPS is a plasma assisted rapid sintering technique which momentarily generates high temperature plasma (spark plasma) between the gaps of compacted powder by electrical DC pulsing discharge [18,19].

SPS can be done at wide range of temperatures and pressures, with controls of temperatures or current during processing [20]. SPS has evolved as a sinter consolidation method to fabricate exotic and novel materials, which are difficult to fabricate by conventional processing techniques. This pressure assisted spark plasma sintering allows much shorter sintering temperatures and times, serving as an effective technique for obtaining fully dense nanocrystalline ceramic composites [21].

Spark Plasma Sintering is a moderate plasma sintering method based on the conjecture of high temperature plasma momentarily generated in the gaps between powder materials by electrical discharge during DC pulsing (see Figure 2-5). It has been suggested that the on-off DC pulse energizing method can generate: (1) spark plasma (2) spark impact pressure (3) Joule heating, and (4) an electrical field diffusion effect (see Figure 2-4)[22,23]. In this process, powders are loaded into a graphite die and heated by passing an electric current through the assembly. The low heat capacity of the graphite die allows rapid heating. Therefore, SPS can rapidly consolidate powders to near theoretical density through the combined actions of a rapid heating rate, pressure application, and proposed powder surface cleaning [22,23].

### 2.4.3. Advantages

SPS technique can produce high quality and uniform compacts which can be sintered rapidly at lower temperatures and short periods compared to conventional sintering methods [24]. Therefore, the advantages of SPS process have been reported to be [17,25]:

(1) The structure of powder particles is maintained by high temperature exposure through sintering. Pulsed resistance heating by generation of localized plasma between powder particles maintains the integrity of starting microstructure without grain coarsening.

(2) The electrical energy that is supplied in combination with mechanical pressure contributes to very short actual consolidation times, thereby also preventing the formation of coarse microstructures.

(3) The discharge plasma generated between powders particles confers a significant surface cleaning ability that can lead to enhanced particle sinterability

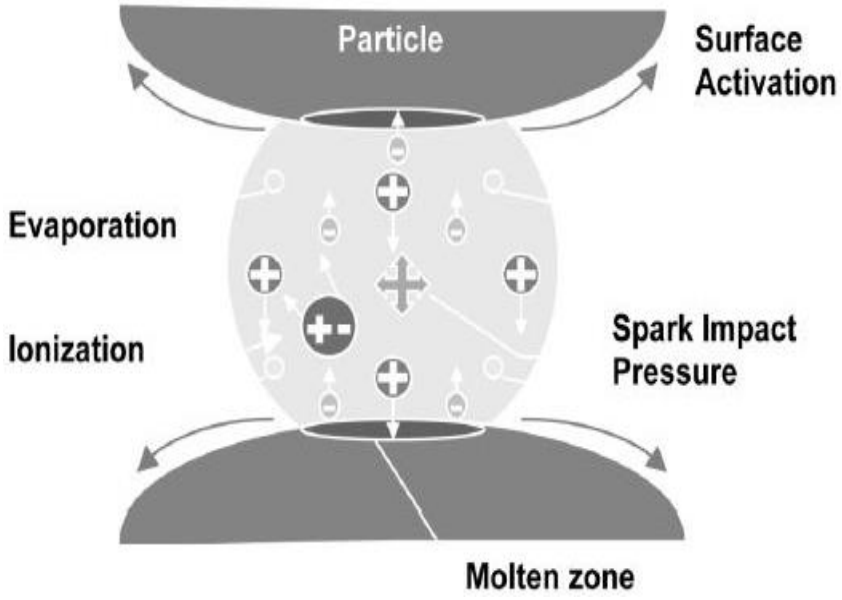


*Figure 2-4: Schematic of dominant sintering mechanism during SPS. Taken from* [17].

### 2.4.4. Equipment of SPS process and mechanism

Figure 2-5 shows the schematic of typical SPS instrument which consists of a graphite die where powder is loaded and is heated by passing electric current through the assembly. SPS

can rapidly consolidate powders to near theoretical density through the action of a rapid heating rate, application of pressure, and powder surface cleaning [23].

The powder mixtures are placed inside a graphite die and the typical SPS processing parameters are: (i) an applied pressure between 50 and 100 MPa, (ii) pulse periods cycles of 2.5 ms with on–off cycle of 2–2.5 ms, and (iii) maximum pulse parameter of 10,000 A and 10 V.

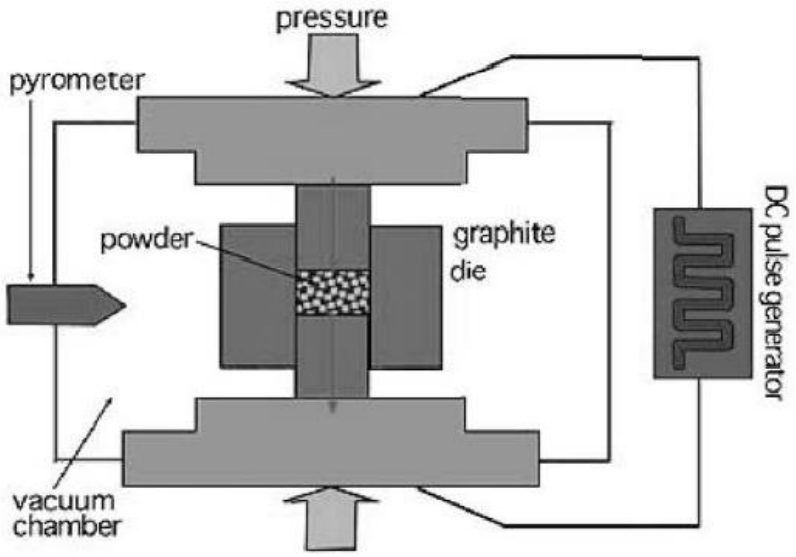


*Figure 2-5: Schematic of spark-plasma-sintering (SPS). Taken from* [22].

The entire process of densification using the SPS technique consists of four stages; (1) vacuum creation, (2) pressure application, (3) resistance heating and (4) cooling down as illustrated schematically in Figure 2-6 [20]. The vacuum step is used to remove gases. The process is carried out with applying pressure of typically 53 MPa to powder mixture during this vacuum process result in a densely consolidated composite [20]. In this study the process of SPS carried out under vacuum 50 MPa and discussed in chapter 4.

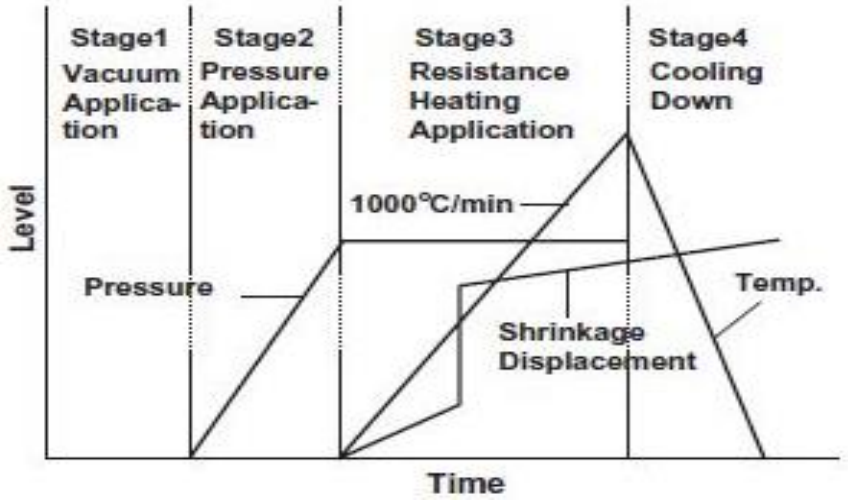


*Figure 2-6: Schematic representation of the temperature, pressure and shrinkage displacement profiles during spark plasma sintering. Taken from* [20].

**2.4.5 Synthesis of ZrC by Spark plasma sintering (SPS)**

(SPS) is an effective technique for manufacturing dense ceramics. During SPS, the rapid and thorough heat distribution through-out the samples generated from the high-frequency transformation and dispersion of the spark/Joule heat makes it possible to densify the materials at a low temperature and in a short time [26].

Many structural ceramics have been successfully fabricated by SPS including $ZrO_2$ and WC [27,28]. However, a relatively high sintering temperature may still be required for ZrC densification using the SPS method. Sciti et al.[29]investigated the sinterability of commercial powders by SPS and found that dense ZrC ceramics with a mean grain sizes of 13±1 μm and density of 10.1 g/cm$^3$ were obtained after sintered at 2100 $^o$C.

Previous studies by Nezhevenko et al. [30] reported on the the effect of initial porosity on the character of sintered of ZrC. ZrC powders with particle diameter was 5 μm, were sintered under isothermal conditions (T = 1200-1700 °C and by heating at a constant rate of 10 °C/min to temperatures of 2250, 2500, and 2700 °C. The ZrC specimens with initial

relative density 56% (ratio of the density to the standard density of ZrC of 6.73 g/cm$^3$) at 2500 °C, final density of 97% was attained.

In the case of sintering ZrC-C composites, Nezhevenko et al. [30] observed that densification was significantly inhibited in samples containing carbon (graphite or diamond) particles. The sintered densities tended to decrease as the (i) volume fraction of the carbon particle was increased. (ii) Particle size of carbon was decreased.

## References


[1] M.H. Francombe, Handbook of an introduction to thin films, Gordon and Breach Science, New York, 1973.

[2] K. Seshan, Handbook of thin film deposition processes and Techniques: Principles, Methods, Equipments and Applications, Noyes Publications , William Andrew, 2002.

[3] J.H. Park, Handbook of Chemical Vapor Deposition, ASM International, USA, 2001.

[4] K.L. Choy, Chemical vapour deposition of coatings, Prog. Mater. Sci. 48 (2003) 57–170.

[5] T.T. Kodas, M.J. Hampden-Smith, The Chemistry of Metal CVD, VCH Publishers, Weinheim, 1994.

[6] Y. Xu, X.-T. Yan, Chemical vapour deposition: an integrated engineering design for advanced materials, 1st ed., Springer, London, 2010.

[7] H.O. Pierson, Handbook of chemical vapor deposition: principles, technology and applications, 2nd ed., Noyes, New Jersey, 1999.

[8] A. Maitre, P. Lefort, Solid state reaction of zirconia with carbon, Solid State Ionics. 104 (1997) 109–122.

[9] Y. Katoh, G. Vasudevamurthy, T. Nozawa, L.L. Snead, Properties of zirconium carbide for nuclear fuel applications, J. Nucl. Mater. 441 (2013) 718–742.

[10] E.K. Storms, The refractory carbides, Academic Press, New York, 1967.

[11] M.D. Healy, D.C. Smith, R. Rodrigo R, R.W. Springer, J.E. Parmeter, The organometallic chemical vapor deposition of transition metal carbides: the use of homoleptic alkyls, Mater. Res. Soc. Symp. Proc. 327 (1994) 127–132.

[12] H. Wu, W. Zhang, J. Zhang, Pyrolysis synthesis and microstructure of zirconium carbide from new preceramic polymers, Ceram. Int. 40 (2014) 5967–5972.

[13] M. Dolle, D. Gosset, C. Bogicevic, F. Karolak, D. Simeone, G. Baldinozzi, Synthesis of nanosized zirconium carbide by a sol--gel route, J. Eur. Ceram. Soc. 27 (2007) 2061–2067.

[14] T. Ogawa, K. Ikawa, K. Iwamoto, Chemical vapor deposition of ZrC within a spouted bed by bromide process, J. Nucl. Mater. 97 (1981) 104–112.

[15] K. Ikawa, K. Iwamoto, Coating microspheres with zirconium carbide-carbon alloy by iodide process, J. Nucl. Sci. Technol. 11 (1974) 263–267.

[16] J.H. Park, C.H. Jung, D.J. Kim, J.Y. Park, Temperature dependency of the LPCVD growth of ZrC with the ZrCl4–CH4–H2 system, Surf. Coatings Technol. 203 (2008) 324–328.

[17] V. Viswanathan, T. Laha, K. Balani, A. Agarwal, S. Seal, Challenges and advances in nanocomposite processing techniques, Mater. Sci. Eng. R Reports. 54 (2006) 121–285.

[18] J. Wan, R. Duan, A.K. Mukherjee, Spark plasma sintering of silicon nitride / silicon carbide nanocomposites with reduced additive amounts, Scr. Mater. 53 (2005) 663–667.

[19] J.D. Kuntz, J. Wan, A.K. Mukherjee, Single-wall carbon nanotubes as attractive toughening agents in aluminabased nanocomposites, Nat. Mater. 2 (2003) 38–42.

[20] H. Kim, I. Shon, Consolidation and properties of binderless sub-micron tungsten carbide by field-activated sintering, Refract. Met. Hard Mater. 22 (2004) 257–264.

[21] G. Zhan, J.D. Kuntz, J.E. Garay, A.K. Mukherjee, Electrical properties of

nanoceramics reinforced with ropes of single-walled carbon nanotubes, Appl. Phys. Lett. 1228 (2003) 1228–1230.

[22] G.D. Zhan, A.K. Mukherjee, Carbon Nanotube Reinforced Alumina-Based Ceramics with Novel Mechanical, Electrical, and Thermal Properties, Appl. Ceram. Technol. 71 (2004) 161–171.

[23] G.D. Zhan, J. Kuntz, J. Wan, J. Garay, A.K. Mukherjee, A Novel Processing Route to Develop a Dense Nanocrystalline Alumina Matrix (<100 nm) Nanocomposite Material, J. Am. Ceram. Soc. 202 (2002) 200–202.

[24] C. Jia, H. Tang, X. Mei, F. Yin, X. Qu, Spark plasma sintering on nanometer scale WC – Co powder, Mater. Lett. 59 (2005) 2566–2569.

[25] R. Kumar, P. Cheang, K.A. Khor, Spark plasma sintering and in vitro study of ultra-fine HA and ZrO2–HA powders, J. Mater. Process. Technol. 140 (2003) 420–425.

[26] S.K. Sun, G.J. Zhang, W.W. Wu, J.X. Liu, T. Suzuki, Y. Sakka, Reactive spark plasma sintering of ZrC and HfC ceramics with fine microstructures, Scr. Mater. 69 (2013) 139–142.

[27] M. Yoshimura, T. Ohji, M. Sando, K. Niihara, Rapid rate sintering of nano-grained ZrO2-based composites using pulse electric current sintering method, J. Mater. Sci. Lett. 17 (1998) 1389–1391.

[28] S.G. Huang, K. Vanmeensel, O. der Biest, J. Vleugels, Binderless WC and WC--VC materials obtained by pulsed electric current sintering, Int. J. Refract. Met. Hard Mater. 26 (2008) 41–47.

[29] D. Sciti, S. Guicciardi, M. Nygren, Spark plasma sintering and mechanical behaviour of ZrC-based composites, Scr. Mater. 59 (2008) 638–641.

[30] L.B. Nezhevenko, I.I. Spivak, P. V. Gerasimov, B.D. Gurevich, V.N. Rystsov, Sintering of zirconium and niobium carbides with carbon additions, Sov. Powder Metall. Met. Ceram. 19 (1980) 535–539.

# Chapter 3. Thermodynamics

In this study, ZrC layers were grown by CVD at different temperatures and at atmospheric pressure. To understand the mechanism of ZrC layer formation and reactions between $ZrCl_4$ and $CH_4$, the thermodynamics of these interactions were investigated. This chapter also discusses the thermodynamics of the Ir-Zr, Ir-ZrC and Ir-C binary systems in order to understand the driving force which promotes chemical reactions to take place between Ir and sintered ZrC.

The standard software, HSC chemistry[1] was used to investigate the stages involved in the growth of the ZrC layers at different temperatures. The various binary phase diagrams are reviewed to study the chemical equilibrium conditions as a function of temperature and composition.

### 3.1 Law of Mass action

The mass action law is the proposition that the rate of a chemical reaction is directly proportional to its active mass or concentration (Rate $\propto$ Reactant). The mass action law can be introduced by using a general chemical reaction equation in which reactants *A* and *B* react at elevated temperatures to give products *C* and *D*.

$$aA + bB \rightarrow cC + dD \tag{3.1}$$

Where *a*, *b*, *c*, and *d* are the coefficients for a balanced chemical equation. The mass action law states that if the system is at equilibrium at given temperature, then the ratio of the reactant and products is a constant[2]:

$$K_c = \frac{[C]^c[D]^d}{[A]^a[B]^b} \tag{3.2}$$

where $K_c$ is the equilibrium constant for the reaction in equation (3.1).

### 3.2 Gibbs Free Energy

Gibbs free energy is a thermodynamic quantity that can measure the maximum, reversible work done by a thermodynamic system at constant temperature, *T* and pressure, *P*. For a chemical reaction to take place the Gibbs free energy is required to change. The driving force for a process to take place is given by the change in the Gibbs free energy for the reaction($\Delta_r G_T$)as:

$$\Delta_r G_T = \Delta H - T\Delta S \tag{3.3}$$

where$\Delta$H is the change in enthalpy,$T$ is the temperature and $\Delta S$ is the change in entropy. $\Delta_\mathrm{r} G_T < 0$ indicates that the reaction will take place and it will be spontaneous and the reaction proceeds spontaneously with a driving force proportional to the magnitude of $\Delta$G. In the case of $\Delta_\mathrm{r} G_T > 0$, a reaction will not occur and is non-spontaneous. While at $\Delta_\mathrm{r} G_T = 0$ the reaction is at chemical equilibrium [3].

The relationship between enthalpy (heat of formation) and temperature is given by:

$$\Delta H_T = \Delta H_{298} + \int_{298}^{T} \Delta C_p dT \tag{3.4}$$

The relationship between entropy and temperature is given by:

$$\Delta S_T = \Delta S_{298} + \int_{298}^{\mathrm{T}} \frac{\Delta \mathrm{C_P}}{\mathrm{T}} \mathrm{dT} \tag{3.5}$$

where $\mathrm{C_p}$is heat capacity usually expressed by an empirical relationship such as:

$$\mathrm{C_p} = \mathrm{a} + (\mathrm{b} \times 10^{-3})\mathrm{T} + (\mathrm{c} \times 10^{-6})\mathrm{T}^2 + (\mathrm{d} \times 10^{5})\mathrm{T}^{-2} \tag{3.6}$$

where *a*, *b*, *c* and *d*are constants. If the products and reactants have the same heat capacity there will be no change in the heat of formation ($\Delta$H) as a function of temperature (*T*).

In solid state reactions, equation (3.3) can be rewritten as an approximation given as[4]:

$$\Delta_r G_T = \Delta H_{298} - T\Delta S_{298} \quad (3.7)$$

In thermodynamic reactions, the temperature $T$ is usually below the melting points of reactants or products and the volume changes are negligible because they are very small. In such reactions, the change in entropy contribution is also very small ($\Delta S \approx 0$). The $T\Delta S°$ term becomes negligibly small compared to the heat formation$\Delta H$. Therefore, the change in Gibbs energy $\Delta_r G_T$ in equation (3.7) can be reduced to equation (3.8) when the $T\Delta S_{298}$term is small compare to $\Delta H_T$[5]:

$$\Delta_r G_T \approx \Delta H_{298} \quad (3.8)$$

This can occur for temperatures less than the melting point of reactants and products. However, the standard value at temperature ($T$ = 298 K) for enthalpy and entropy can be used for thermodynamic calculations. The change in Gibbs free energy can also be approximated by standard enthalpy only, when the change in entropy is considered to be zero.

The Gibbs free energy of a reaction can be determined from equation:

$$\Delta_r G_T = \sum \Delta_f G_T(products) - \sum \Delta_f G_T(reactants) \quad (3.9)$$

The Gibbs free energy of a reaction and the corresponding thermodynamic equilibrium constant can be calculated from equations (3.9) and (3.10) respectively:

$$K_T = exp - \left(\frac{\Delta_r G_T}{RT}\right) \quad (3.10)$$

where $K_T$is the rate constant, Ris the gas constant, and Tis temperature (K).

### 3.3 Thermodynamics of ZrC

The deposition of ZrC layers was performed using a vertical wall CVD system at different temperatures ranging from 1250 °C to 1450 °C using zirconium tetrachloride ($ZrCl_4$), methane ($CH_4$) and hydrogen ($H_2$) precursors with argon (Ar) as the carrier gas. Therefore,

the overall chemical reaction between $ZrCl_4$ and $CH_4$ to form ZrC in the CVD chamber is given below:

$$ZrCl_4\,(g) + CH_4\,(g) \rightarrow ZrC(s) + 4HCl(g) \qquad (3.11)$$

The temperature dependent values of Gibbs free energy of formation of $CH_4$, ZrC, HCl gas, and $ZrCl_4$ at atmospheric pressure were obtained from the JANAF thermodynamic tables[6] are given in Table 3-1. The calculated values of the change in Gibbs free energy for reaction given by equation (3.11) and the corresponding thermodynamic equilibrium constants for the temperature from 298.15 K to 2000 K at atmospheric pressure are also tabulated. The plots of the change in Gibbs free energy for the reaction as a function of temperature, and the equilibrium constant are shown in Figure 3-1.

The change in Gibbs free energy of the reaction at from 298.15 K to1600 K (1327 °C) can be observed to be > 0 (Table 3.1). This indicates that the reaction to form ZrC cannot occur spontaneously. However, at 1700 K (1427 °C), the change in Gibbs free of the reaction was found to be < 0 indicating that the reaction to form ZrC could occur and would proceed spontaneously. This indicates that the reaction for the production of ZrC is only possible starting from the temperature of 1427 °C (1700 K).

Figure 3-2 shows the speciation results obtained using the HSC chemistry software at different temperatures [1]. This thermodynamic approach, takes into account all possible product species via minimization of the system Gibbs free energy [7].The results indicate that the growth of ZrC is possible from a temperature of 900 °C (1173 K). Higher yields of ZrC are expected at higher temperatures.

The difference in the value of the reaction temperature between Figure 3.1 or Table 3.1 (1427 °C (1700 K)) and Figure 3-2 (900 °C (1173 K)) is because Figure 3.1 indicates the

equilibrium point of the reactants and the products. The temperature range for ZrC formation predicted from the plots in Figure 3-1 is similar to those reported in other reported studies [8–12].

*Table 3-1: Gibbs free energy of formation of ZrC and equilibrium thermodynamic constant resulting from the reaction of $CH_4$ and $ZrCl_4$ at atmospheric pressure.*

| T (K) | $\Delta_f G_T$ (kJ/mol) | | | | $\Delta_r G_T$ (kJ/mol) | $K_T$ |
|---|---|---|---|---|---|---|
| | $CH_4$ | $ZrCl_4$ | ZrC | HCl | | |
| 298.15 | -50.768 | -835.003 | -193.282 | -95.300 | 311.289 | 0.88198 |
| 300 | -50.618 | -834.786 | -193.262 | -95.318 | 310.870 | 0.882827 |
| 400 | -42.054 | -823.139 | -192.208 | -96.280 | 287.865 | 0.917080 |
| 500 | -32.741 | -811.635 | -191.299 | -97.166 | 264.413 | 0.938374 |
| 600 | -22.887 | -800.24 | -190.508 | -97.985 | 240.679 | 0.952898 |
| 700 | -12.643 | -788.929 | -189.806 | -98.747 | 216.778 | 0.963437 |
| 800 | -2.115 | -777.679 | -189.168 | -99.465 | 192.766 | 0.971434 |
| 900 | 8.616 | -766.470 | -188.570 | -100.146 | 168.700 | 0.977707 |
| 1000 | 19.492 | -755.286 | -187.995 | -100.799 | 144.603 | 0.982758 |
| 1100 | 30.472 | -744.113 | -187.428 | -101.430 | 120.493 | 0.986911 |
| 1200 | 41.524 | -732.717 | -186.635 | -102.044 | 96.382 | 0.990386 |
| 1300 | 52.626 | -721.224 | -185.744 | -102.644 | 72.278 | 0.993335 |
| 1400 | 63.761 | -709.755 | -184.875 | -103.234 | 48.183 | 0.995869 |
| 1500 | 74.918 | -698.303 | -184.023 | -103.815 | 24.102 | 0.998069 |
| 1600 | 86.088 | -686.863 | -183.182 | -104.388 | 0.0410 | 0.999997 |
| 1700 | 97.265 | -675.430 | -182.349 | -104.956 | -24.008 | 1.001700 |
| 1800 | 108.445 | -663.996 | -181.519 | -105.519 | -48.044 | 1.003216 |
| 1900 | 119.624 | -652.558 | -180.687 | -106.077 | -72.061 | 1.004572 |
| 2000 | 130.802 | -641.108 | -179.849 | -106.631 | -96.067 | 1.005794 |

Figure 3-2 also indicates that the methane is unstable at temperatures higher than 400°C, producing carbon and hydrogen upon decomposition. The formation of ZrC can be controlled by the flow rate of methane, with its decomposition making carbon available. The reaction rate of methane with $ZrCl_4$ is strongly influenced by the temperature of substrate surface. As

the temperature increases the chemical reaction is pushed to the region of high yield of ZrC and concurrently high degrees of dissociation of $ZrCl_4$ and methane.

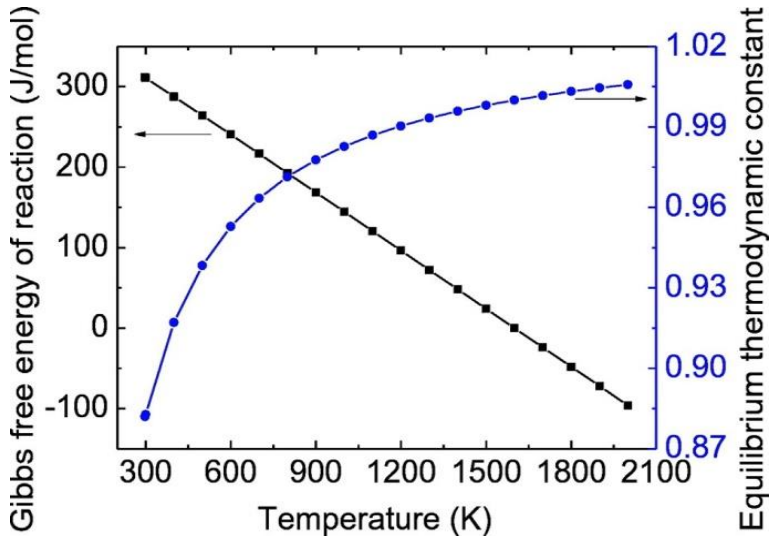


*Figure 3-1: Ellingham diagram for stoichiometric ZrC layers formation plotted from data in Table 3.1.*

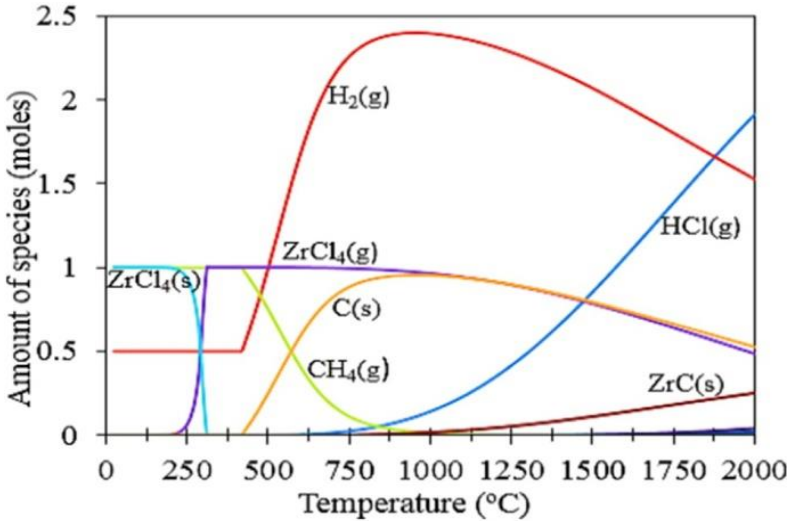


*Figure 3-2: Temperature dependent speciation curves of $ZrCl_4$, $CH_4$ and $H_2$ feed system.*

The formation of HCl starts at 750 °C, when the Zr reacts with free carbon at this temperature. If carbon was not present then the Zr can only react with Cl since it is present due to decomposition of $ZrCl_4$. By adding the hydrogen, Cl and hydrogen can react to form HCl. Therefore, the concentration of $H_2$ declines at the point where the HCl starts forming.

### 3.4 Phase Diagrams

Phase diagrams are graphical representations that indicate the chemical equilibrium conditions for a system usually as plots of temperature against composition. They show the ranges over which certain phases or mixtures of phases exist under conditions of thermodynamic equilibrium [13]. In this study, ZrC was synthesized by a CVD process and sintering and thereafter the solid state interactions between Ir and ZrC were investigated. Hence, understanding the phases present in the three binary systems is very important.

#### 3.4.1 Zirconium-Carbon binary phase diagram

Stable ZrC exists over a wide range of composition. Due to this wide range, ZrC is often considered to be as a non-stoichiometric compound [14,15]. The vacancies which exist in ZrC are usually from the missing carbon atoms and therefore its empirical formula is always written as $ZrC_x$, where $x<1$ [14,15].Carbon-rich composition typically leads to presence of graphitic carbon phase embedded in a slightly sub-stoichiometric $ZrC_x$ matrix [16].

Figure 3-3 shows the phase diagram of the Zr-C system, the $ZrC_x$ phase exists at from 38.5 to 49.6 at.% C [17]. The melting point of $ZrC_x$ is about 3723 K (3450 °C) when the carbon-to-zirconium (C/Zr) ratio approaches 0.78. When the composition of carbon is less than 37 at.% C, the $ZrC_x$ phase coexists with hexagonal close packed Zr (α-Zr) phase until around 1200 K. At about 1200 K, the α-Zr phase transforms to the body centered cubic (β-Zr). However, at temperature above 2100 K, the β-Zr phase starts to melt to give a liquid of Zr phase and a solid $ZrC_x$ phase. However when the carbon content is more than 49.5 atomic percent, the phases present are $ZrC_x$+C below 3200 K [16,17].

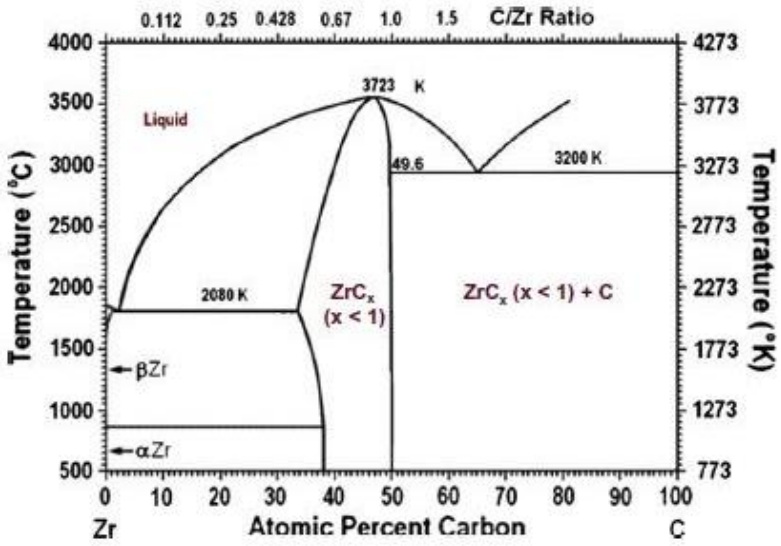


*Figure 3-3: Phase diagram of the Zr-C system* [16].

### 3.4.2 Iridium-Carbon binary phase diagram

The Ir-C phase diagram is presented in Figure 3-4 from the temperature range of 2000 °C to about 3000 °C [18]. The phase diagram has a eutectic point at 2208 °C with a composition of 20.8 at. % C. The melting point of Ir is about 2447 °C. The maximum solubility of carbon in iridium of < 3% is very low. Ir is non-reactive with carbon reportedly not forming carbide as seen the Ir-C phase diagram in Figure 3-4 [18,19].

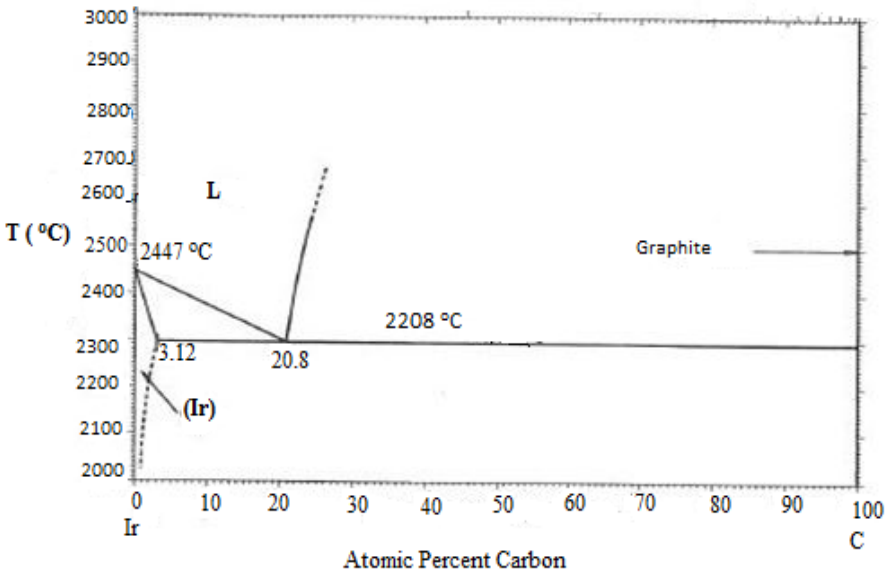


*Figure 3-4: Ir-C binary phase diagram obtained from* [18]

### 3.4.3 Iridium-Zirconium binary phase diagram

The Ir-Zr binary phase diagram in Figure 3-5 [20] is presented in the temperature range of 500 to 2500 °C. The Ir-Zr system consists seven intermetallic compounds such as $Ir_3Zr$, $Ir_2Zr$,α-IrZr, β-IrZr, $Ir_3Zr_5$, $IrZr_2$, and $IrZr_3$ [21]. The maximum solubility of Zr in Ir is about 5 at. % Zr at 2120 °C. The phase diagram indicates that the $Ir_3Zr$ phase melts congruently at 2280 °C with a composition of 22 at. % Zr. The IrZr phase undergoes polymorphic transformation from the α phase to β phase upon heating. From Figure 3-5 α-IrZr exists at temperatures below 900 $^{o}$C and β-IrZr exists at temperature above 900 $^{o}$C up to 2050 °C.

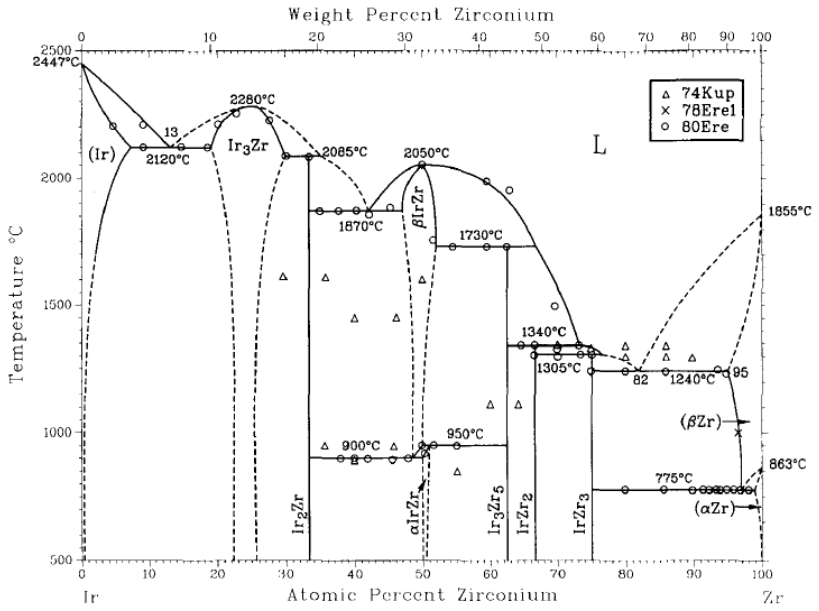


*Figure 3-5: Ir-Zr binary phase diagram taken from* [20].

### 3.4.4 Solid state reactions between ZrC and Ir

The driving force for solid state reactions is usually the change in the Gibbs free energy. For solid state reaction $\Delta H°$ is a good approximation of the change in free energy ΔG° because the change in entropy ΔS° is usually negligible [5]. The standard enthalpies of formation of ZrC and the Ir-Zr phases are given in Table 3-2. It can be seen that the standard heats of formation of the Ir-Zr system have lower magnitudes than those of ZrC. The probable

reactions between Ir and ZrC and the enthalpies of reaction are given in Table 3-3. Only the formation of Ir-Zr phases was considered since Ir carbides are not expected to form as previously seen in the Ir-C phase diagram in Figure 3-4.The reaction enthalpies were calculated using enthalpies of formation of ZrC and Ir-Zr system given in Table 3-2. It can be observed that the enthalpies of reaction (1) to (3) are negative, while reactions (4) to (6) are positive.

*Table 3-2: Standard enthalpies of formation at room temperature 298.15 K of ZrC and Ir-Zr phases. Taken from* [22]*and* [21]*respectively.*

| **Phase** | $\Delta H_f^o$ **(kJ.mole$^{-1}$·at)** |
|---|---|
| ZrC | -101.5 |
| $Ir_3Zr$ | -79.1 |
| $Ir_2Zr$ | -100.0 |
| IrZr | -114.4 |
| $Ir_3Zr_5$ | -98.2 |
| $IrZr_2$ | -89.0 |
| $IrZr_3$ | -67.6 |

Reactions to form Zr rich phases have positive enthalpies. The negative values of enthalpies of reaction indicate that reactions (1) to (3) between Ir and ZrC are favourable. Reaction (2) between Ir and ZrC to form $Ir_2Zr$ is thermodynamically favoured since it has the largest negative reaction enthalpy.

*Table 3-3: Enthalpies of possible reactions between ZrC and Ir.*

| # | Reaction | T(K) at room temperature | $\Delta H_R^o$ (kJ.mole$^{-1}$·at) |
|---|---|---|---|
| 1 | $ZrC + 3Ir \rightarrow Ir_3Zr + C$ | 298.15 | -22.7 |
| 2 | $ZrC + 2Ir \rightarrow Ir_2Zr + C$ | 298.15 | -24.3 |
| 3 | $ZrC + Ir \rightarrow IrZr + C$ | 298.15 | -8.6 |
| 4 | $5ZrC + 3Ir \rightarrow Ir_3Zr_5 + 5C$ | 298.15 | 17.6 |
| 5 | $2ZrC + Ir \rightarrow IrZr_2 + 2C$ | 298.15 | 27.8 |
| 6 | $3ZrC + Ir \rightarrow IrZr_3 + 3C$ | 298.15 | 48.4 |

## References


[1] Outotec, HSC Chemistry 7 (Thermo-chemical software), (2007).

[2] O.A. Kubaschewski, C.B. Alcock, Metallurgical Thermochemistry, Pergamon Press, New York, 1979.

[3] M. Ohring, A review of Materials Science, in: Mater. Sci. Thin Film. Depos. Struct., 2nd ed., Academic Press Inc, San Diego, 2002: pp. 17–56.

[4] L. Brewer and O. Krikorian, Reactions of Refractory Silicides with Carbon and Nitrogen, J. Electrochem. Soc. 103 (1956) 38–51.

[5] R. Pretorius, T.K. Marais, C.C. Theron, Thin film compound phase formation sequence: An effective heat of formation model, Mater. Sci. Reports. 10 (1993) 1–83.

[6] NIST, NIST-JANAF Thermochemical Tables, (2018). https://janaf.nist.gov/ (accessed March 25, 2018).

[7] S. Jarungthammachote, A. Dutta, Equilibrium modeling of gasification: Gibbs free energy minimization approach and its application to spouted bed and spout-fluid bed gasifiers, Energy Convers. Manag. 49 (2008) 1345–1356.

[8] J. Hoon, C. Hwan, D. Jin, J. Yeon, Effect of H2 dilution gas on the growth of ZrC during low pressure chemical vapor deposition in the ZrCl4–CH4–Ar system, Surf. Coat. Technol. 203 (2008) 87–90.

[9] J.G. Kim, D.J. Choi, D.K. Kim, Y.W. Lee, J.Y. Park, Microstructure and mechanical properties of chemical vapor deposited ZrC film on SiC/graphite substrate, J. Ceram. Process. Res. 10 (2009) 21–24.

[10] Q. Liu, L. Zhang, L. Cheng, Y. Wang, Morphologies and growth mechanisms of zirconium carbide films by chemical vapor deposition, J. Coatings Technol. Res. 6 (2009) 269–273.

[11] J. Hoon, C. Hwan, D. Jin, J. Yeon, Temperature dependency of the LPCVD growth of ZrC with the ZrCl4-CH4-H2 system, Surf. Coat. Technol. 203 (2008) 324–328.

[12] Y. Zhu, L. Cheng, B. Ma, S. Gao, W. Feng, Y. Liu, L. Zhang, Calculation and synthesis of ZrC by CVD from ZrCl4–C3H6–H2–Ar system with high H2 percentage,

Appl. Surf. Sci. 332 (2015) 591–598.

[13] A.R. West, Solid State Chemistry and its Applications., Wiley-VCH Verlag, New York, 1986.

[14] H. Hugosson, O. Eriksson, U. Jansson, B. Johansson, Phase stabilities and homogeneity ranges in 4d-transition-metal carbides: A theoretical study, Phys. Rev. B. 63 (2001) 1–11.

[15] A. Fernández Guillermet, Analysis of thermochemical properties and phase stability in the zirconium-carbon system, J. Alloys Compd. 217 (1995) 69–89.

[16] Y. Katoh, G. Vasudevamurthy, T. Nozawa, L.L. Snead, Properties of zirconium carbide for nuclear fuel applications, J. Nucl. Mater. 441 (2013) 718–742.

[17] R.W. Harrison, W.E. Lee, Processing and properties of ZrC, ZrN and ZrCN ceramics: a review, Adv. Appl. Ceram. 115 (2016) 294–307.

[18] T.B. Massalski, Binary Alloy Phase Diagrams, 2nd ed., American Society for Metals, Metals Park, Ohio, 1991.

[19] K.M. Axler, D.T. Eash, High-Temperature Compatibility Study of Iridium (DOP-26 Alloy) with Graphite and Plutonia, Los Alamos Natl. Lab. LA-11127-MS. (1987).

[20] H. Okamoto, The Ir-Zr (Iridium-Zirconium) System, J. Phase Equilibria. 13 (1992) 653–656.

[21] H. Ran, Z. Du, Thermodynamic assessment of the Ir--Zr system, J. Alloys Compd. 413 (2006) 101–105.

[22] R.C. Weast, Handbook of chemistry and physics., 67th ed., CRC Press Inc., Boca Raton, FL, 1986.

# Chapter 4. Sample Preparation

In this study some ZrC layers were deposited on graphite substrates using chemical vapour deposition (CVD) and others (ZrC samples) were manufactured from ZrC powder using spark plasma sintering (SPS). Iridium (Ir) thin layers were then deposited on the sintered ZrC by electron deposition. The Ir-ZrC samples were annealed at different temperatures to investigate solid-state interactions. This chapter discusses the techniques used to prepare these samples.

## 4.1 Chemical Vapour Deposited ZrC

A vertical-wall thermal CVD system shown in Figure 4-1 was used to deposit ZrC layers onto graphite substrates. Figure 4-1 (a) and (b) shows the reactor set up including the process and instrumentation diagram of the CVD system. This CVD system was developed in-house at Necsa (South African Nuclear Energy Corporation). This system consists of four fundamental components namely: (a) RF power supply induction heating source with maximum power output of 10 kW, (b) gas ($H_2$, Ar, $CH_4$ and $ZrCl_4$) supply and delivery system,(c) scrubber containing calcium carbonate chips ($CaCO_3$) for extracting and neutralizing the HCl gas which is formed as a by-product during the decomposition reaction, and (d) the reactor system, which is a cylindrical graphite reaction tube heated by an induction heating coil in which the substrate is mounted on a stage.

The distance between the four-turn helical copper coil and cylindrical graphite reaction tube was kept small, about 2 cm, so as to obtain good RF coupling. Alumina ($Al_2O_3$) ceramic material was placed in the gap between the graphite tube and the coil to reduce heat transfer from the heated graphite reaction tube to the coil. Alumina ($Al_2O_3$) also secured the graphite reaction chamber at the centre of the coil in a fixed position.

The graphite tube had an inner diameter of 2.µcm and a length of 30 cm. An inlet at the top of the graphite tube and outlet at the bottom allowed the flow of the gases past the heated substrate mounted on substrate stage. The substrate temperature was measured by an optical pyrometer through a quartz viewing window at the top of the flange.

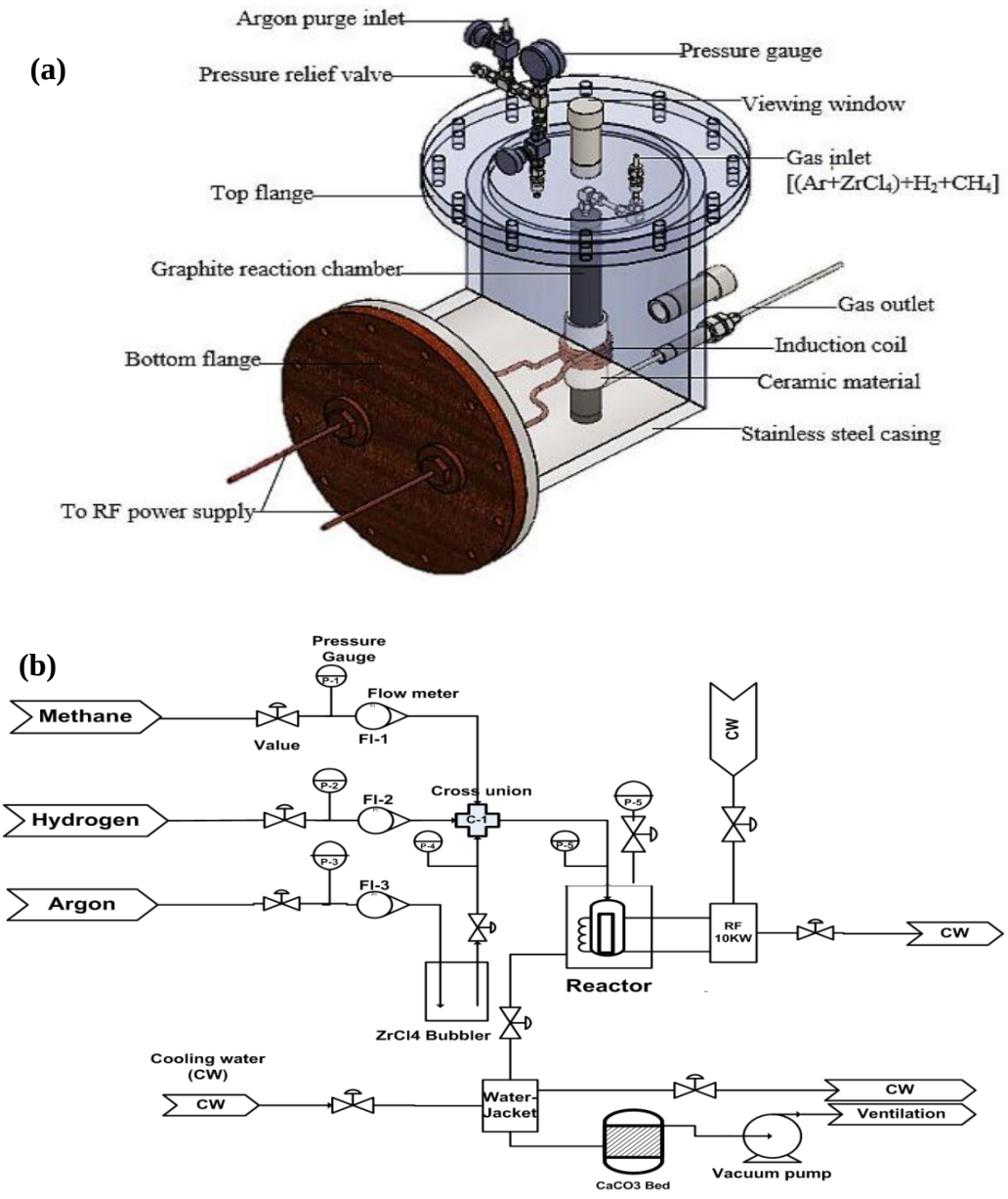


*Figure 4-1: Schematic diagram of the CVD reactor system, (b) Process and instrumentation diagram for the CVD reactor set-up. Taken from* [1].

All the gases ($H_2$, Ar and $CH_4$) were controlled by previously calibrated rotameters. To avoid $ZrCl_4$ from clogging the gas feed lines, all gas feed lines were heated to 300 °C by an electric heating tape.

$ZrCl_4$ powder and methane were used as Zr and C sources, respectively. The $ZrCl_4$ powder was vaporised in the vaporisation system consisting of an oven and stainless steel tube fitted with inlet and outlet feed lines. $ZrCl_4$ powder placed inside the stainless steel tube was heated in an oven with a thermostat to maintain a constant temperature.$ZrCl_4$ is very hygroscopic, therefore placing the $ZrCl_4$powder in the stainless tube was done in a glove box. The inlet consisting of stainless steel tube allowed argon to be swept through freely, therefore transporting $ZrCl_4$ into the reaction chamber.

To determine and optimize the vapour pressure of $ZrCl_4$ for the deposition of ZrC coating, $ZrCl_4$ powder was heated in vacuum and under argon for 3 min at temperatures ranging from20 $^oC$ to 400 $^oC$. Figure 4-2shows a plot of the pressure as function of temperature measured under vacuum at $10^3$kPa and at argon pressure of 11 kPa.

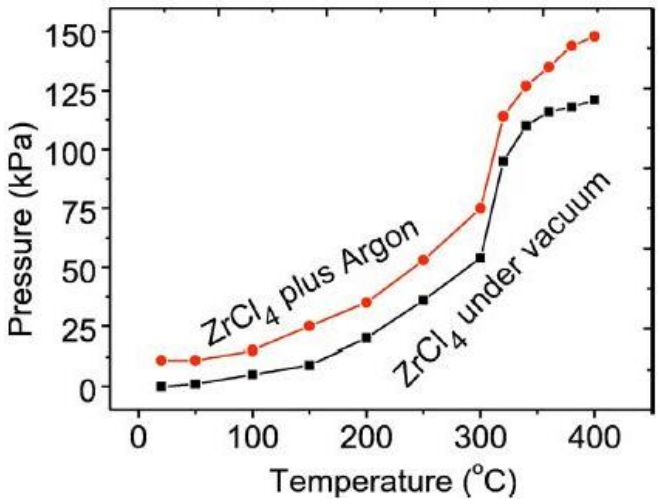


*Figure 4-2: Variation of pressure in the vaporizer as a function of temperature* [1].

For $ZrCl_4$ with argon, the total pressure measured was the sum of the $ZrCl_4$ (vapour) and argon partial pressures. It was shown that the presence of argon in the $ZrCl_4$ does not change the pressure-temperature trend of $ZrCl_4$, as shown in Figure 4-2. At temperatures between 20 to 150 °C the increase in pressure of $ZrCl_4$ is small. However at 190 °C up to about 330 °C, there is rapid increase in the pressure. This quick rise in pressure is due to an increase in $ZrCl_4$ vapour molecules as the temperature is increased [2]. After 330 °C the trend of the curve changed, indicating full sublimation of the $ZrCl_4$. To avoid full sublimation and to have a manageable vapour pressure, a temperature of 300 °C was selected during this study.

The vaporized $ZrCl_4$ was delivered into the reaction chamber by an argon flow, subsequently mixed with the $CH_4$ and $H_2$. The mass flow rate of $ZrCl_4$ was controlled by varying the argon flow rate. The $ZrCl_4$ mass flow rate as a function of argon flow is shown in Figure 4-3.The calibration curve was obtained by flowing argon through the $ZrCl_4$ powder at different argon flow rates for 20 min.

The $ZrCl_4$ flow rate was calculated from the mass difference after each run using: (4.1)

$$ZrCl_4 \text{ mass flow rate} = \frac{M_b - M_a}{t} \qquad (4.1)$$

where $M_b$ is the mass of the loaded $ZrCl_4$ vaporiser before vaporisation and argon flow and $M_a$ is the mass of the loaded $ZrCl_4$ vaporiser after vaporisation and argon flow rate.

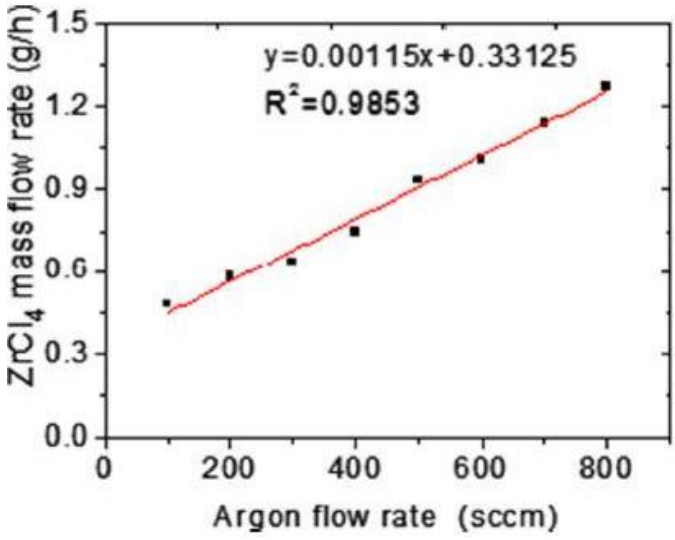


*Figure 4-3: Calibration curve of $ZrCl_4$ mass flow rate in argon* [1].

### 4.1.1 Raw materials and deposition of ZrC layers

Graphite substrates of 11 mm in diameter and 3 mm thickness were used to deposit the ZrC layers on. These substrates were cut from high density (1.71 g $cm^{-1}$) bulk graphite rods and were hand polished on a polishing wheel using 1000 grit silicon carbide paper. The polished substrates were sequentially cleaned by ultrasonic agitation with acetone, ethanol and then demineralised water, for 15 min each. The cleaned substrates were then dried in an oven at 250 $^{o}$C for 2 h. Before deposition, substrates were mounted on the clean graphite substrate stage inside the cylindrical graphite reaction tube. The loaded reactor was flushed by continuously pressurising and depressurizing using argon in order to remove air (oxygen) and atmospheric moisture.

The precursors used in deposition were $ZrCl_4$ powder (purity > 99.5%, Hf< 50 mg/kg) supplied by Sigma-Aldrich (Pty), and $CH_4$, $H_2$ and Ar with all with purity of 99.99%. $ZrCl_4$ was carried from the vaporization chamber to the reaction chamber by argon. Hydrogen gas was used to provide a reducing and diluting environment for $ZrCl_4$ vapour.

The ZrC deposition process can be described by overall chemical reaction given in (3.11).

The deposition was carried out at atmospheric pressure of 87 kPa for 2h at substrate temperatures ranging from 1250 $^{o}$C to 1450 $^{o}$C, excluding the time taken for the substrates to reach thermal equilibrium, which was between 5 to 10 minutes periods. The deposition rate of ZrC layer at each temperature was studied by measuring the mass before and after deposition with an electric balance with a precision of 0.0001g.

### 4.2 ZrC prepared by spark plasma sintering

The raw materials used were zirconium carbide powder (mean particle size of 5 nm and purity >99 %) from Sigma-Aldrich. The ZrC powder was weighed using an electronic mass balance, so that equal amounts of the ZrC powder were used for the spark plasma sintering (SPS) process. The powders were prepared in a 20 mm inner diameter graphite die. Graphite foil with a thickness of 0.2 mm was placed between the die and powder for easy removal and to ensure that the cooling of the sintered ZrC samples was homogeneous.

The outside of the graphite die was covered with an insulating felt to reduce radiation loss [3]. After the powder was placed in the graphite die, it was first cold pressed using a hydraulic press to consolidate the powder together and then spark plasma sintered (SPS). The ZrC ceramic pellets were sintered by SPS using the HHPD-25 from FCT Syteme GmbH Germany at Tshwane University of Technology (see Figure 2.2 in chapter 2).The SPS process was conducted at temperatures of 1700 °C, 1900 °C and 2100 °C at a heating rate of 100 °C/min in vacuum (0.05 bar) until the desired temperature was attained. The holding time and pressure for sintering were 10 minutes and 50 MPa respectively. At the end of the sintering cycle, the specimens were rapidly cooled to room temperature. The samples of 20 mm diameter and approximately 5mm thickness were attained. The samples were then cut into smaller pieces by a diamond sawand thereafter polished using a Saphir 550 Semi-Automatic Grinder/Polisher. The samples were then cleaned in an ultrasonic bath using

demineralised water and then ethanol for 5 min each. Thereafter, the samples were dried in an oven at 100 $^{o}$C for 30 min.

### 4.3 Electron beam deposition of Iridium thin film on ZrC

The electron beam deposition (EBD) set-up used in this study is shown in Figure 4-4[4]. It consisted of a vacuum chamber, substrate holder, a water cooled hearth, electron emitter magnetic lens and a filament. The filament emits electrons which are accelerated and focused onto the target (crucible containing the metal) by electric and magnetic fields. The accelerated electrons thermally evaporate the metal allowing metal atoms to travel towards the substrate at a controllable deposition rate. The e-beam chamber was first pumped down to a base pressure of $5\times10^{-7}$mbar. The deposition of iridium on ZrC substrate was done at a pressure of approximately $1\times10^{-6}$mbar.

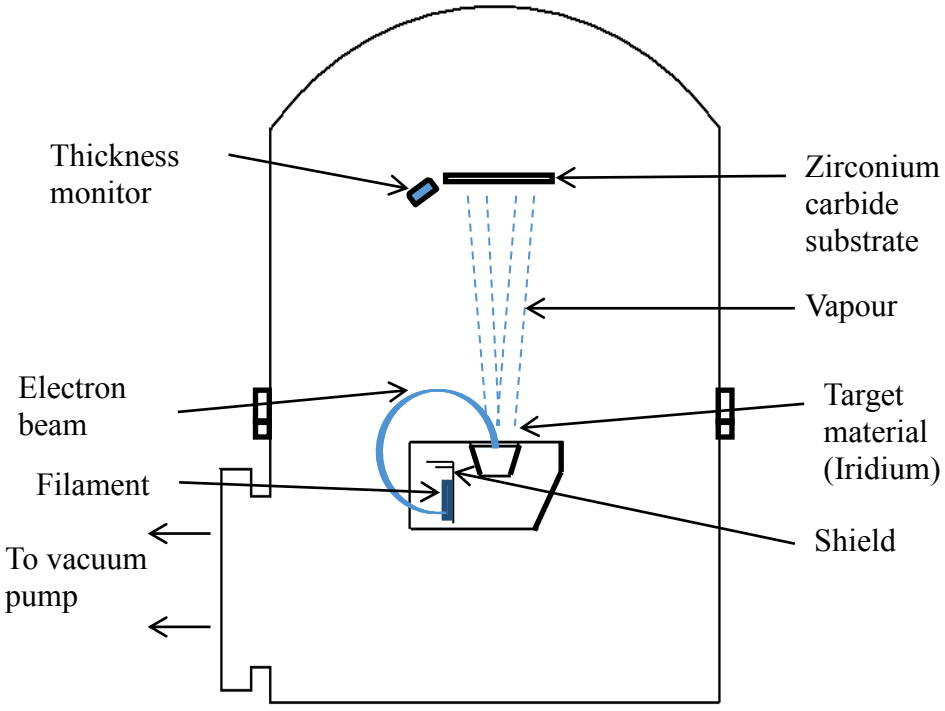


*Figure 4-4: The electron beam deposition (EBD) system. Taken from[4].*

### 4.4 Annealing

Annealing is a very important step in the study of solid-state reactions because it can activate and accelerate diffusion, intermixing and reaction processes. The as-deposited Ir-ZrC samples were annealed in vacuum using a quartz tube furnace. Figure 4-5 taken from [5], shows a schematic diagram of the quartz tube furnace annealing system at University of Pretoria. The samples were placed in a quartz tube sample holder. This tube has a thermocouple wire for measuring the annealing temperature. An outer larger quartz tube was connected to the turbo pump housing. The thermocouple was connected to a data acquisition system (Agilent 34970A) which was interfaced to a computer that collected and stored annealing data.

The quartz tube was initially evacuated to $10^{-3}$ mbar by the fore pump and thereafter the turbo pump system was switched on. The two pumps were left running until the vacuum gauge read a pressure of approximately $10^{-6}$ mbar. The annealing temperature was pre-set, the furnace switched on, allowed to attain and stabilize at the desired temperature.

Then the furnace was drawn over the quartz tube with the sample inside in order to allow the sample to heat up quickly. This was done while the data acquisition program was running on the computer. After the annealing duration was attained, the furnace was pulled away from the quartz tube to allow the sample to cool down rapidly and reach room temperature. The high vacuum during annealing at a base pressure of around $10^{-6}$ mbar was necessary to reduce oxidation of sample during the annealing temperature. The Ir-ZrC (SPS) samples were annealed at temperatures of 600 °C and 800 °C for 2h.

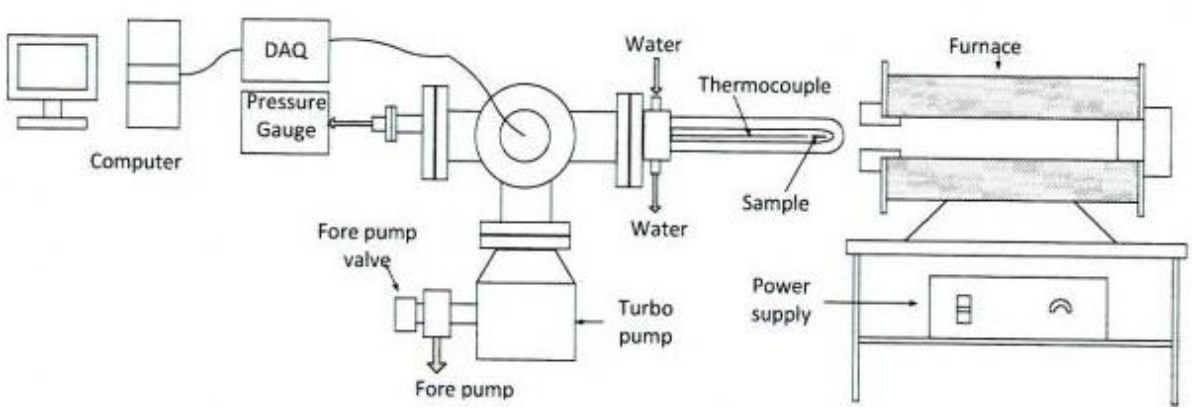


*Figure 4-5: Tube furnace annealing system consisting inter alia of a data logging system, vacuum pumps and furnace. Taken from* [5].

## References


[1] S. Biira, P.L. Crouse, H. Bissett, B.A.B. Alawad, T.T. Hlatshwayo, J.T. Nel, J.B. Malherbe, Optimisation of the synthesis of ZrC coatings in a radio frequency induction-heating chemical vapour deposition system using response surface methodology, Thin Solid Films. 624 (2017) 61–69.

[2] C. Liu, B. Liu, Y. Shao, Z. Li, C. Tang, Vapor pressure and thermochemical properties of ZrCl4 for ZrC coating of coated fuel particles, Trans. Nonferrous Met. Soc. China. 18 (2008) 728–732.

[3] A. Zavaliangos, J. Zhang, M. Krammer, J.R. Groza, Temperature evolution during field activated sintering, Mater. Sci. Eng. A. 379 (2004) 218–228.

[4] S.M. Tunhuma, F.D. Auret, J.M. Nel, E. Omotoso, H.T. Danga, E. Igumbor, M. Diale, Electrical characterization of defects induced by electron beam exposure in low doped n-GaAs, Nucl. Instruments Methods Phys. Res. Sect. B Beam Interact. with Mater. Atoms. 409 (2017) 36–40.

[5] Eric Gitau Njoroge, Solid-state interactions between Zr thin films and SiC, PhD thesis, University of Pretoria, 2014.

# Chapter 5. Analytical and characterisation Techniques

In this study, two sets of samples were used, viz. ZrC layers deposited on carbon substrates using chemical vapour deposited (CVD) method and ZrC manufactured by a spark plasma sintering process from powder. Iridium (Ir) layers were deposited on some of the sintered ZrC samples. Ir-ZrC were then annealing at temperatures ranging from 600 $^{o}$C to 800 $^{o}$C for 2 hours in vacuum ($2\times10^{-6}$ mbar). The deposited, sintered and annealed samples were characterised by X-ray Diffraction (XRD), Energy Dispersive Spectroscopy (EDS), Raman Spectroscopy and Scanning Electron Microscopy (SEM). This chapter discusses the analytical techniques used on this study.

## 5.1 X-ray diffraction (XRD)

XRD is a technique used to determine the properties of different material structures. This technique is used for phase identification, to measure the crystallite size, residue stress, lattice strain, preferred orientation, lattice parameters, etc.[1]. The crystal structure or arrangement of atoms in a solid is determined by the diffraction of waves suggested by Von Laue in 1912; however, it was developed by Bragg in 1913 and now is used in different fields of scientific research [2].

X-rays are a part of the electromagnetic spectrum in the region between ultraviolet and gamma rays. X-rays have a shorter wavelength of (about 0.1 to 10 nm) when compared to the visible light (about 400 to 800 nm) and X-rays also have a higher energy (of about $10^2$ to $10^5$ eV) as compared to light (10 eV) [3].

### 5.1.1 Bragg's law

When X-rays are incident on atoms (planes), the X-ray wave collides with atoms causing the scattering and interference of the waves to occur. Therefore, the peaks in X-ray diffraction pattern are related to the interatomic distances [4]. Figure 5-1 shows an incident X-ray beam

interacting with atoms. The wavelength of the incident light has to be on the same order as the spacing of the atoms.

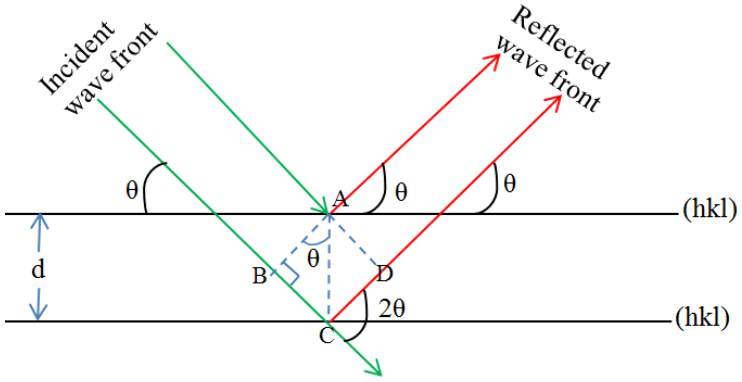


*Figure 5-1: Scattering of X-rays and Bragg's law. Taken from [4].*

The incident X-ray beam and the atoms (planes) make an angle θ between them. The angle between the incident X-ray beam and reflected X- ray beam is 2θ. Reflection of X-rays only occurs, when the conditions for constructive interface are fulfilled. In Figure 5-1 the difference in path length is:

$$2BC = n\lambda \tag{5.1}$$

where n is the integer which represents the order of diffraction and λ is the wavelength of the X-rays. If one considers the dotted triangle with the hypotenuse of *d* in Figure 5-1, Bragg's law (named after L. Bragg) can be obtained [4].

$$n\lambda = 2d_{hkl}Sin\theta_{hkl} \tag{5.2}$$

In equation (5.2) θ is the Bragg's angle, which is half of scattering angle , *n* is the integer which represents the order of diffraction and λ is the wavelength of the X-rays, $d_{hkl}$ is interplanar distance. Using Bragg's equation (5.2), the values of lattice parameter (*a*) can be determined. For cubic crystalline materials such as ZrC, the lattice parameter (*a*) is described by Equation 5.3:

$$a^2 = d^2{}_{hkl}\left(h^2 + k^2 + l^2\right) \tag{5.3}$$

where hkl are the Miller indices for the (hkl) plane, $(h^2 + k^2 + l^2)$is a constant which is replaced by *m*. Combining Equations 5-2 and 5-3, the value of *a* can be determined from the equation 5.4:

$$a^2 = \frac{m\lambda^2}{4\sin^2\theta_{hkl}} \tag{5.4}$$

where *m* is a positive integer, the peaks of the diffraction pattern must be indexed in order to obtain the correct value of m, so that *a* is analytically obtained from Equation (5.4) [4].

### 5.1.2 XRD diffractometer

Figure 5-2 shows a diffractometer. A diffractometer consists of an X-ray source (X-ray tube) producing monochromatic X-ray of known wavelength, a sample holder, and an X-ray detector as shown in Figure 5-2.The X-rays are generated in a cathode ray tube by heating the filament to produce electrons [5]. Thereafter, the electrons are accelerated by high voltage towards the target, bombarding the target sample with electrons. If the electrons have sufficient energy to dislodge inner shell electrons of the target material, characteristic X-rays are produced. The X-rays are generated by the cathode ray tube are then filtered to produce monochromatic radiation, collimated to concentrate and then directed toward the sample which needs to be analyzed.

The geometry of an X-ray diffractometer is such that the sample rotates in the path of the collimated X-ray beam at an angle θ. While the X-ray detector is mounted on an arm to collect the diffracted X-rays and rotates at an angle of 2θ. The instrument used to maintain the angle and rotate the sample is termed a goniometer.

The sample and detector are on the same side. As the sample or detector is rotated, the intensity of the reflected X-rays is recorded. When the geometry of the incident X-rays impinging the sample satisfies the Bragg equation, constructive interference occurs and a

peak appears. A detector records and processes this X-ray signal and converts the signal to a count rate which is then output to a device such as a printer or computer monitor.

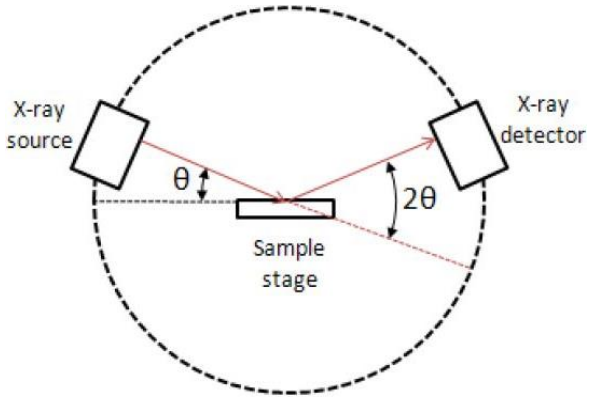


*Figure 5-2: The X-ray diffractometer. Taken from [5].*

### 5.1.3 XRD applications

X-ray diffraction can be applied to identify crystallinity of the sample, phase composition, lattice parameters and preferred orientation. Phase identification is obtained by measuring the *d*-spacing and integrating the intensities from the XRD pattern.

The first scientist that investigated the effect of limited crystallite size on X-ray diffraction patterns was Paul Scherrer in 1918. He published an equation which became known as Scherrer's equation [6]. He used equation (5-5) to calculate the crystal sizes in a solid material based on broadening of the diffraction peak(s). The Scherrer's equation can be written as:

$$D = \frac{K\lambda}{B\cos\theta_B} \tag{5.5}$$

where $D$ is the crystallite size, $K$ is dimensionless shape factor (values between 0.62 – 2.08),$\lambda$ is wavelength, $B$ is the full width at half maximum (FWHM) in radians, and $\theta_B$is Bragg angle in radians.

The Scherrer's equation is limited to nano size particles and it cannot be used for grains larger than about 0.1 to 0.2 μm. The Scherrer formula provides a lower bound on the particle sizes because of a variety of factors. These factors which include crystal size, inhomogeneous strain and instrumental effects, can contribute to the width of a diffraction peak.

The preferred orientation can be determined analytically by the texture coefficients. The texture coefficient $T(hkl)$ is determined by Equation 5.6 [7]:

$$T(hkl) = \frac{I(hkl)/I_0(hkl)}{(1/N)\sum_N I(hkl)/I_0(hkl)} \tag{5.6}$$

where *I(hkl)*is the relative intensity of the *(hkl)* plane as measured from the diffraction pattern of the sample and *N* is the number of diffraction peaks considered. The quantity $I_o(hkl)$ is the reference relative integrated intensity of the randomly oriented grains (powder sample). If the values of *T(hkl)* are less or equal to one, then it means the crystallites in the plane are randomly oriented. When the value of *T(hkl)*is greater than one it implies that the preferred orientation of the crystallites is in the given *hkl* direction [7].The value of $I_o(hkl)$for the corresponding plane can be obtained from the JCPD data files**.**

The conventional Bragg-Brentano X-ray diffraction geometry is not useful to study ultra-thin, graded composition and multi-layered thin films, this because of poor sensitivity and because of presence of the interfering effect of the substrate [8]. This makes it very difficult to identify the phases present in such samples. A popular technique for analysing thin films is the use the grazing incidence angle geometry, known as glancing incidence XRD (GIXRD).

GIXRD geometry which is a slight modification of conventional Bragg-Brentano geometry is attained by making the X-ray fall on the sample at a glancing angle (θ) while the detector on the 2θ axis scan the XRD pattern as seen in Figure 5-3 [9]. In GIXRD geometry, the incident X-ray beam remains stationary at a very small angle with the surface of the sample (typically

1° to 5°) while the detector rotates through the angular range (radial scan). This increases the length of the path which the X-ray beam travels through the thin film and therefore increasing the diffracting volume as in shown Figure 5-3. This acts to increase the intensity of diffracted X-rays originating from the near surface volume, thus also from shallow layers, and reduces the intensity of the diffraction from the underlying substrate [9].

The aim of XRD analysis is to identify the crystalline phases present. This is accomplished by comparing the peak positions and relative intensities with those from a large set of database provided by the International Centre for Diffraction Data (ICDD). The ICDD maintains the data base of inorganic and organic species known as the Powder Diffraction File (PDF). The PDF-2 database version contains in addition to d-spacing and intensities, the hkl values, the chemical name, the chemical formula, cell dimensions and selected physical properties [9].

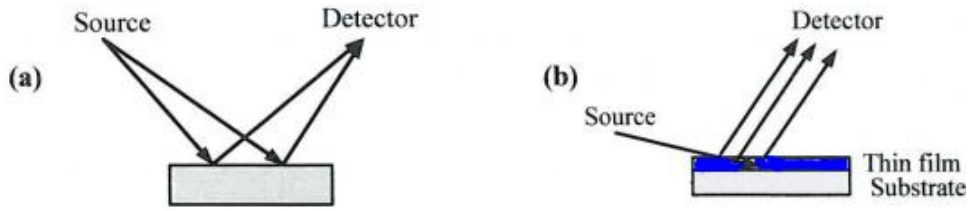


*Figure 5-3: XRD geometries for (a) bulk analysis and (b) thin film. Taken From [9].*

### 5.1.4 XRD Experimental Setup

The analysis was performed at South Africa Nuclear Energy Corporation (Necsa) XRD Laboratory. GI and Bragg-Brentano scattering geometry XRD analysis were done using a Bruker-AXS diffractometer, D8 Advanced XRD system with a Cu (Kα) X- ray radiation source, at 2θ step size of 0.04° and dwell time of 5s per frame. For GIXRD analysis, the incident X-ray beam was kept at an angle of 3° relative to the surface of sample and the diffraction pattern collected by a detector rotated by a goniometer from 24° to 117°. Bragg-Brentano or wide-angle XRD analysis was also performed on the as-deposited ZrC samples.

The radiation source angle (θ) was maintained at 15° and the detector angle scan from 10° to 125°.

The XRD diffraction data was shifted to 2θ positions corresponding to the wavelength of copper Kα radiation (λ = 0.1540598 nm). This was done to enable comparison this results with the standard diffraction files from the International Centre for Diffraction Data files (ICDD and PDF-2) for indexing purposes.

### 5.2 Raman Spectroscopy

Raman spectroscopy is a non-destructive technique for structural and chemical composition characterisation of materials by employing the Raman scattering effect [10]. It was discovered by Chandrasekhar Venkata Raman in 1928 in India [11].This technique is based on the inelastic scattering of monochromatic light from a laser in the visible, near infrared, or near ultraviolet near range [12]. Inelastic scattering means that the photon frequency of monochromatic laser light changes after interaction with a sample [13].

Raman system consists of major fundamental components such as the sample illumination system and light collection optics, the excitation source (laser), a detector and wavelength selector (filter or spectrophotometer) as shown in Figure 5-4. The sample to be measured is usually irradiated with a laser beam. The scattered light after interaction with the sample is collected by a lens. The lens then directs this scattered light through an interference filter or a spectrophotometer to obtain a Raman spectrum of a sample [13].

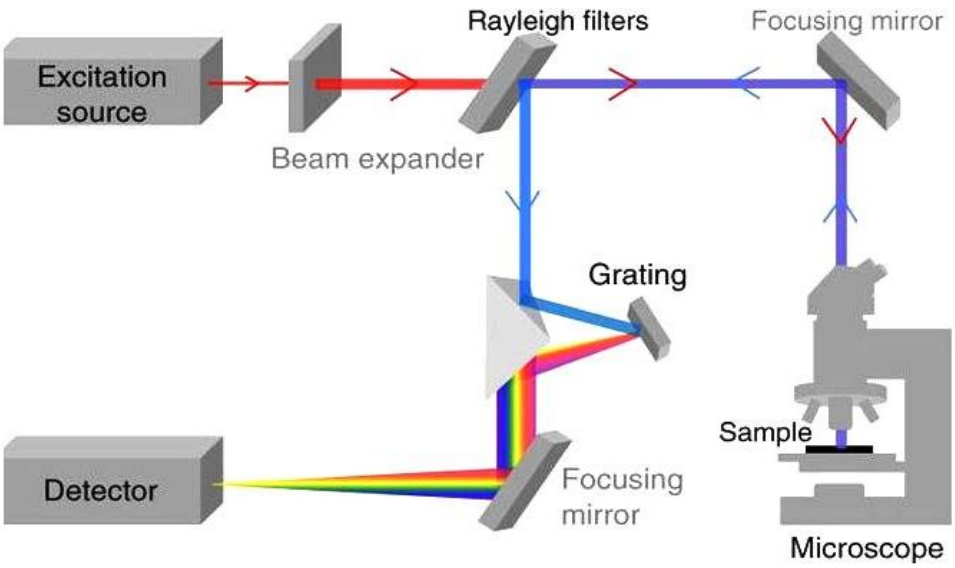


*Figure 5-4: Schematic of instrument interment of Raman Spectroscopy. Taken From [13].*

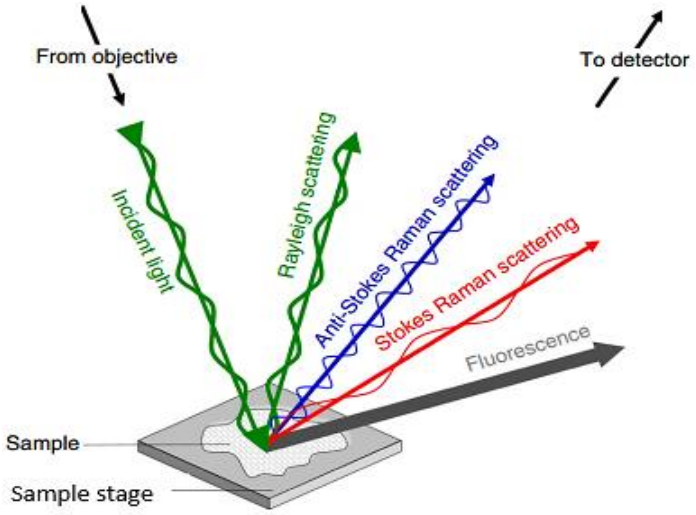


*Figure 5-5: Scattering of incident radiation by a sample illuminated by a laser beam. Taken from [13].*

In Raman experiments the sample is irradiated with a monochromatic laser light with frequency $v_o$as shown in Figure 5-5. The frequency of a big fraction of the scattered radiation is similar to the frequency of incident beam $v_o$ as shown in Figure 5-6. This kind of scattering radiation is elastic and it called Rayleigh scattering. However, the frequency of small fraction of incident beam is ($v_o \pm v_m$), where $v_m$ is a vibration frequency of a molecule. This kind of scattering is inelastic and it is called Raman scattering. If the frequency of scattering radiation

is about $v_o$ - $v_m$, it is called the Stokes lines in the Raman spectrum and for anti-Stokes for the $v_o$+ $v_m$ scattered light[14,15].

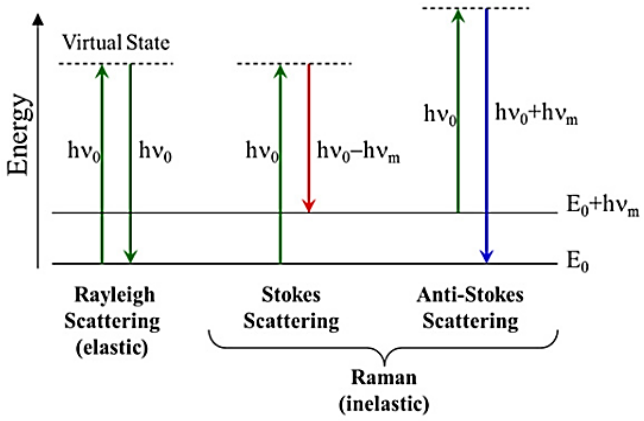


*Figure 5-6: Energy level diagram for Raman scattering (a) Stokes scattering (b) anti-Stokes scattering. Taken From [14].*

Thus, in Raman spectroscopy, we measure the vibrational frequency ($v_m$) as a shift from the incident beam frequency ($v_o$). In contrast to IR spectra, Raman spectra are measured in UV-visible region where the excitation as well as Raman lines appear [16].

According to classical electromagnetic theory by Ferraro et al.[16], Raman scattering can be explained as follows: The electric field strength *E* of an incident electromagnetic wave (laser beam) fluctuates with time *t* as given in Equation (5.7):

$$E = E_o \cos 2\pi V_o t \tag{5.7}$$

where $E_o$ is the vibrational amplitude and $V_o$ is frequency of laser. If a diatomic molecule is irradiated by this light an electric dipole moment P is given:

$$P = \alpha E = \alpha E_o \cos 2\pi V_o t \tag{5.8}$$

where α is a proportionality constant and is called polarizability. If the molecule is vibrating with a frequency $V_m$ and with a particular vibrational amplitude $q_o$, then the displacement $q$ of the molecule about its origin can be written as:

$$q = q_o \cos 2\pi V_m t \tag{5.9}$$

where $q_o$ is the vibration amplitude. However, for small amplitude vibration α is a linear function ofq, therefore it can be represented this equation:

$$\alpha = \alpha_o + (\partial_\alpha/\partial_q)_o q_o + \cdots \tag{5.10}$$

where $\alpha_o$the polarizability of equilibrium is position and$(\partial_\alpha/\partial_q)_o$is the rate change of α respect to the change in q evaluated at the equilibrium position. Therefore by combining equations (5.10) and (5.9) and then (5.8) it can obtain:

$$P = \propto_o E_o cos(2\pi V_o t) + (\partial_\alpha/\partial_q)_o q_o E_o cos(2\pi V_o t)\, cos(2\pi V_m t) \tag{5.11}$$

$$P = \propto_o E_o \cos(2\pi V_o t) + \frac{1}{2}\left(\partial_\alpha/\partial_q\right)_o q_o E_o [cos\{2\pi(V_O + V_m)t\} + cos\{2\pi(V_m + V_o)\, t\}] \tag{5.12}$$

According to classical theory, the first term displays an oscillating dipole that radiates light of frequency $V_O$(Rayleigh scattering) whereas the second term corresponds to Raman scattering of frequency$V_m + V_o$ (anti-Stokes) and $V_m - V_o$(Stokes). Therefore, if $\left(\partial_\alpha/\partial_q\right)_o$ is zero the vibration is not Raman active. However, the vibration to be Raman active the rate of change of polarizability with vibration must not be equal to zero. In normal Raman spectroscopy, the excited line ($V_o$) is chosen so that its energy is far below the first electronic excited state. Under normal conditions the Stokes lines are stronger than the anti-Stokes line. Since both give the same information it is customary to measure only the Stokes side of the spectrum [16].

### 5.2.1 Raman Experimental Setup

In this study Raman spectroscopy was used to analyse the samples. The data was collected using a Horiba Jobin-YvonT64000 spectrometer with a 50× objective lens.The excitation laser was an argon-krypton laser with an excitation wavelength of 514.3 nm and a laser

power of 1.5 mW. The spectra were acquired from Raman shifts ranging from 200 $cm^{-1}$ – 1800 $cm^{-1}$. The analysis of the Raman spectra was performed by LabSpec5 software, which enabled the measurement of peak height, position and width.

### 5.3 Scanning Electron Microscopy (SEM)

#### 5.3.1 Description of Technique

Scanning electron microscopy (SEM) is a technique for high-resolution imaging of sample surfaces [17]. The SEM uses electrons for imaging, much as a light microscope uses visible light [17]. SEM can provide information about surface such as sample topography, crystalline structure, chemical composition and electrical behaviour of the samples [18]. The advantages of SEM over light microscopy is that SEM has a higher magnification ( over 100,000X) and greater depth of field up to 100 times compared to light microscopy [17].

Figure 5-7 shows the basic components of a typical SEM, which may be grouped into four categories: (1) the electron column, (2) the specimen (or sample) chamber, (3) Secondary electron detector and backscattering electron detector (4) the vacuum pumping system and (5) the electron control and imaging system.

The SEM generates a beam of incident electrons in an electron column above the sample chamber. The electrons are produced by a thermal emission source, such as a heated tungsten filament, or by a field emission cathode. The energy of the incident electrons can be as low as 100 eV or high as 30 keV depending on the evaluation objectives [17]. These electrons are emitted by the electron gun in the SEM column and are focused into a small beam through a series of electromagnetic lenses onto the sample surface (see Figure 5-7).Scanning coils near the end of the column direct and position the focused beam onto the sample surface [17]. The beam can also be focused at a single point or scanned along a line for X-ray analysis. The beam can be focused to a final probe diameter as small as about 10 Å [17].

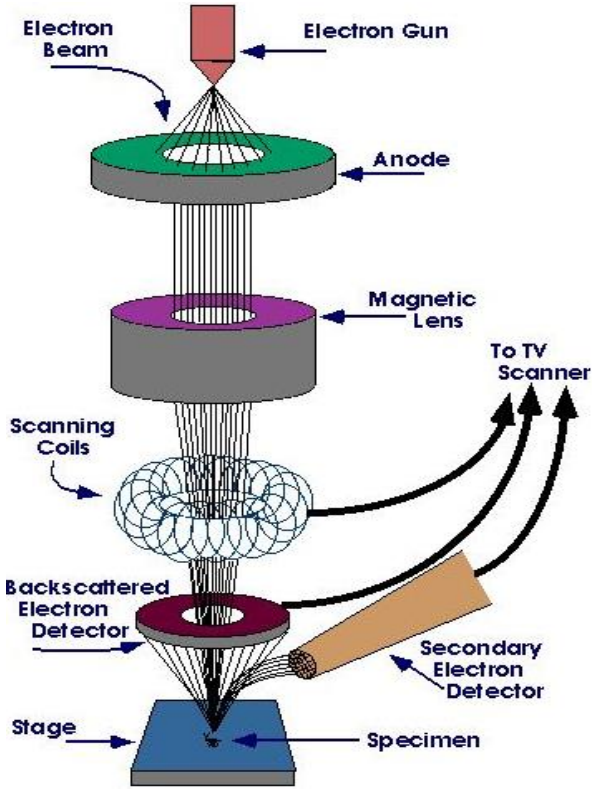


*Figure 5-7: Schematic representation of a scanning electron microscope. Taken from [19].*

### 5.3.2 Electron beam sample interaction and detection

When a beam of incident electrons strikes the surface of the sample and interacts with the atoms of the sample, signals in the form of secondary electrons, backscattered electrons, characteristic X-ray are generated that contain information about the samples surface topography, composition, etc. [19]. The signals emitted by the sample include secondary electrons, backscattered electrons, Auger electrons, X-rays and cathodoluminescence (light) [20] as shown in Figure 5-8. The SEM utilizes these signals to observe and analyse the sample surface (or just beneath the surface)[20].

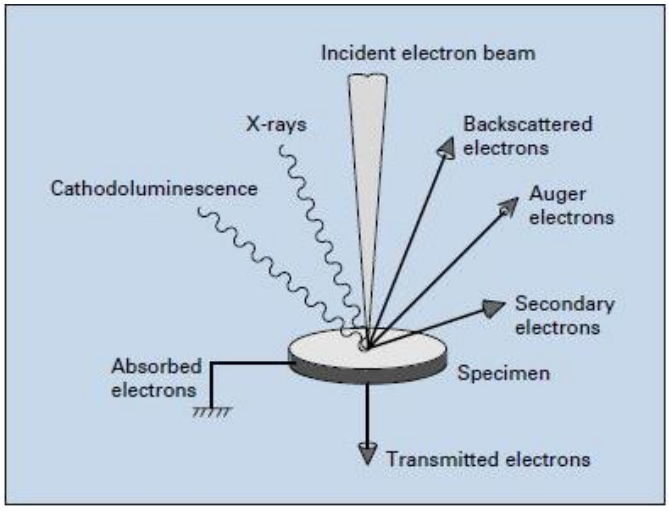


*Figure 5-8: Incident electron beam interaction with the sample and the different type of particles and rays that can be emitted. Taken from [20].*

The incident electrons cause electrons to be emitted from the sample because of elastic and inelastic scattering events within the near-surface region of the material [17]. Figure 5-9 is a schematic diagram that illustrates how various signals are emitted from the sample. High-energy electrons that are ejected by an elastic collision of an incident electron, typically with a sample atom‘s nucleus, are referred to as backscattered electrons [17,21]. The energy of backscattered electrons is comparable to that of the incident electrons [17].

Emitted low energy electrons resulting from inelastic scattering are called secondary electrons. Secondary electrons can be formed from inelastic scattering of the loosely bound valence electrons (in the K-shell) from the sample [17]. The energy of secondary electrons is typically 50 eV or less. To create an SEM image, the incident electron beam is scanned in a raster pattern across the sample's surface [17].

The emitted electrons are detected for each position in the scanned area by an electron detector. The intensity of the emitted electron signal is displayed as brightness on a cathode ray tube (CRT). By synchronizing the CRT scan to that of the scan of the incident electron beam, the CRT display represents the morphology of the sample surface area scanned by the

beam. Magnification of the CRT image is the ratio of the image display size to the sample area scanned by the electron beam [17].

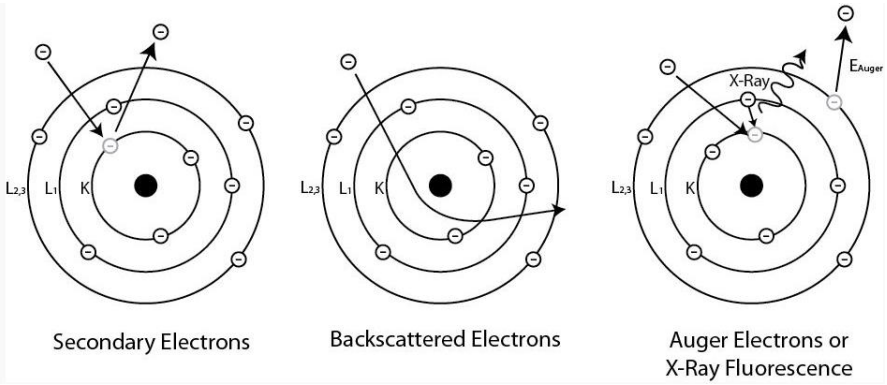


*Figure 5-9: Emission of various signals from the sample. Taken from [21].*

Auger electrons can result from higher energy level electrons filling the vacancies in a lower energy level, the difference in the two energies are carried away through the emission of Auger electrons (low energy electrons) or the production of X- rays. The signals that result from these Auger electrons can be used for chemical analysis of the sample surface. The X-ray signals are used in chemical characterization of the samples by XPS and EDS [22,23].

### 5.3.3 SEM Experimental Setup

In this study, the surface morphology of the ZrC layers and Ir thin films deposited on ZrC was investigated using a Zeiss Ultra 55 field emission scanning electron microscope (University of Pretoria). This microscope is equipped with secondary electron, backscattered electron and in-lens SE detectors. The in-lens detector was used for analysis in this study. The in-lens detector is located in the column above the sample and it is capable of detecting scattered electrons of the surface originating from the impact of the beam. The in-lens detection is often combined with energy filtering of the secondary electrons that form the image. The analysis of the surface for the ZrC layer or Ir-ZrC thin film was done with beam

energy of 2 kV, operating with 0.7 nm spatial resolution to show the surface features. Samples were prepared by placing the ZrC layer or Ir-ZrC on carbon stickers attached to an aluminium holder.

### 5.4 Energy Dispersive X-Ray Spectroscopy (EDS)

#### 5.4.1 Principle of EDS

Energy dispersive spectroscopy (EDS) is a non-destructive quantitative and qualitative chemical microanalysis technique. EDS is normally attached to a transmission electron microscope (TEM) or a scanning electron microscope (SEM). Basically, EDS has the capability of analysing the elemental composition of materials which have atomic number greater than three [22,23].

As shown in Figure 5-10, the physical basis of energy dispersive X-ray spectrometry (EDS) with a semiconductor detector begins with photoelectric absorption of an X-ray photon in the active volume of the semiconductor (Si). The entire energy of the photon is transferred to a bound inner shell atomic electron, which is ejected with kinetic energy equal to the photon energy minus the shell ionization energy (binding energy), 1.838 keV for the Si K-shell and 0.098 keV for the Si L-shell. The ejected photoelectron undergoes inelastic scattering within the Si crystal [24].

One of the consequences of the energy loss is the promotion of bound outer shell valence electrons to the conduction band of the semiconductor, leaving behind positively charged “holes” in the valence band. In the conduction band, the free electrons can move in response to a potential applied between the entrance surface electrode and the back surface electrode across the thickness of the Si crystal, while the positive holes in the conduction band drift in the opposite direction, resulting in the collection of electrons at the anode on the back surface of the EDS detector [24].

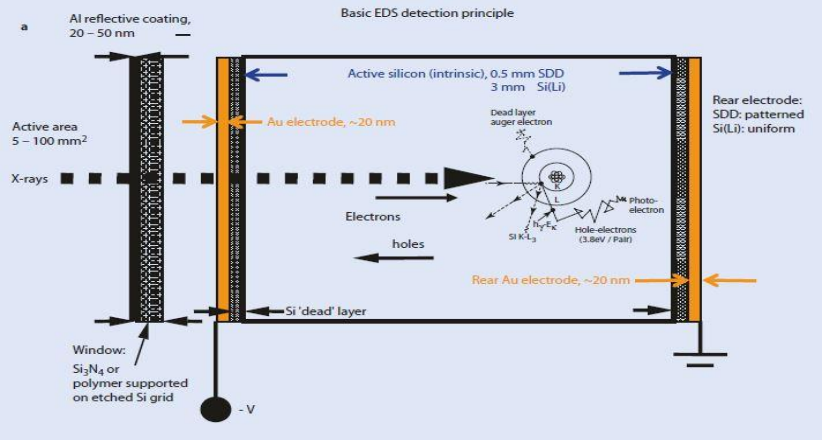


*Figure 5-10: Basic principle of photon measurement with a semiconductor-based energy dispersive X-ray spectrometer. Taken from [24].*

### 5.4.2 EDS detection process

The basic process of EDS detector which is proportional conversion of photon energy into an electrical signal as represented in Figure 5-11. The active portion of the detector consists of intrinsic silicon, with a thin layer of p-type material on the front surface, coated with a thin gold electrical contact. When an energetic photon is captured, electrons are promoted into the conduction band, leaving holes in the valence band. Under an applied bias, these electrons and holes are swept apart and collected on the electrodes on the faces of the crystal [23,25].

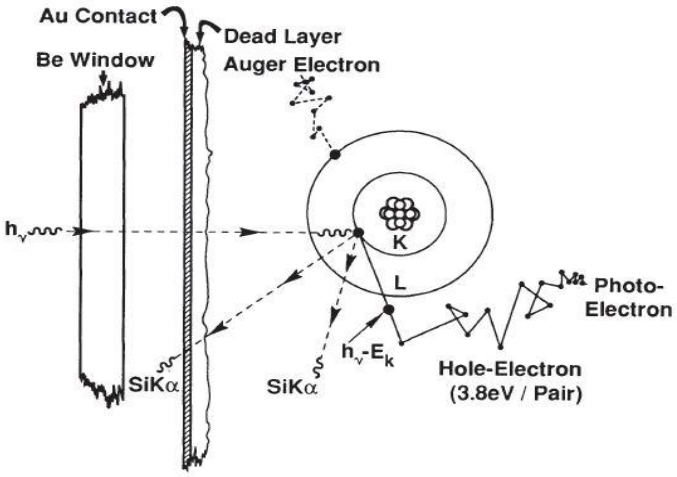


*Figure 5-11: Energy dispersive X-ray detection process in the Si(Li) detector. Taken from* [23,25].

The incident X-ray photon with energy hvis first absorbed by a silicon atom and an inner shell electron is ejected with energy as given:

$$E = hv - E_c \tag{5.13}$$

where$E_c$, for silicon is1.84 keV. Therefore the photoelectron can create electron hole pairs as it travels in the detector silicon and scatters inelastically [23,25].

The silicon atom is left in an excited state because of the vacancies caused by the ejection of the photoelectron. As electrons from less tightly bound states fill the vacancies, energy is subsequently released in the form of either an Auger electron or a silicon X-ray. The Auger electron scatters inelastically and also creates electron hole pairs [23,25]. The silicon X-ray can be reabsorbed, which initiates the process again, or it can be scattered inelastically. Thus, a sequence of events takes place leading to the deposition of all of the energy of the original photon in the detector, unless radiation generated during the sequence, such as a silicon Kα photon escapes the detector giving rise to the artefact known as the "escape peak,"[23,25].

The ideal number of charges *n* created in the detector per incident photon with energy *E* (eV) is given by:

$$n = E/\in \tag{5.14}$$

where ∈ = 3.8 eV for silicon. For example, if the detector captures one photon having energy of 5 keV, then from equation (5.14) the total number of electrons swept from the detector is approximately 1315, which represents a charge of $2\times10^{-16}$ C. This is an extraordinarily small charge. To measure charge accurately, noise minimization is essential, hence the need for keeping the detector crystal close to liquid-nitrogen temperature [25].

Figure 5-12 (a) is a representation of the detector, charge-to-voltage converter (often referred to as a preamplifier), and pulse-shaping linear amplifier from an electronic perspective. Once

created, the charge from the detector is rapidly swept into a virtual ground at the input of an operational amplifier, where it is deposited onto the capacitor, C. The first stage of the preamplifier is a carefully selected low-noise field effect transistor (FET), which is also cooled and placed immediately behind the detector [23,25].

The preamplifier output for each event is a voltage step proportional to the incident photon energy. The height of each step is on the order of a few millivolts and occurs over a period of about150 nanosecond. It is important to recognize that the effect of electronic noise is the introduction of some fluctuation in the output voltage level on both sides of each step. This will be discussed in further detail in the section on factors determining energy resolution. Figure 5-12 (b) displays the output of the charge-to-voltage converter after the detection of a series of X-ray photons. The difference in the step sizes indicates that they have different energies. This energy for each incident X-ray photons as determined from the voltage measurement is then sent to a computer for display and further data evaluation[23,25].

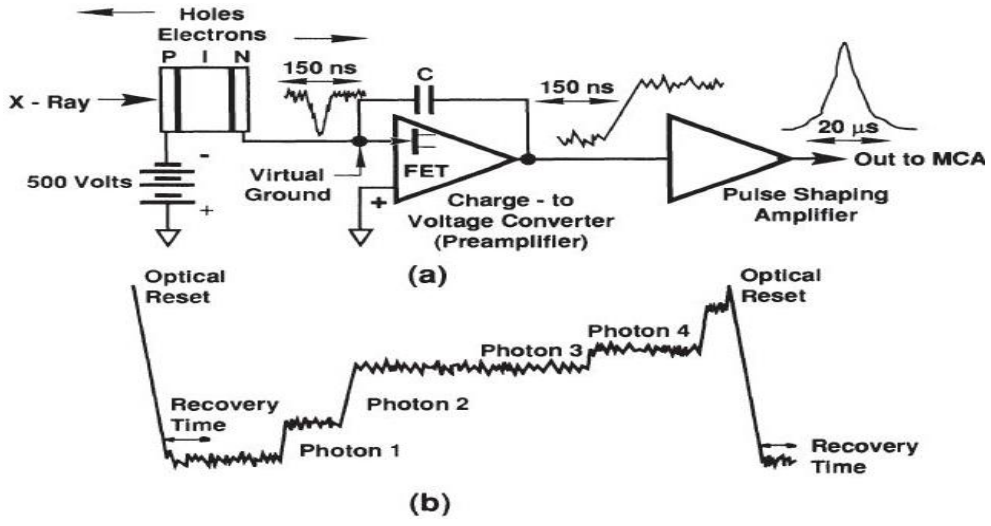


*Figure 5-12: Charge-to-voltage conversion process. (a) Illustration of the detector charge-to-voltage converter, and pulse-shaping linear amplifier from an electronic perspective. (b) Output of the charge-to-voltage converter after the detection of a series of X-ray. Taken from [23, 25].*

### 5.4.3 EDS Experimental Setup

In this study the characterisation of the elemental composition of the ZrC layers was analysed by the EDS instrument at University of Pretoria. This instrument was manufactured by Oxford Instruments. It was mounted on a FE-SEM Zeiss Ultra Plus. The operating voltage while collecting the EDS spectra was set at 20 kV. To cater for inhomogeneity in the sample, six measurements from six different regions on the surface of each ZrC sample were taken. The average of these measurements was taken as the elemental composition of the ZrC sample. The software used generates the elemental composition values as a weight percentage. The weight percentage of each element (i.e. $W_i$ of element) was therefore converted into atomic percentage (*at. %)* by considering the atomic weight of each element (i.e. $A_i$ of element) in the sample composed of *n* elements. This was calculated from Equation (5.15) [26]:

$$At\% = \frac{W_i / A_i}{\sum_{i=1}^{n} W_i / A_i} \times 100\% \qquad (5.15)$$

## References


[1] J.I. Langford, D. Louer, Powder diffraction, Reports Prog. Phys. 59 (1996) 131–234.

[2] M. Eckert, Disputed discovery: the beginnings of X-ray diffraction in crystals in 1912 and its repercussions., Acta Crystallogr. Sect. A Found. Crystallogr. 68 (2012) 30–39.

[3] P. Knipping and M. Von Laue, X-Ray diffraction, (1952).

[4] V. Pecharsky, P. Zavalij, Fundamentals of powder diffraction and structural characterization of materials, Springer, New York, 2003.

[5] Powder X-ray Diffraction, (2012). http://chemwiki.ucdavis.edu/A nalytical_Chemistry /Instrumental_Analysis / Diffraction/Powder_X-ray_ Diffraction (accessed May 31, 2012).

[6] C.. Neugebauer, Condensation, Nucleation and Growth of Thin Films, in: H. Frey, H.R. Khan (Eds.), Handb. Thin-Film Technol., Springer, New York, 1970.

[7] B.D. Cullity, Elements of X-ray diffraction, Addison-Wesley, Reading, 1977.

[8] R.D. Tarey, R.S. Rastogi, K.L. Chopra, Characterization of Thin Films by Glancing Incidence X-ray Diffraction, Rigaku J. 4 (1987) 11–15.

[9] Eric Gitau Njoroge, Solid-state interactions between Zr thin films and SiC, PhD thesis, University of Pretoria, 2014.

[10] P.M. Martin, Handbook of deposition technologies for films and coatings: science, applications and technology, William Andrew, Oxford, 2009.

[11] R.L. McCreery, Raman spectroscopy for chemical analysis, John Wiley & Sons, New York, 2005.

[12] E. Smith, G. Dent, Modern Raman spectroscopy: a practical approach, John Wiley & Sons, 2013.

[13] H.J. Butler, L. Ashton, B. Bird, G. Cinque, K. Curtis, J. Dorney, K. Esmonde-white, N.J. Fullwood, B. Gardner, P.L. Martin-hirsch, M.J. Walsh, M.R. Mcainsh, N. Stone, F.L. Martin, Using Raman spectroscopy to characterize biological materials Using Raman spectroscopy to characterize biological materials, Nat. Protoc. 11 (2016) 664–687.

[14] Introduction to Raman Spectroscopy, (2017). http://bwtek.com/raman-theory-of-raman-scattering/ (accessed August 1, 2017).

[15] D.L. Andrews, A.A. Demidov, An introduction to laser spectroscopy, 2nd ed., Springer, New York, 2002.

[16] J.R. Ferraro, K. Nakamoto, C.W. Brown, Introductory Raman Spectroscopy, Academic press, San Diego, 2012.

[17] L.D. Hanke, Handbook of analytical methods for materials, Materials evaluation and engineering Inc, Plymouth, 2001.

[18] K.D.D. Vernon-Parry, Scanning electron microscopy: an introduction, III-Vs Rev. 13 (2000) 40–44.

[19] M. Joshi, A. Bhattacharyya, S.W. Ali, Characterization techniques for nanotechnology applications in textiles, Indian J. Fibre Text. Res. 33 (2008) 304–317.

[20] S.A. Technology, Scanning Electron Microscope A To Z Basic Knowledge For Using The SEM, www.jeolusa.com (accessed February 15, 2015)., JEOL USA Electron Opt, 2009.

[21] Microscopy, (2017). https://sites.ualberta.ca/~ccwj/teaching/microscopy/ (accessed August 1, 2017).

[22] J.I. Goldstein, D.E. Newbury, P. Echlin, D. Joy, D.R.J. Alton, C. Lyman, F. Charles, E. Lifshin, Handbook of Scanning Electron Microscopy and X-Ray Microanalysis, Plenum, New York, 1981.

[23] J.I. Goldstein, D.E. Newbury, C.E. Lyman, D.C. Joy, Scanning Electron Microscopy and X-Ray Microanalysis, Plenum , New York, 1992.

[24] J.I. Goldstein, D.E. Newbury, J.R. Michael, N.W.M. Ritchie, J.H.J. Scott, D.C. Joy, Scanning Electron Microscopy and X-Ray Microanalysis, Plenum, New York, 2017.

[25] D. Newbury, D. Joy, C. Lyman, P. Echlin, E. Lifshin, J. Michae, J. Goldstein, D. Newbury, D. Joy, I. Charles, Scanning Electron Micros id X-Ray Microanalysis, Plenum, New York, 2003.

[26] S. Biira, Construction of a chemical vapour deposition reactor and the deposition of ZrC layers, PhD thesis, University of Pretoria, 2017.

# Chapter 6. Results and Discussion

In this study, some ZrC layers were grown on to graphite substrates by chemical vapour deposition (CVD) at temperatures between 1250 °C and 1450 °C and others (ZrC samples) were prepared by spark plasma sintering (SPS) at 1700 °C, 1900 °C and 2100 °C. Both as-deposited and sintered ZrC were characterized by XRD, EDS, Raman and SEM. To investigate the interaction between Iridium and ZrC, Ir layers were deposited on the sintered ZrC. The as-deposited Ir-ZrC samples were annealed at 600 °C and 800 °C in vacuum. The as-deposited Ir-ZrC samples and annealed Ir-ZrC were characterized by XRD and SEM. This chapter discusses the results.

## 6.1 As-deposited samples by CVD

### 6.1.1 Growth rate of ZrC layers

The deposition rate $k$ of the ZrC layers was calculated from the rate of the increase of the layer thickness based on the mass $M$ of the layer after a time $t$, viz.

$$k = M / \rho A t \qquad (6.1)$$

where $A$ is the surface area and $\rho$ is the density of ZrC of 6.73 g $cm^{-3}$. In this calculation it is assumed that layer thickness increases uniformly with time. The experimental parameters and results are summarized in Table 6-1. The deposition rates are plotted on a logarithmic scale in Figure 6-1. The errors bars indicated in the figure were calculated from the uncertainties in the sample areas (i.e. deposited areas).

*Table 6-1: The experimental parameters and results of the CVD deposition process.*

| Temp. (°C) | $CH_4$ flow rate (sccm) | $H_2$ flow rate (sccm) | Ar flow rate (sccm) | $ZrCl_4$ flow rate ($gh^{-1}$) | Molar ratio $CH_4/ZrCl_4$ | Deposition rate (µm/h) | Grain size (nm) |
|---|---|---|---|---|---|---|---|
| 1250 | 10.80 | 853 | 562 | 1 | 6.14 | 4.2 | 19.90 |
| 1300 | 15.80 | 853 | 562 | 1 | 8.83 | 5.3 | 24.59 |
| 1350 | 27.11 | 853 | 562 | 1 | 15.24 | 6.4 | 28.47 |
| 1400 | 38.50 | 853 | 562 | 1 | 21.75 | 7.2 | 25.77 |
| 1450 | 44.30 | 853 | 562 | 1 | 24.44 | 9.3 | 26.18 |

Different deposition mechanisms at different temperatures can occur during CVD growth. These mechanisms are manifested by differences in the apparent activation energy for the deposition rate in the different temperature regimes using an Arrhenius plot. From the Arrhenius plot in Figure 6-1, apparent activation energy of 19.8 kcal/mol was obtained from the deposition rates at different temperatures using the Arrhenius law:

$$k = Aexp\left(-\frac{E_a}{RT}\right) \tag{6.2}$$

where $k$ is the deposition rate, $A$ is a constant, $E_a$ is the apparent activation energy, $R$ is the gas constant, and $T$ is the deposition temperature.

The data fits well with a straight line indicating a single deposition mechanism. This value is in reasonable agreement with the 15.8 kcal/mol. obtained by Kim et al. [1] in basically the same temperature range. They regarded their deposition mechanism to be controlled by surface reactions. When using slightly different set of growth conditions (different flow rates), a different value for activation energy of 12.0 kcal/mol. was obtained which is still greater than 10 kcal/mol. This difference is expected because of the slightly different growth conditions. The fact that 12.0 kcal/mol. is greater than 10 kcal/mol. again confirms that this deposition mechanism was controlled by surface reactions.The deposition mechanism has been reported to be

controlled by surface reactions when the activation energy is between 10 and 50 kcal/mol. and by mass transport mechanism for activation energies less than 10 kcal/mol.[2].

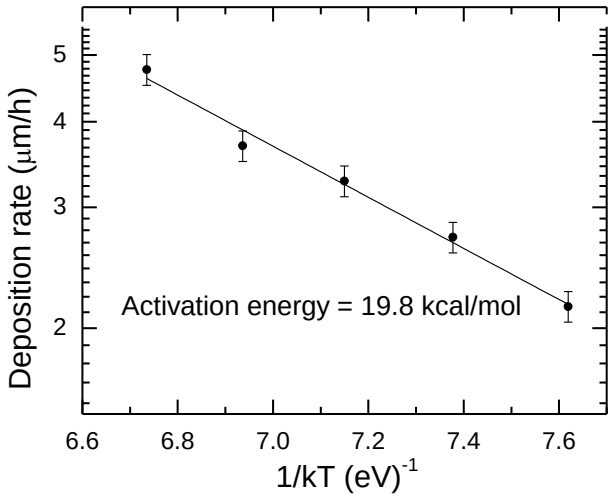


*Figure 6-1: Arrhenius plot of the deposition rate of ZrC layers grown by CVD at various deposition temperatures.*

In contrast, Park et al. [3] found two different growth temperature regimes. Below 1623 K they found an activation energy of 11.46 kcal/mol (therefore also a surface reaction controlled deposition mechanism) while above this temperature the apparent activation energy was 2.99 kcal/mol. Since the latter activation energy was below10 kcal/mol, they ascribed the layer growth mode to be controlled by a mass transport reaction mechanism for temperatures above 1623 K. Although, they did not calculate any activation energy, Biira et al. [4] also found a kink in an Arrhenius plot of their growth rate. At the lower temperatures the slope (related to the activation energy) was higher than the slope at the higher temperatures. The results of these last two papers (i.e. [3] and [4]) are in contrast to those of Liu et al. [5] which reported a very high activation energy of 305 kJ/mol (72.9 kcal/mol) at deposition temperatures above 1523 K and a lower activation energy of 85 kJ/mol (20 kcal/mol) at lower temperatures.

### 6.1.2 XRD results

#### 6.1.2.1 Phase and composition

Figure 6-2 shows the XRD pattern of the ZrC layers deposited at different temperatures ranging from 1250 °C to 1450 °C. The observed diffraction peaks, indicated by (+) in Figure 6-2, at 2θ° positions of 32.9°, 38.2°, 55.1°, 65.7°, 69.1°, 81.8°, 91.0°, 94.1°, 106.6° and 116.5° were indexed to the (111), (200), (220), (311), (222), (400), (331), (420), (422), and (511) ZrC diffraction planes, respectively. This was done using the International Center for Diffraction Data (ICDD) file number ZrC: 03.065–8833, thus confirming the deposition of polycrystalline ZrC layers. Other diffraction peaks, indicated by (*) in Figure 6-2, observed at 2θ° positions of 26.6°, 42.8°, 44.4°, and 77.5° corresponded to the (0002), $(10\bar{1}0)$, $(10\bar{1}1)$,and $(10\bar{1}2)$ diffraction planes of graphite. This confirmed the presence of free carbon in the form of graphite co-deposited in the ZrC layers when matched with ICDD file number C: 00-008-0415. As will be discussed later, Raman spectroscopy showed that this was disordered graphite. The origin of the free carbon/graphite comes from two competing reactions which took place during deposition as given below:

$$CH_4\,(g) \rightarrow C + 2H_2 \tag{6.3}$$

$$ZrCl_4 + C + 2H_2 \rightarrow ZrC + 4HCl \tag{6.4}$$

Some of this carbon was deposited as carbon and some reacted with $ZrCl_4$ to form ZrC.

The graphite peak at 2θ = 26.6° shifted towards smaller angles with increase in temperature. This can be attributed to convolution/overlapping of the two phases, that is, graphite and the carbon peak located at about 26.2°.

Li et al. [6] also observed a skewed broadening of the 26.6° XRD graphite peak when ball milling their graphite samples. When graphite [7] and carbon nanotubes [8] were compressed to high pressures in a diamond anvil, there were significant changes in the XRD patterns. For

graphite the XRD peaks in the 2θ range of 5 to 18° (unfortunately the range covered in this study is not shown) became increasingly broadened with a shifting of the peaks.

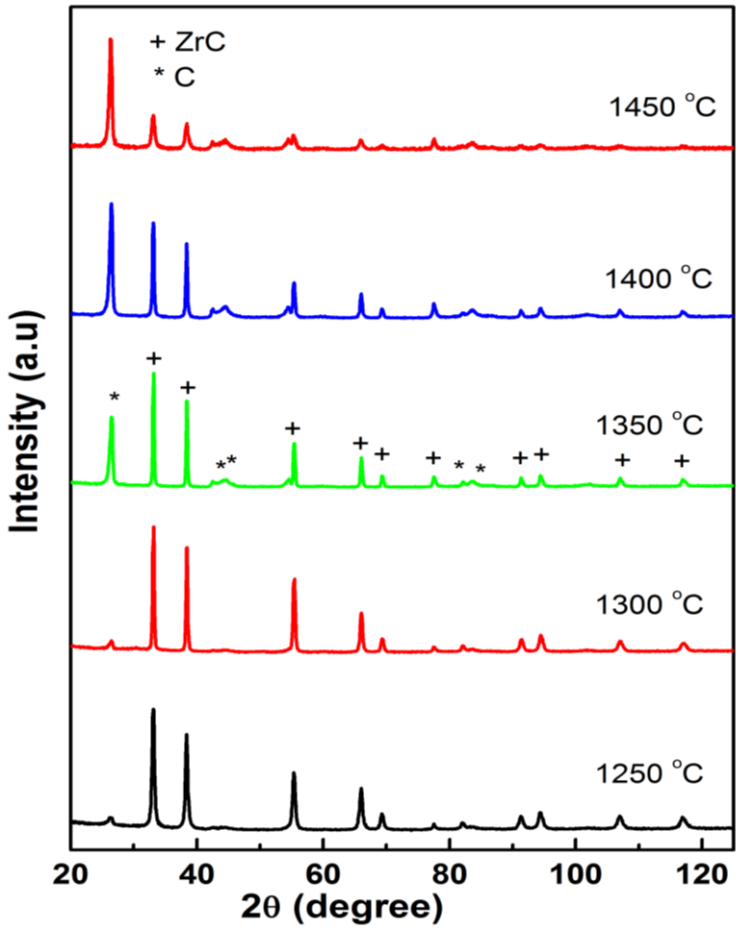


*Figure 6-2: XRD patterns of ZrC layers deposited at different temperatures by CVD.*

These changes were accompanied by a distortion of the basal planes as half of the π-bonds were transformed into σ-bonds. Under pressure the carbon nanotubes transformed into hexagonal carbon with a symmetry space group *P*6_2*c* (no. 190). As will be shown later in this chapter, the free graphite pockets in this samples have sizes in the order of 11.50 nm to 17.96 nm at 1250 °C to 1450 °C respectively. From elementary physics it is known that the pressure in a cavity with radius *r* is proportional to 1/*r*. Therefore, it can be concluded that the skewed broadening of XRD peak at about 26° is due to an increase in pressure when confining the graphite to small cavities inside the ZrC matrix.

#### 6.1.2.2 Rietveld analysis

The results of a Rietveld analysis on the XRD patterns at the different growth temperatures are shown in Table 6-2. The weighted-profile R value, Rwp, which is a measure of the accuracy of the fitting of the calculated profile to the experimental diffraction pattern, is shown in the last column [9]. The column, denoted by carbon, represents the remaining elements and compounds in the sample apart from graphite and ZrC. It also does not represent the high pressure hexagonal carbon phase mentioned in the previous paragraph. EDS analysis on these samples basically agreed with the XRD results in that the only two elements present were Zr and C except at the two lowest temperatures where oxygen was also detected. Therefore, based on EDS analysis the carbon column gives mostly elemental carbon, the high pressure hexagonal carbon phase in the samples and also an oxide phase at the two lowest growth temperatures due to the well-known gettering properties of ZrC [10,11]. Using TEM analysis, Kim et al. [1]found free carbon in their CVD-grown ZrC layer between temperatures of 1200 °C to 1500 °C.

*Table 6-2: Relative percentage of the crystalline phases calculated by the Rietveld method.*

| Growth temperature (°C) | Graphite (wt %) | ZrC (wt %) | Carbon (wt %) | Rwp |
|---|---|---|---|---|
| 1250 | 13.2 ±3.2 | 78.6 ± 3.3 | 8.3 ± 1.6 | 10.45 |
| 1300 | 12.1 ± 2.9 | 77.3 ± 2.9 | 10.6 ± 2.9 | 11.10 |
| 1350 | 12.1 ± 2.3 | 76.8 ± 2.3 | 11.1 ± 1.5 | 10.43 |
| 1400 | 30.3 ±3.9 | 54.5 ±2.8 | 15.2 ± 1.8 | 12.50 |
| 1450 | 45.5 ± 2.5 | 34.1 ± 1.7 | 20.3± 1.9 | 19.00 |

From Table 6-2 it can be seen that at the three lowest temperatures (i.e. up to the deposition temperature of 1350 °C) the carbon and graphite concentrations remained about the same. However, at the two highest temperatures the graphitic and elemental carbon concentrations increased with increasing deposition temperature. (The EDS analyses showed an increase in

the C/Zr ratio with increasing temperature.) As was pointed out above, the origin of this carbon is from the decomposition of methane into carbon and hydrogen at the high temperatures in the reactor vessel near the sample substrate. The solid carbon was deposited on the substrate where most of it reacted with the $ZrCl_4$ to form ZrC with the rest remaining as graphite inclusions and elemental carbon.

In agreement with these results, there are other experimental studies which also found an increase in carbon with increasing temperature by Kim et al. [1], Park et al. [3], Biira et al. [4], Wang et al. [12] and Fukuda et al. [13]. Transmission electron microscopy results by Sun et al. [14] confirmed that the graphite in the CVD grown ZrC layers is in the form of turbostratic carbon, i.e. highly disordered graphite. The result of the increase in graphite with increasing temperature does not agree with thermodynamic calculations by Biira et al. [15], which showed that there should be an increase in ZrC formation with increasing temperature with a corresponding decrease in free carbon from the decomposition of the methane. However, Kim et al. [16] found that the increasing co-deposition of carbon can be linked to a decrease in $ZrCl_4$ supply at the deposition substrate when using a static vaporizer (as was the case in this study). To compensate for this effect they used an impeller-driven vaporizer. Biira et al. [17] also found that decreasing $ZrCl_4$ partial pressures in the reactor vessel led to increasing free carbon in their deposited ZrC layers. In this study, there was ZrC deposition on the hot reactor walls, which increased with increasing temperature. This deposition on the walls resulted in a decrease in $ZrCl_4$ supply at the deposition substrate. This then led to the increase in free carbon, in the form of graphite, the high pressure hexagonal carbon phase and elemental carbon, in the deposited ZrC films at the higher temperatures.

The precipitation of free carbon has an additional effect on the properties of the ZrC layers. According to the review paper by Katoh et al. [18], the value of lattice parameter of ZrC usually depends on the Zr/C ratio with the lattice parameter of $ZrC_{0.96–1.0}$ being about 0.4698

nm. However, carbon-rich ZrC shows no significant dependence of the lattice parameter on the C/Zr ratio. This has been attributed to the precipitation of excess carbon when the C/Zr ratio exceeds 0.98. The carbon-rich ZrC layers from this study layers agree with this non-dependence of the lattice parameter on the ZrC ratio. The lattice parameter was calculated from the XRD data using the Bragg equation for the major ZrC peaks at 2θ equal to 33.1, 38.4, 55.3, 66.0 and 69.3° at each deposition temperature. Although the above Rietveld analysis (see Table 6-2) showed differences in the carbon concentrations, and therefore in the ZrC ratios, at the different deposition temperatures, there were no trends in the lattice parameter data to show either a temperature dependence or a ZrC peak dependence. Taking the average of these 5 measurements, a value for the lattice parameter of 0.46838 ± 0.00091 nm was obtained. Although EDS showed that there were small amounts of oxygen in the samples manufactured at the two lowest temperatures, the lattice parameters calculated for these layers did not deviate from those calculated for the layers deposited at the higher temperatures. This is in contrast to reports which showed that oxygen and other impurities also reduce the lattice parameter [18].

### 6.1.3 Raman results

Additional evidence that there were graphite inclusions in the deposited ZrC layers came from Raman spectroscopy analysis. Figure 6-3(a) shows the Raman spectra of the graphite substrate and ZrC layers deposited at different temperatures in the range of 1250 °C to 1450 °C. The spectra show two prominent Raman peaks, the D-peak at 1350 $cm^{-1}$ and the G-peak at 1582 $cm^{-1}$. The G-peak corresponds to the basal plane vibrations of the graphitic carbon atoms while the D-peak corresponds to the out-of plane vibrations of displaced carbon atoms, i.e. the disordered carbon bonds reported by Ferrari et al. [19]

Due to the NaCl-type structure of stoichiometric ZrC, it has no first-order Raman peaks. However, it is known that defects in ZrC can break the local symmetry and thereby give rise to the appearance of Raman bands. These can arise either from ion bombardment of ZrC as shown in [20] or carbon vacancies in CVD grown Zr [16] or even oxygen interstitials [21]. To eliminate the dominance of the D and G-peaks, the Raman spectra were re-plotted in the wave number range of 200 to 1000 $cm^{-1}$ in Figure 6-3(b). The Raman peaks due to carbon vacancies, viz. the acoustic branches at about 210 $cm^{-1}$ and 280 $cm^{-1}$ and the optical branches at about 540 $cm^{-1}$ and 600 $cm^{-1}$ were not really visible, indicating that the ZrC layers were mostly stoichiometric or, at least, relatively free of carbon vacancies.

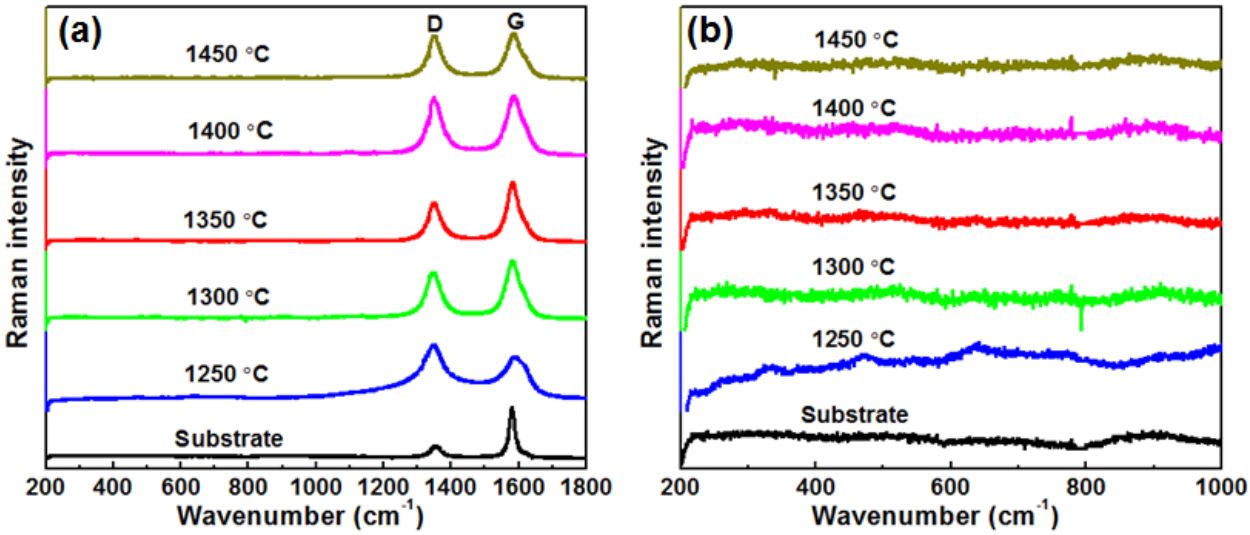


*Figure 6-3: The Raman spectra of (a) the graphite substrate and zirconium carbide layers deposited at different temperatures in the range of 1250 to 1450 °C, and (b) the corresponding Raman spectra in the wave number range of 200 to 1000 $cm^{-1}$.*

Often the two carbon peaks can be deconvoluted into sub-peaks. The results of such a deconvolution are shown in Figure 6-4 for the graphite substrate (a) and ZrC deposited at the different temperatures (b)-(f). A Lorentzian function was used for the fitting of the D, D″, D‴ and a low intensity peak at 1100 $cm^{-1}$, and a Breit–Wigner–Fano (BWF) function for the G peak and D′ peak. In this procedure the peak position (i.e. the wave number) of each peak

was kept constant for the substrate and for each annealing temperature. The results are summarized in Table 6-3. The $R^2$ values for the fitting were excellent and varied from 0.994 to 0.999.

*Table 6-3: A summary of the peak parameters and the results of the deconvolution of the Raman peak for carbon into sub-peaks.*

| | **Peak position ($cm^{-1}$)** | **Fitting function** | | **Substrate** | **Temperature (°C)** | | | | |
|---|---|---|---|---|---|---|---|---|---|
| | | | | | **1250** | **1300** | **1350** | **1400** | **1450** |
| G | 1582 | BWF | Height | 290.9 | 348.9 | 174.3 | 230.1 | 161.5 | 197.0 |
| | | | FWHM | 20.3 | 69.3 | 46.7 | 40.1 | 49.4 | 46.6 |
| D | 1350 | Lorentzian | Height | 66.2 | 426.7 | 144.3 | 150.3 | 155.3 | 188.3 |
| | | | FWHM | 35.0 | 83.1 | 51.8 | 45.6 | 50.1 | 46.7 |
| D' | 1612 | BWF | Height | 13.7 | 55.9 | 30.5 | 29.9 | 37.6 | 46.9 |
| | | | FWHM | 16.0 | 20.6 | 31.3 | 24.4 | 31.3 | 34.0 |
| D'' | 1490 | Lorentzian | Height | | 59.2 | 3.5 | 3.0 | 0.8 | |
| | | | FWHM | | 183.5 | 45.0 | 143.8 | 80.6 | |
| D''' | 1215 | Lorentzian | Height | | 54.5 | | | | |
| | | | FWHM | | 140.3 | | | | |
| Lowint ensity | 1100 | Lorentzian | Height | | | 7.7 | 7.0 | 5.7 | 8.2 |
| | | | FWHM | | | 256.1 | 81.3 | 127.9 | 85.8 |

Phonon modes in the density of states of graphitic carbon materials are the origin for the weak intensity band at 1100 $cm^{-1}$ as reported by Nemanich et al. [22]. The D''' band (1215 $cm^{-1}$) is related to the lattice vibrations of $sp^2$-$sp^3$ bonds as reported by Sadezky et al. [23]. It has only a very weak presence in the Raman spectrum of the 1250 °C ZrC. The D″ band (1490 $cm^{-1}$) originates from the amorphous carbon as shown by Sadezky et al. [23] and as can be seen from Table 6-3 is only prominent for the 1250 °C ZrC layer. The D′ band (1612 $cm^{-1}$), which is seen as a shoulder on the G band, corresponds to a graphitic lattice mode with $E_{2g}$ symmetry [23,24] and is present in graphitic carbons with very small size of $sp^2$ domains[25]. Dresselhaus et al. [26] identified this band in the Raman spectra of carbon intercalation compounds as a perturbation to the graphite lattice (i.e. $E_{2g}$) mode structure. It originates as a graphite boundary layer adjacent to an intercalant layer. This mode fits for graphite inclusions in a ZrC matrix.

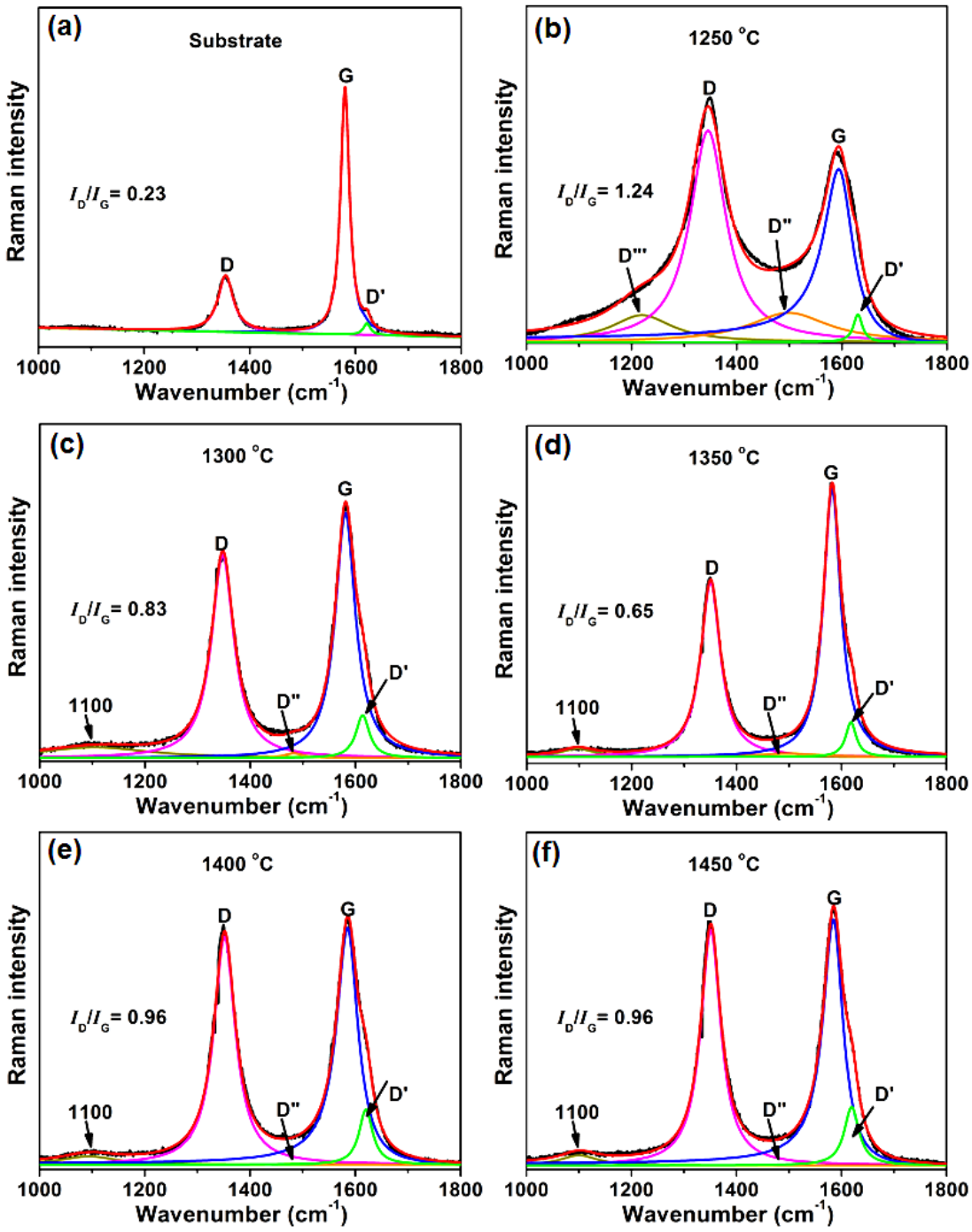


*Figure 6-4: (a) The Raman spectrum of the graphite substrate and (b-f) Raman spectra of zirconium carbide layers deposited at different temperatures from 1250 to 1450 °C. The Lorentzian fitting results of D (indicated by the purple line), D' (light green line), D'' (yellow), D''' (green) and low intensity peak at 1100 cm$^{-1}$ (brown-green), and a BWF fitting of G peak (blue) and D' peak (light green) are also included. The experimental curve is given in black while the sum of all the fits is a red line.*

A measure of the degree of graphitization of carbonaceous materials can be obtained from the ratio of the intensity of the D and G peaks (i.e. the $I_D/I_G$ ratio). From the data in Table 6-3 the $I_D/I_G$ ratio of the graphite substrate is 0.22 which indicates that the substrate had a high degree of graphitic crystalline structure. For the ZrC layer deposited at 1250 °C this ratio increases to 1.22 suggesting that the co–deposited carbon has a low degree of graphitic crystalline structure. However, as the deposition temperature increases, the degree of graphitic crystallinity improves, i.e. $I_D/I_G < 1$. This observation of the increase in the graphitic crystallinity with temperature is in agreement with other studies, e.g. [1,12].

The CVD growth of ZrC and graphite is a complex system, with competition between the ZrC grains and graphite inclusions growth. However, this result can be explained by a simple model. Increasing the temperature leads to an increase in the mobility of the deposited atoms, including the carbon atoms, on the depositing surface. This means that at higher deposition temperatures, the free (i.e. unreacted) carbon atoms can move to preferred carbon lattice sites in the carbon inclusions, thereby improving the crystallinity.

### 6.1.4 Crystal sizes

Average crystal sizes of a polycrystalline substrate can be obtained from the XRD spectra using Scherrer's equation [27]:

$$D = \frac{K\lambda}{\beta \cos\theta} \tag{6.5}$$

where $D$ is the average crystallite size, $\beta$ is the full width at half maximum (FWHM) of the diffraction peak (the correction for the instrumental broadening was done), $\theta$ is the Bragg angle, $K$ is a constant (a value of 0.94 was used), $\lambda$ = 1.5406 Å is the wavelength of the excitation X-rays. To calculate the average sizes of the ZrC grains in the deposited layers, the same major ZrC diffraction peaks as for the lattice parameter were used and the average of them were taken for each deposition temperature. The results are shown in Figure 6-5. The

overall trend is an increase in crystal size with increasing temperature. It is well known that the average grain size of a film increases with increasing temperature as reported by Thompson et al. [28]. This is due to the increasing mobility of the atoms at higher temperature. A surface atom from one grain can diffuse to another nearby crystallite leading to shrinking of the donor grain and growth of the receiver grain. The surface diffusion depends on the surface energy of the atoms. A part from the different energies for different crystal surfaces, the surface energy per atom for a specific crystal plane also scales with the grain surface to volume ration as shown by Thompson et al. [28]. Surface atoms in small grains will have a higher energy compared to those in large grains leading to an enhanced diffusion from these smaller crystallites to the larger ones Zinke-Allmang et al. [29]. Therefore, these different surface energies lead to an increase in the average size of the grains – an Ostwald ripening process. This preferential growth of some grains forms part of a general class of growth of non-equilibrium systems showed by Stavans et al. [30].

However, as can be seen in Figure 6-5, the average crystal size reached a maximum at a deposition temperature of 1350 °C. From the Rietveld analysis discussed in the previous section (see Table 6-2), it follows that the graphite and carbon concentrations were about the same for the three lowest temperatures. At the two temperatures above 1350°C, these two concentrations increased significantly. The “free” carbon atoms will inhibit the grain growth because according to the step-flow model of crystal growth, any impurity will limit the growth of a crystal, resulting in smaller crystallite sizes in a polycrystalline material as reported by Burton et al. [31]. This has been verified experimentally because it is well known in metallurgy that impurities or second phase particles are very effective in altering and eventually inhibiting grain growth [32].

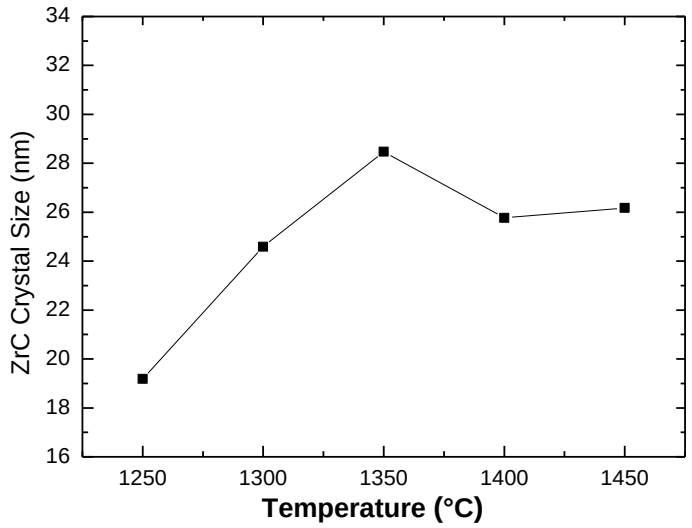


*Figure 6-5: Average crystal size of the ZrC grains at each deposition temperature as determined by the Scherrer equation.*

There have not been many reports on ZrC crystal sizes in the literature. In previous studies, the reported crystal sizes varied from about 22 to 34 nm by varying different deposition parameters such as the gas-inlet gap [33], $ZrCl_4$ partial pressure [17]. The ZrC crystal size obtained in this study agrees with these investigations. A few other studies also reported similar results i.e. 10–50 nm [14], and 11 nm [34]. However, when incorporating ZrC layers (deposited at 1500 °C in nuclear TRISO fuel particles, Kim et al. [16,35]reported that their ZrC size distribution was between 100 – 300 nm, which is much larger than the ones reported in this study.

The average size of the graphite crystallites was also calculated in the same way. Since there was only one major XRD graphite peak, viz, the one at $2\theta = 26.58°$, only this one was used for substitution into the Scherrer equation (6.5). However, as was discussed in section 6.1.3, this graphite overlapped with a carbon 2H peak. By deconvoluting this peak into graphite and a carbon 2H peak, the FWHM for each of these two peaks could be determined and used to determine the average grain sizes of both phases, after correcting for instrumental

broadening. The results are shown in Figure 6-6.The average grain size of the carbon increased monotonically with increasing temperature - as can be expected - while those for the carbon 2H, initially increased with temperature and then at 1350 °C levelled to approximately a constant value. No crystal sizes for the carbon/graphite inclusions in ZrC layers have been reported in the literature.

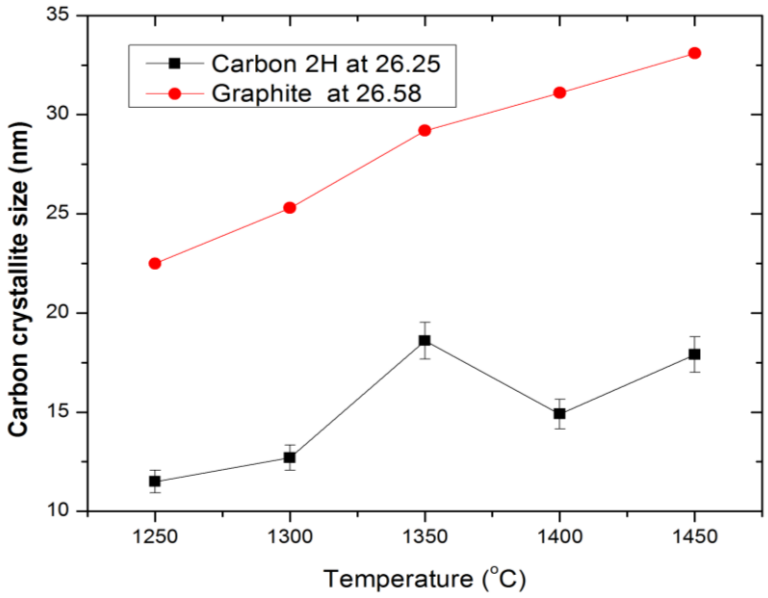


*Figure 6-6: Average crystal size of the graphite (blue) and the carbon 2H (red) grains at each deposition temperature as determined by the Scherrer equation.*

Raman spectra of disordered carbon materials can also be used to extract the crystallite sizes $L_a$ of the graphitic crystallites by using the empirical Tuinstra-Koenig relationship

$$\frac{I_D}{I_G} = \frac{C(\lambda)}{L_a} \tag{6.6}$$

where $I_D$ and $I_G$ are the $D$ and $G$ band intensities respectively, and $C(\lambda)$ is a constant which is laser dependent. Matthews et al. [36] found that this constant is given by $C(\lambda) = -12.6 + 0.033\lambda$ (nm) for the 514.5 nm laser excitation used in this study. Figure 6-5 shows the average (disordered) graphite crystallite sizes at each deposited temperature by using the values given in Table 6-3 for $I_D$ and $I_G$.

The general trend in Figure 6-5 is an increase in the average crystallite size with temperature in agreement with the XRD (Scherrer) results. However, there are also significant differences between these two sets of data. Not only are Raman values much smaller than the XRD ones, but the Raman data has a maximum at a temperature of 1350 °C. This is also the transition temperature above which the total carbon content (including the graphite) in the layer dramatically increased. Zickler et al. [37] compared the predictions of the Tuinstra-Koenig formula with values obtained by the Scherrer formula for XRD spectra. Although their main conclusion was that there was a quantitative discrepancy between the two methods for $L_a < 2$ nm, there were also differences for carbons with different microstructures. They also suggested perhaps the area under peak should be used instead of the peak height (intensity). In Figure 6-7, the crystallite sizes calculated from the area under the curves have been plotted. Essentially both sets of data are within a 10% error bar range.

A very selective investigation of papers, which used the Tuinstra-Koenig formula, showed that in these papers the formula was only applied to predominantly carbonaceous materials. In this study it was used for the analysis of disordered graphitic inclusions in a predominantly carbide matrix. Following a suggestion by Zickler et al. [37], this discrepancy can be used to propose an alternative value for $C(\lambda)$ for turbostratic carbon in a ZrC matrix, However, a more extended range of film composition should be done in order to confirm this value, possibly also an extension to other carbide films.

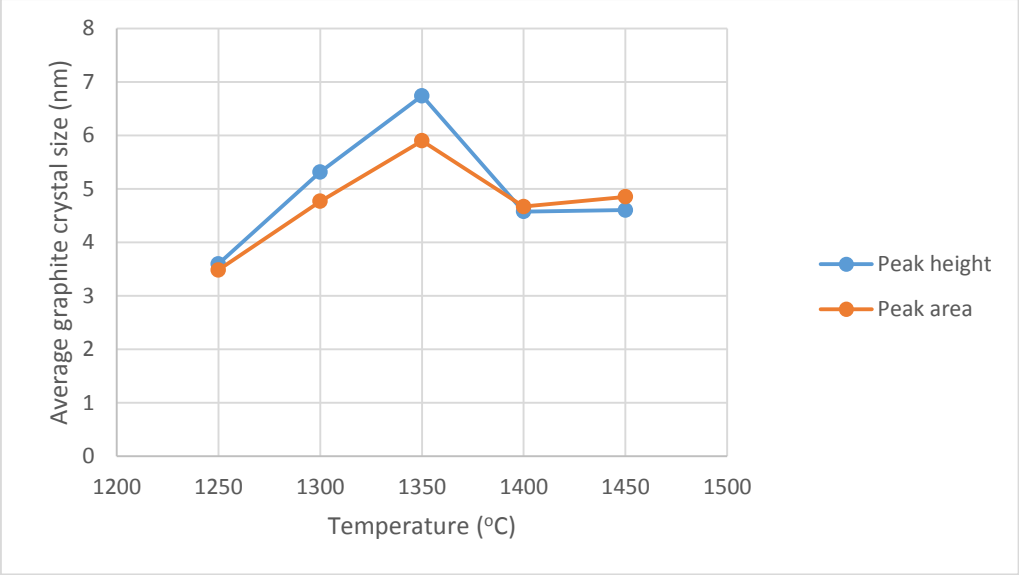


*Figure 6-7: Average graphite crystal sizes as calculated from the Raman spectra using the Tuinstra-Koenig formula. The data using the peak heights (intensities) are shown in blue while the red shows the sizes calculated using the area under the peaks.*

### 6.1.5 Preferred crystal orientations

The preferred orientations of the grains in a polycrystalline material influence the properties of crystalline materials. Therefore, the preferred orientation of the planes of the ZrC grains in the deposited ZrC layers was determined from the texture coefficient of the planes given by equation (5.6). If a value of the texture coefficient is less than one or equal to one, this means that the crystallites are randomly oriented, while a value of texture coefficient greater than one means that the preferred orientation of crystallites are in a given direction [38].

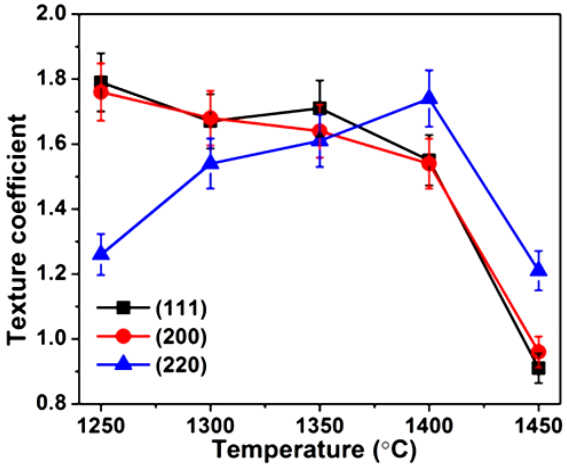


*Figure 6-8: Variation of the texture coefficient for the ZrC grains prepared by CVD technique with deposition temperature.*

Figure 6-8 shows the variation of the texture coefficient of the planes of the as-deposited samples at different deposition temperatures between 1250 °C to 1450°C. It is clear from Figure 6-8 that the curves for the (111) and (200) planes were within experimental error equal to each other. The texture coefficients of these two planes decreased with increasing temperature. At the lower deposition temperatures, i.e. 1250 °C to 1400°C, the texture coefficients of all three planes were greater than one for all the films, implying preferred orientation. For the 1450 °C deposition, the texture coefficients of the (111) and (200) planes decreased to values below 1, indicating no preferred orientation for these two planes. At this temperature, the texture coefficient of the (220) plane was just above 1, viz. 1.2.

There have been a few reports of measurements of preferred ZrC CVD crystal growth. In other reported studies using different growth conditions [33], the (111) preferred orientations were observed in the layers grown at 1200°C and 1400 °C. In contrast to these results in this study, Sun et al. [14] found no preferred orientation in their layers grown at a fixed temperature of 1350 °C. For their layers grown also at a fixed temperature, i.e. 1500 °C, Kim et al. [16] found a (001) preferred orientation. In a temperature range very similar to this study, viz. 1250 °C to 1400 °C, Park et al. [3]reported that the preferred orientation of their

ZrC films changed from (111) to (220) to (200) as the growth temperature increased. When lowering the concentration of the reactive species by adding hydrogen to the Ar carrier gas, the (111) oriented layer changed to a higher surface energy plane, i.e. (200). Lowering the concentration further changed the preferred orientation from (200) to (220) [3]. Kim et al. [1]found that for the low growth temperature of 1200 °C, the lowest energy plane, viz. (111) was the preferred plane to grow. This changed to the higher energy (200) plane when the deposition temperature was 1400 °C.

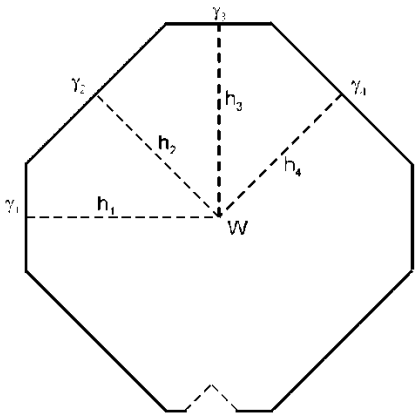


*Figure 6-9: Wulff's construction for the equilibrium form of a free crystal. The bottom plane illustrates how faceting on high index planes occurs according to Wulff's construction.*

To understand and explain the preferred orientation results one must consider the surface energies of the different planes in terms of Wulff's law [39] for equilibrium crystal growth. Wulff's law and Wulff's construction (see Figure 6-9) is based on thermodynamic arguments to explain the shape of crystals under equilibrium growth conditions. Basically it uses the surface energies of the crystal planes and minimization of the Gibbs free energy of the system. The construction is shown in Figure 6-9,

$$\frac{\gamma_1}{h_1} = \frac{\gamma_2}{h_3} = \frac{\gamma_3}{h_3} = \ldots \tag{6.8}$$

where $\gamma_i$ is the surface energy of a particular surface crystal orientation and the different $h_1$, $h_2$ are the lengths of the perpendiculars to these surfaces from a common origin, the so-called

Wulff point *W*. From the equation (6-8), it follows that a crystal surface with a higher surface energy (i.e. more energy is needed to eject the molecule into the vacuum) will grow proportionally faster than another surface with a lower surface energy. This increases the surface area with a lower surface energy, consequently minimizing the total energy of the crystal. In figure 6-9, $h_1 = h_3 > h_2 = h_4$, therefore $\gamma_1 = \gamma_3 > \gamma_2 = \gamma_4$.

For stoichiometric ZrC with a NaCl-type structure $\gamma_{(220)} = 0.85$ J/m$^2$ > $\gamma_{(200)} = 0.69$ J/m$^2$ > $\gamma_{(111)} = 0.52$ J/m$^2$. Thus one would expect that under pure equilibrium growth the ZrC layer would have a preferred (111) orientation. This would typically occur under conditions when the temperature is high enough for the depositing atoms/molecules to have enough mobility and when the growth rate is small enough to prevent competition amongst the atoms/molecules for the available surface lattice positions in line with the step-flow model of crystal growth [31].

At the lowest deposition temperature of this study, the ZrC layers also had this preferred orientation together with the (200) orientation. Deviations from this lowest energy (111) orientation can occur due to either a high deposition rate or the influence of impurities preventing pure equilibrium growth. Since the films contained carbon inclusions, the carbon impurities on the ZrC grain surfaces was probably the main reason for the additional (200) orientation in the films at the lower deposition temperature where the deposition rates were still relatively low. As the temperature increased the deposition rates increased exponentially (see Figure 6-1). This resulted in increasing non-equilibrium growth with reduced crystal orientations. At the highest temperature (1450 $^{o}$C) used in this study, the deposition rate was near the limit of allowing some measure of equilibrium crystal growth with preferred orientations to occur.

### 6.1.6 Surface morphology of ZrC prepared by CVD

It is known that the development of surface morphology is directly linked to the growth mechanisms of the deposited layer which is strongly temperature dependent [40]. During crystal growth, nucleation clusters are formed. These clusters grow larger in line with the step-flow mechanism of crystal growth [31]. As was discussed above, because specific crystallographic orientation have minimum surface and interface energies, clusters with such orientations will grow preferentially leading to certain preferred crystal orientations following Wulff's law [39]. These surface planes can protrude from the surface leading to topography development.

Also discussed above were some of the driving forces of the thin film grain growth namely the minimization of the surface, interface and strain energies between different oriented grains. These lead to preferred surface diffusion controlled by minimization of the Gibbs free energy of the system of grains. Also mentioned was that this leads to an increase in the average size of the grains – an Ostwald ripening process. The parasitic growth naturally leads to a shrinking of the smaller crystals with an eventual disappearance of these crystals. Consequently, cavities develop inside the layer and also on its surface.

It is clear that surface diffusion plays a central role in the development of surface roughening. A factor which can inhibit this specific mechanism is the occurrence of step edge barriers (e.g. the Ehrlich-Schwoebel barrier [41,42]) to surface diffusion [43]. Such barriers also lead to the development of surface topography. They are an important factor in surface topography development during ion bombardment [44].

Low and high magnification SEM images taken with an in-lens detector of the films grown at the different temperatures are shown in Figure 6-10. Because the average sizes of the ZrC and graphite crystals were so small (see section 6.1.5), the topographical effects of the individual

crystals, as discussed above, were not always visible in these images. The low magnification images provide better comparison between the images to ascertain the effect of temperature on the morphology of the layers.

The SEM image of the layer grown at 1250 °C did not show the crystalline nature of the layer as well as the images of the layers deposited at higher temperatures. There are some clusters of crystals visible as the crystals seem to be distributed more randomly in the surface. It seems as if the surface is covered by some amorphous layer an amorphous carbon layer. The deconvolution of the Raman spectra at this temperature showed the presence of the D″ band at 1490 $cm^{-1}$ which originates from amorphous carbon.

The layer deposited at 1300 °C showed more distinct grouping of the crystals in clusters, sometimes with cavities between the clusters. The latter is probably due to the parasitic preferential growth of crystals as discussed above. Also visible in this image are some large clusters on top of the layer, also having a cauliflower appearance. They are reminiscent of SEM images of crystal clusters formed on SiC layers during CVD growth of SiC at very high temperatures [45]. Based on the results and explanations of Chu et al. [45], it is proposed that a similar formation mechanism for the cauliflower shaped crystal clusters. At the high temperatures used in this study, homogeneous nucleation of ZrC molecules in the gas phase is possible due to the increase in intermolecular collisions and the super saturation of the reacting species. The gas phase formed ZrC molecules attached to the substrate via physio-chemical bonding. Subsequent secondary reactions and nucleations occurred on the deposited particle resulting it to grow into the cluster.

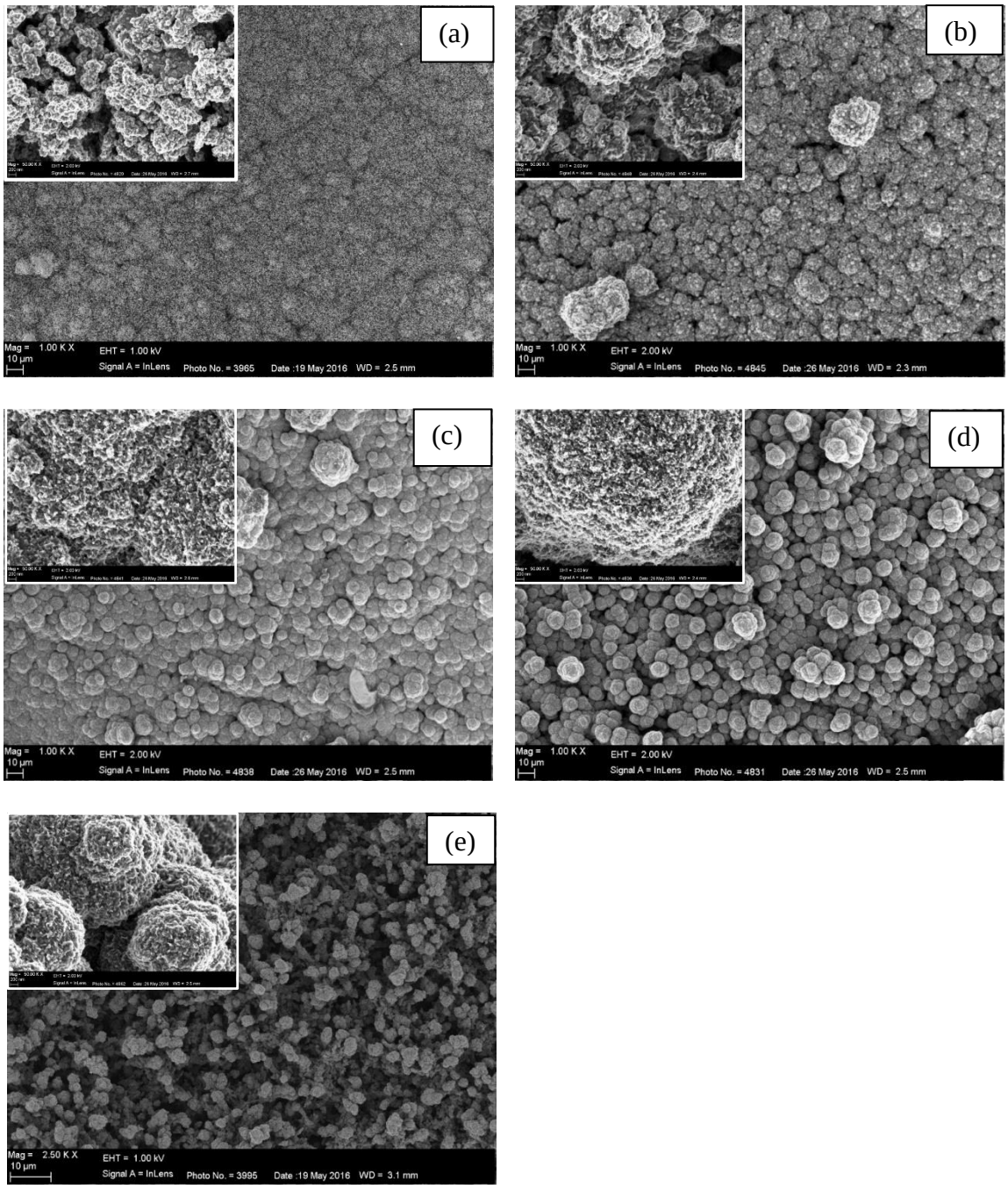


*Figure 6-10: SEM micrographs of ZrC layers deposited on graphite at (a) 1250 °C, (b) 1300 °C, (c) 1350 °C, (d) 1400 °C and (e) 1450 °C.*

This clustering of crystals continued for the layers deposited at 1350 °C and 1400 °C. At 1450 °C the cauliflower appearance disappeared and more cavities due to the parasitic growth of some crystals and crystal planes are visible. The higher magnification images show that this parasitic preferential growth of crystals and planes appeared in all the layers.

## 6.2 Phase formation between iridium thin films deposited on zirconium carbide prepared by spark plasma sintering annealed at relatively low temperatures

### 6.2.1 Introduction

In the second part of this study, zirconium carbide (ZrC) samples were prepared by spark plasma sintering (SPS) from ZrC powder at 1700 °C, 1900 °C and 2100 °C, at 50 MPa for 10 minutes. Thereafter, iridium (Ir) thin films were deposited on the ZrC ceramics by electron beam deposition and annealed in vacuum at temperatures of 600 °C and 800 °C for 2h.

### 6.2.2 X-ray diffraction analysis of ZrC prepared by SPS

The phase composition of the bulk as-sintered ZrC samples was analyzed by X-ray diffraction analysis.The XRD patterns of ZrC samples sintered at 1700 °C, 1900 °C and 2100 °C are shown in Figure 6-11. The diffraction peaks indicate the polycrystalline structure of the SPS synthesised ZrC. Although the three samples had similar peaks, their intensities were observed to vary slightly. Whereas ZrC prepared by CVD consisted mainly of the ZrC phase and some free carbon inclusions (discussed in section 6.1.3), in the SPS prepared ZrC no free carbon was observed since the starting materials were pure ZrC powders. Furthermore, after sintering in the temperature range of 1700 °C to 2100 °C, the XRD patterns of polycrystalline ZrC showed a typical NaCl structure.

The ZrC peaks became slightly sharper at 2100 °C but the peak intensities were slightly lower than those obtained at 1700 °C and 1900 °C. The change in the peak intensity might be due to the change in the ZrC grain size. Comparison between the SPS (Figure 6-11) and CVD (Figure 6-2) ZrC XRD results, it can be observed that the SPS XRD patterns have higher intensities and the ZrC peaks are sharper. This indicates that the pre-formed ZrC powders results in higher crystallinity compared to CVD prepared ZrC. The preferred orientation determined from the texture coefficient of the planes given by equation (6.7) of

the ZrC prepared by SPS at 1700 °C, 1900 °C and 2100 °C was found to be (200). The preferred orientation is probably due to the packing of the powder before sintering occurs.

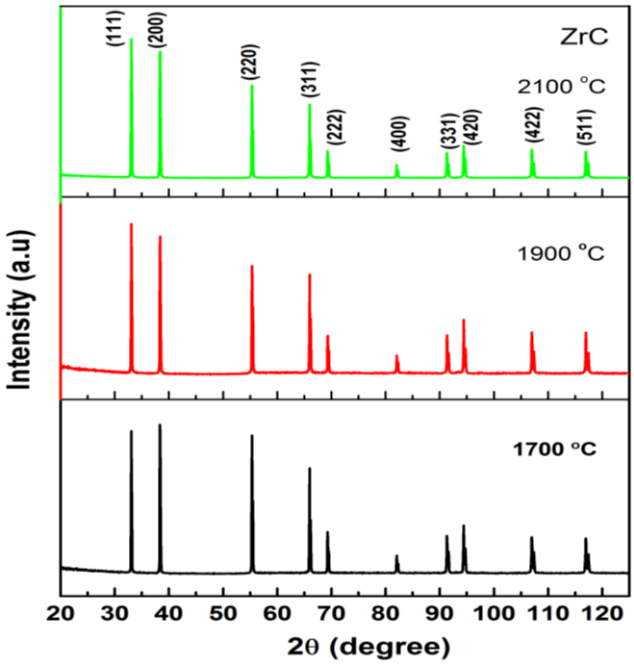


*Figure 6-11: X-ray diffraction patterns of ZrC ceramics prepared by SPS method at 1700 °C, 1900 °C and 2100 °C.*

### 6.2.3 Grain size of ZrC (SPS)

The grain sizes of the ZrC samples were calculated using Sherrers's equation (equation (6.5)). The calculated grain size of the pure ZrC powder (manufactured by Sigma-Aldrich with 99.9% purity and mean particle size of 5 micron). However, the grain size was observed to increase from 71.88 ± 3.6 to 83.59 ± 3.9 nm after sintering from 1700 °C to 2100 °C, at 50 MPa and 10 min, respectively. In comparison to previous studies by Sciti et al. [46,47] who investigated the sinterability of commercial ZrC powders with mean particle size 3.8 µm (they did not report the grain or crystallite size), they obtained dense ZrC ceramics whose grain size increased to 13±1 µm after sintering at 2100 °C, pressure of 65 MPa and time of 3 min. This indicated that the starting materials, sintering conditions used and

the application of very high heating and cooling rates led to higher grain sizes at higher temperatures which enhanced higher densification.

Sciti et al. measured the grain sizes of their SPS prepared ZrC samples through image analysis on SEM micrographs using the Image Pro Plus Software while in this study, the crystallite size was calculated from XRD spectra. These are fundamentally different results and not comparable since a particle often has more than one crystallite, but not necessarily and XRD analysis gives the crystallite size, not particle size.

The overall trend is an increase in grain size with increasing temperature. It is well known that the average grain size of a film increases with increasing temperature as reported by Thompson et al. [28]. This is due to the increasing mobility of the atoms at higher temperature as was discussed in section 6.1.5.

### 6.2.4 Relative density and Vickers hardness

The measured Vickers hardness and relative densities of SPS prepared ZrC samples from this study and reported data are listed in Table 6-4. The relative density is the ratio of the measured density (mass of a unit volume) of ZrC to the reference density of ZrC (6.73 g/cm$^{3)}$.The bulk densities of the as-sintered ZrC samples were measured by Archimedes' technique (using a Micromeritics Accupyc II 1340 fully automated pycnometer at University of Pretoria), this was done after removing the outer layer by polishing. The Vickers hardness was measured on a hardness tester (Rockwell Hardness testing machine at University of Pretoria) with an indentation load of 10 kg and a dwell time of 10 s.

*Table 6-4: Relative densities and hardness of ZrC prepared by SPS at 1700 °C, 1900 °C and 2100 °C compared with the data from other studies.*

| Materials | Sintering conditions ($^{o}$C/min/MPa) | Mean grain size (µm) | Relative Density (%) | Vickers hardness (GPa) | Reference |
|---|---|---|---|---|---|

| | | | | | |
|---|---|---|---|---|---|
| ZrC | 1700/10/50 | 0.072±0.036 | 96.5 | 7.4 ± 0.83 | This study |
| ZrC | 1900/10/50 | 0.079±0.039 | 98.9 | 17.0±0.07 | This study |
| ZrC | 2100/10/50 | 0.083±0.041 | 99.5 | 18.4 ±0.05 | This study |
| ZrC | 1850/10/60 | Around 2 | 85.3 | 9.1± 1.40 | [48] |
| ZrC | 1900/10/60 | <10 | 96.1 | 16.3 ± 1.60 | [48] |
| ZrC | 2100/3/65 | 13±1 | 99.0 | 17.9 ± 0.60 | [46] |

The relative density of ZrC increased with the sintering temperature from 96.6 % at 1700 °C and reached a maximum of 99.5 % at 2100 °C. The relative density of the ZrC ceramics from Sciti et al. [46] after sintering at 2100 °C was about 99 %. They used ZrC powders with mean particle size of 3.8 µm and their sample was sintered for only 3 min but at a higher pressure of 65 MPa. Sun et al. [48] performed reactive spark plasma sintering (RSPS) using zirconium oxide ($ZrO_2$) and carbon black to obtain ZrC whose relative density increased with the sintering temperature and reached 96.1% at 1900 °C. Therefore, as seen from the results in Table 6-4 and the results from other studies [46,48], it can observed that higher densification of ZrC carbide is obtained as the sintering temperature increased. The relative density increases with temperature from 1700 to 2100 °C, and the grains coalesce to form denser clusters. The density did not reach the theoretical density of ZrC which is about 6.73 g/cm$^3$, due presence of minute amounts of free carbon.

Sun et al. [48] and Sciti et al. [46] obtained Vickers hardness values of 16.3 and 17.9 GPa from ZrC sintered at 1900 °C and 2100 °C respectively. The hardness values obtained in this study were 17.0 and 18.4 GPa after sintering ZrC at 1900 °C and 2100 °C respectively. These hardness values are slightly higher compared to those obtained by Sun et al. and Sciti et al. This is due to the longer sintering duration of 10 min at a lower pressure of 50 MPa at 2100 °C compared to 3 min and 65 MPa used by Sciti et al. [46]. It

can be observed that longer sintering durations can lead to lower porosity therefore high density and high hardness values.

### 6.2.5 Scanning electron microscopy (SEM)

The SEM images from the surface of the ZrC samples sintered to different final temperatures allowed the investigation of the microstructure evolution during the SPS. The surface of ZrC sintered at 1700 °C is given in Figure 6-12 (a) and the surface can be observed to be inhomogeneous and coarse. This is due to agglomeration and coalescing of the fine ZrC particles to form larger ones during sintering. This led to a highly porous structure at this sintering temperature. The presence of these pores can explain the lower relative density of the sample obtained (96.5 %).

The structural changes due to sintering at different temperatures can be deduced from the SEM micrographs as seen in Figure 6-12 (b) of ZrC sample sintered at 1900 °C. Although the surface is still inhomogeneous, it is denser with a lower number of pores compared to the sample sintered at 1700 °C. The inhomogeneous surface consists of particles of different sizes. The reduced pore size and density accounts for the increase in relative density of this sample to 98.9% and increase in particle size after sintering at 1900 °C.

The surface of the sample sintered at 2100 °C has fewer and smaller pores compared to the sample prepared at 1900 °C with relative density of 99.5 % which had larger and more pores. The surface looks smoother compared to the 1900 °C and 1700 °C prepared samples and the grains are lying flat on a surface. The SEM micrographs of ZrC sintered at 1900 and 2100 °C illustrate how the ZrC surface morphology changed with the relative density. These changes led to an increase in relative density and hardness from 96.5 and 7.4 GPa at 1700 to 99.5 and 18.4 GPa at 2100 °C, respectively. A more consolidated surface structure appears in

the specimens sintered at higher temperature of 2100 °C (Figure 6-12 (c)).

The sintering temperature determines the level of densification as well as the crystallite size growth. The progress of enhanced densification and crystallization phenomena with increase in the sintering temperature might be due to accelerated surface diffusion and grain boundary diffusion at the higher temperatures [49].

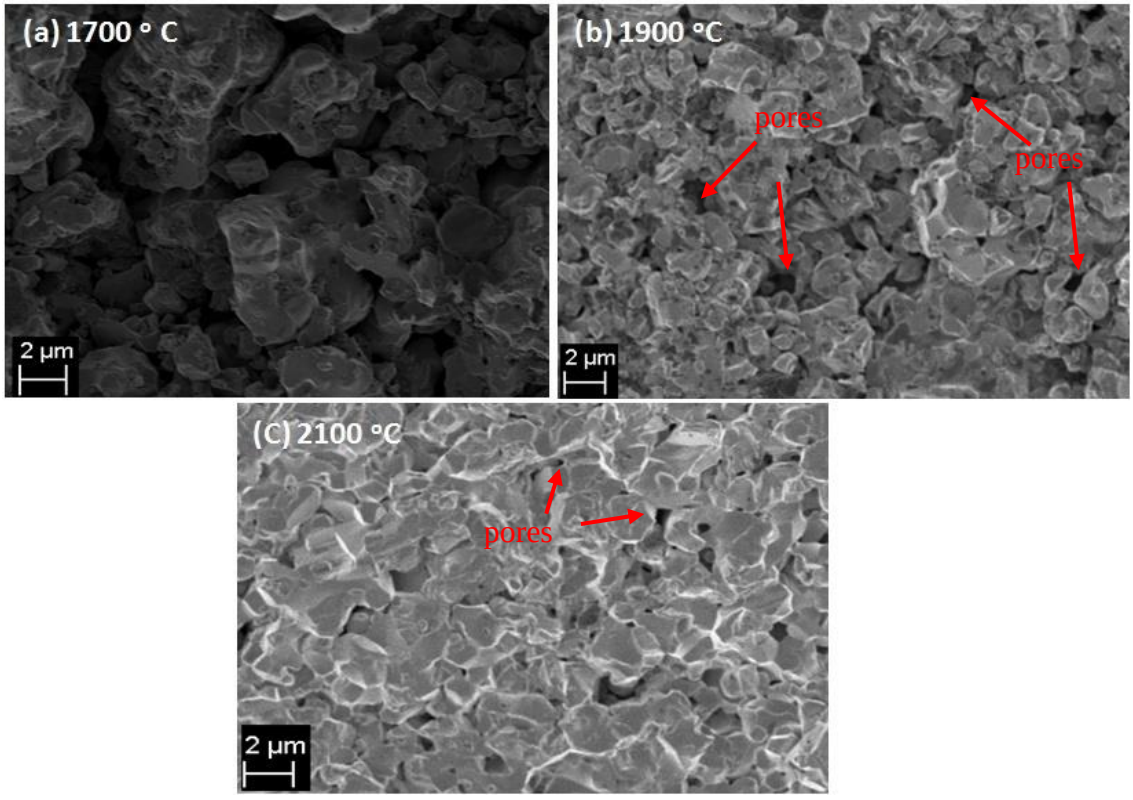


*Figure 6-12: SEM micrographs of (a) ZrC ceramic sintered at 1700 °C, (b) at 1900 °C and (c) at 2100 °C by SPS.*

### 6.3 Ir thin film on ZrC polished

Thin Ir films were deposited by electron beam deposition at room temperature onto ZrC substrates sintered at 2100 °C. The mean thickness of the Ir film was found to be about 70

nm. This substrate was chosen due to its inherent attractive properties such as low porosity, higher density and hardness.

### 6.3.1 Grazing incident X-ray diffraction (GIXRD)

The GIXRD patterns of the as-deposited Ir-ZrC sample and after annealing at 600 °C, 800 °C for 2 hours are shown in Figure 6-13. The XRD patterns of the as-deposited sample showed the presence of ZrC and Ir phases. Three Ir peaks can be observed at 2θ positions of 40.87°, 47.68° and 84.21° indexed to (111), (200) and (311) planes respectively. This indicates that an Ir film was successfully deposited on the ZrC substrate surface and it had a polycrystalline structure. The Ir peaks are broad and have low intensities. This might be due to the nano-particle size effect which causes broadening of diffraction peaks.

Annealing the Ir-ZrC samples at 600 °C for 2h showed four peaks from the unreacted Ir film at 40.87°, 47.68°, 69.58° and 84.21° indexed to the (111), (200), (220) and (311) planes respectively. A new Ir diffraction peak appeared at 69.58° 2θ position and at (220) plane. The appearance of this new Ir peak after annealing at this temperature indicates that the crystallinity of Ir thin film had improved.

The peaks at 65.65° and 88.14° 2θ positions are attributed to the $Ir_2Zr$ phase. The presence of these peaks indicates that a reaction between Ir and Zr responsible for the formation of $Ir_2Zr$ had occurred at 600 °C. This was the only reaction product formed at this temperature.

After annealing at 800 °C for time 2 h, Ir peaks at 2θ positions of 40.87°, 47.68° and 84.21° and a peak indexed to IrZr at 69.35° 2θ position were observed. This implies that a fraction of the $Ir_2Zr$ phase had transformed into IrZr thus resulting in a decrease in $Ir_2Zr$ peak intensity. The possible reactions are represented by Equations (6.9) and (6.10) below:

$$ZrC + 2Ir \rightarrow Ir_2Zr + C \quad (6.9)$$

$$Ir_2Zr + ZrC \rightarrow 2IrZr + C \quad (6.10)$$

After annealing at 600 °C and 800 °C for 2 h there was an additional peak at 48.63° from single crystal diffraction. The Debye-Scherrer diffraction rings from sample annealed at 600 °C in Figure 6-13(b) shows some bright spots which suggest the presence of relatively large grains in the sample (i.e. large grains in relation to the beam size of ~1 mm diameter). The position of the single crystal diffraction peak (48.63°) is not necessarily at the same position as those coming from polycrystalline diffraction patterns. If this is close to the ring as it is the case with this sample, see the arrow in the image in Figure 6-13(b), upon integration it might show an additional peaks.

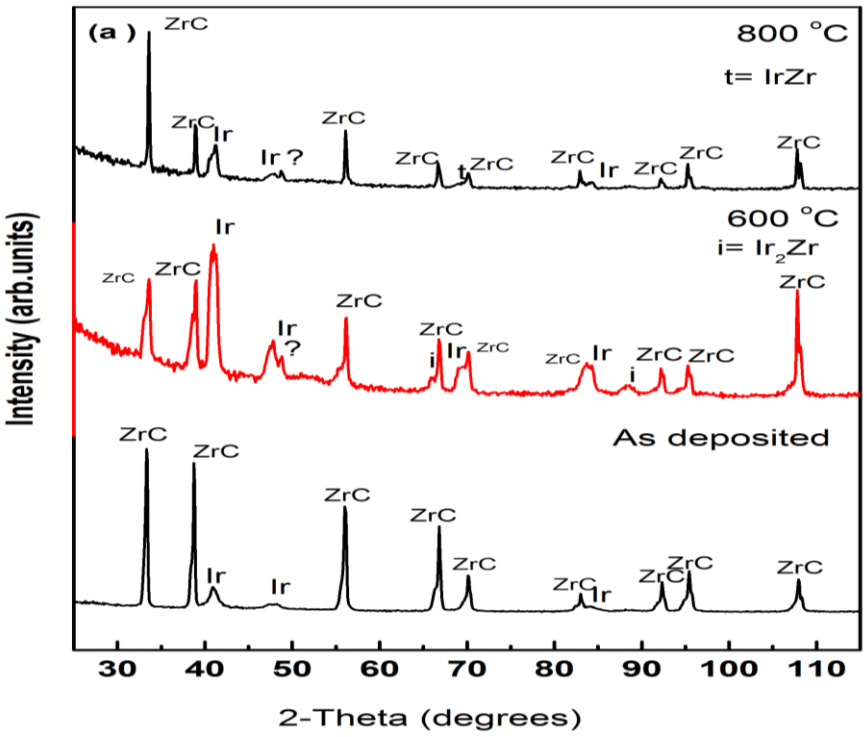

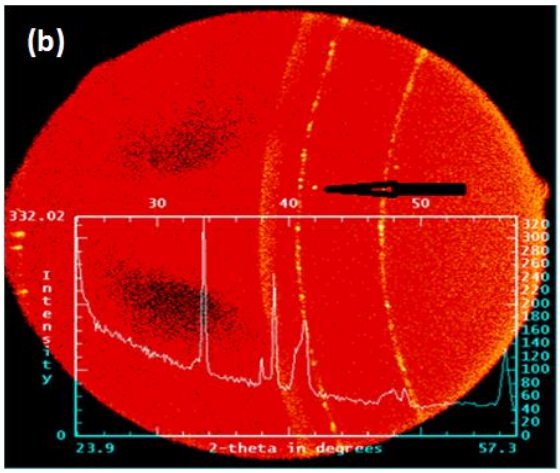


*Figure 6-13: (a) Grazing incidence X-ray diffraction patterns of as-deposited Ir-ZrC sample and after annealing at 600 °C and 800 °C in vacuum. (b) The corresponding Debye-Scherrer rings for sample annealed at 600 °C showing single crystal diffraction 2θ position of 48.63°.*

The reaction between Ir and ZrC and the enthalpies of reaction are given in Table 6-5. The reaction enthalpies were calculated using enthalpies of formation of ZrC and Ir-Zr system taken from reference [50]. From Table 6-5, it can be seen that the enthalpies of reaction (1) to (3) are negative, while reactions (4) to (6) are positive.

Reaction (1) between Ir and ZrC to form $Ir_2Zr$ is thermodynamically favoured at temperature 600 °C since it has the highest negative reaction enthalpy. This was the initial phase to form and only phase observed to form in this study after annealing at 600 °C. There are no previous studies which report the formation of $Ir_2Zr$ from the interaction between Ir and ZrC at low temperature.

Reaction (3) to form IrZr which has a lower negative enthalpy of reaction (-8.6 $kJ.mole^{-1}$·at) occurred at 800 °C. The appearance of this phase in the Ir-ZrC reaction zone could be due to diffusion kinetics of the reactants limiting the effective concentration to form $Ir_2Zr$. The IrZr phase has not been previously observed to form after the reaction between Ir and ZrC at high temperatures.

However, reaction (2) to form $Ir_3Zr$ whose reaction enthalpy is lower than reaction (1), has been reported by Criscione et al. [51] to form after annealing at 1200 °C and by Strife et al. [52] between 1650 °C and 2127 °C. The peak from $Ir_3Zr$ phase diffraction was not observed within the sensitivity of GIXRD. This implies that the $Ir_3Zr$ phase forms at temperatures higher than 800 °C after a reaction between IrZr and Ir. Reactions (4), (5) and (6) have positive enthalpies of reaction, so they are not expected to proceed at low or high temperatures.

*Table 6-5: Possible reactions between Ir and ZrC and the calculated reaction enthalpies.*

| **Reaction** | **$\Delta H_R^0$ (kJmole$^{-1}$·at)** |
|---|---|
| 1. $ZrC + 2Ir \rightarrow Ir_2Zr + C$ | -24.3 |
| 2. $ZrC + 3Ir \rightarrow Ir_3Zr + 2C$ | -22.7 |
| 3. $ZrC + Ir \rightarrow IrZr + C$ | -8.6 |
| 4. $3ZrC + Ir \rightarrow IrZr_3 + 3C$ | 48.4 |
| 5. $2ZrC + Ir \rightarrow IrZr_2 + 2C$ | 27.8 |
| 6. $5ZrC + 3Ir \rightarrow Ir_3Zr_5 + 5C$ | 17.6 |

### 6.3.2 Scanning electron microscopy (SEM)

The changes in the surface morphology of the as-deposited and annealed samples were monitored by SEM analysis. The SEM micrographs of Ir-ZrC sample surface after annealing from 600 °C to 800 °C for 2h in vacuum are shown in Figure 6-14. The surface of the as-deposited sample was included for comparison. Figure 6-14(a) depicts the surface of Ir film deposited onto ZrC sintered at 2100 °C. The surface of the Ir film shows some distributed interconnected pores. These pores are influenced by the ZrC substrate surface nature which was discussed previously in section 6.2.5. The surface has an agglomerated granule structure which might be due to the underlying ZrC.

The SEM micrographs of the Ir-ZrC samples annealed at 600 °C and 800 °C (see Figure 6-14(b) and (c)), show that some form of surface rearrangement which led to a reduction in the number of pores and less rough surface. The micrographs also show regions of necking between adjacent grains. This smoothening of the surface might be due to surface diffusion of Ir or the formation of the different phases ($Ir_2Zr$ and IrZr) forming at temperature 600 °C and 800 °C, as shown in the XRD results discussed in the previous section, where Ir reacted with ZrC to form respectively. The reactions to form $Ir_2Zr$ and IrZr seem to promote agglomeration of the surface particles.

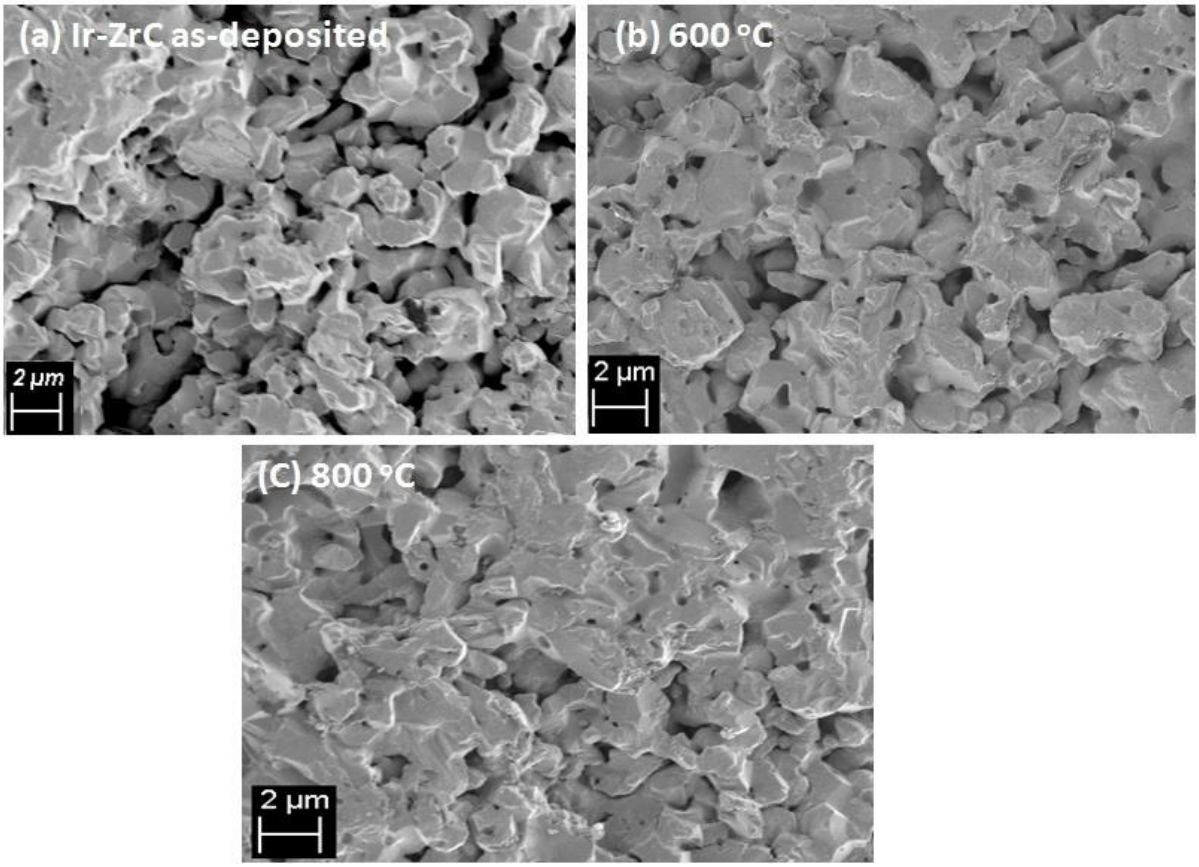


*Figure 6-14: SEM micrographs of (a) Ir on ZrC as- deposited; vacuum annealed samples for 2h at (b) 600 °C, and (c) 800 °C.*

## References


[1] J.G. Kim, S.J. Park, J.Y. Park, D.J. Choi, The effect of temperature on the growth and properties of chemical vapor deposited ZrC films on SiC-coated graphite substrates, Ceram. Int. 41 (2015) 211–216.

[2] J.H. Kwon, S.G. Yoon, Preparation of Pt thin films deposited by metalorganic chemical vapor deposition for ferroelectric thin films, Thin Solid Films. 303 (1997) 136–142.

[3] J.H. Park, C.H. Jung, D.J. Kim, J.Y. Park, Temperature dependency of the LPCVD growth of ZrC with the ZrCl4–CH4–H2 system, Surf. Coatings Technol. 203 (2008) 324–328.

[4] S. Biira, P.L. Crouse, H. Bissett, T.T. Hlatshwayo, J.H. Van Laar, J.B. Malherbe, Design and fabrication of a chemical vapour deposition system with special reference to ZrC layer growth characteristics, J. South. African Inst. Min. Metall. 117 (2017) 931–938.

[5] Q. Liu, L. Zhang, L. Cheng, Y. Wang, Morphologies and growth mechanisms of zirconium carbide films by chemical vapor deposition, J. Coatings Technol. Res. 6 (2009) 269–273.

[6] Z.Q. Li, C.J. Lu, Z.P. Xia, Y. Zhou, Z. Luo, X-ray diffraction patterns of graphite and turbostratic carbon, Carbon N. Y. 45 (2007) 1686–1695.

[7] L. Wendy, H. Mao, J. Peter, P. Thomas, Bonding changes in compressed superhard

graphite, Science. 302 (2003) 425–427.

[8] Z. Wang, Y. Zhao, K. Tait, X. Liao, D. Schiferl, C. Zha, R.T. Downs, J. Qian, Y. Zhu, T. Shen, A quenchable superhard carbon phase synthesized by cold compression of carbon nanotubes, Proc. Natl. Acad. Sci. U. S. A. 101 (2004) 13699–13702.

[9] L.B. Mccusker, R.B. Von Dreele, D.E. Cox, D. Louer, P. Scardi, Rietveld refinement guidelines, J. Appl. Crystallogr. 32 (1999) 36–50.

[10] T.M. Besmann, Thermochemical assesment of oxygen gettering by SiC and ZrC in PuO2-x in TRISO fuel, J. Nucl. Mater. 397 (2010) 69–73.

[11] R.E. Bullock, J.L. Kaae, Performance of coated UO2 particles gettered with ZrC, J. Nucl. Mater. 115 (1983) 69–83.

[12] Y. Wang, Q. Liu, J. Liu, L. Zhang, L. Cheng, Deposition mechanism for chemical vapor deposition of zirconium carbide coatings, J. Am. Ceram. Soc. 1252 (2008) 1249–1252.

[13] K. Fukuda, K. Ikawa, F. Kobayashi, K. Iwamoto, Microstructure of vapor-deposited ZrC-C alloy, J. Nucl. Mater. 56 (1975) 243–245.

[14] W. Sun, X. Xiong, B.Y. Huang, G.D. Li, H.B. Zhang, P. Xiao, Z.K. Chen, X.L. Zheng, Preparation of ZrC nano-particles reinforced amorphous carbon composite coating by atmospheric pressure chemical vapor deposition, Appl. Surf. Sci. 255 (2009) 7142–7146.

[15] S. Biira, P.L. Crouse, H. Bissett, B.A.B. Alawad, T.T. Hlatshwayo, J.T. Nel, J.B. Malherbe, Optimisation of the synthesis of ZrC coatings in a radio frequency induction-heating chemical vapour deposition system using response surface methodology, Thin Solid Films. 624 (2017) 61–69.

[16] D. Kim, M.J. Ko, J.Y. Park, M.S. Sung, W. Kim, Influence of free carbon on the characteristics of ZrC and deposition of near-stoichiometric ZrC in TRISO coated particle fuel, J. Nucl. Mater. 451 (2014) 97–103.

[17] S. Biira, P.L. Crouse, H. Bissett, T.T. Hlatshwayo, E.G. Njoroge, J.T. Nel, T.P. Ntsoane, J.B. Malherbe, The role of ZrCl4 partial pressure on the growth characteristics of chemical vapour deposited ZrC layers, Ceram. Int. 43 (2017) 15133–15140.

[18] Y. Katoh, G. Vasudevamurthy, T. Nozawa, L.L. Snead, Properties of zirconium carbide for nuclear fuel applications, J. Nucl. Mater. 441 (2013) 718–742.

[19] A.C. Ferrari, J. Robertson, Interpretation of Raman spectra of disordered and amorphous carbon, Phys. Rev. B. 61 (2000) 14095–14107.

[20] S. Pellegrino, L. Thomé, A. Debelle, S. Miro, P. Trocellier, Radiation effects in carbides: TiC and ZrC versus SiC, Nucl. Instruments Methods Phys. Res. Sect. B-Beam Interact. with Mater. Atoms. 327 (2014) 103–107.

[21] K. Tamura, T. Ogawa, K. Fukuda, The oxidation behavior of ZrC coating and powder studied by laser Raman spectroscopy and X-ray diffraction, J. Nucl. Mater. 175 (1990) 266–269.

[22] R.J. Nemanich, S.A. Solin, First and second order Raman scattering from finite-sized crystals of graphite, Phys. Rev. B. 20 (1979) 392–401.

[23] A. Sadezky, H. Muckenhuber, H. Grothe, R. Niessner, U. Poschl, Raman microspectroscopy of soot and related carbonaceous materials: Spectral analysis and structural information, Carbon. 43 (2005) 1731–1742.

[24] Y. Wang, D.C. Alsmeyer, R.L. Mccreery, Raman spectroscopy of carbon materials: structural basis of observed spectra, Chem. Mater. (1990) 557–563.

[25] T.R. Ravindran, B.R. Jackson, J. V Badding, UV Raman Spectroscopy of Single-Walled Carbon Nanotubes, Chem. Mater. (2001) 4187–4191.

[26] M.S. Dresselhaus, G. Dresselhaus, P.C. Eklund, D.D.L. Chung, Lattice vibration in graphite and intercalation compounds of graphite, Mater. Sci. Eng. 31 (1977) 141–152.

[27] C.. Neugebauer, Condensation, Nucleation and Growth of Thin Films, in: H. Frey, H.R. Khan (Eds.), Handb. Thin-Film Technol., Springer, New York, 1970.

[28] C.V. Thompson, Structure evolution during processing of polycrystalline films, Annu. Rev. Mater. Sci. 30 (2000) 159–190.

[29] M. Zinke-Allmang, Phase separation on solid surfaces: nucleation, coarsening and coalescence kinetics, Thin Solid Films. 346 (1999) 1–68.

[30] J. Stavans, The evolution of cellular structures, Reports Prog. Phys. 56 (1993) 733–789.

[31] B.Y.W.K. Burton, N. Cabrera, F.C. Frank, The Growth of Crystals and the

Equilibrium Structure of their Surfaces, Philos. Trans. R. Soc. London. 243 (1951) 299–358.

[32] P. Beck, Annealing of cold worked metals, Adv. Phys. 3 (1954) 245–324.

[33] S. Biira, B.A.B. Alawad, H. Bissett, J.T. Nel, T.P. Ntsoane, T.T. Hlatshwayo, P.L. Crouse, J.B. Malherbe, Influence of the substrate gas-inlet gap on the growth rate, morphology and microstructure of zirconium carbide films grown by chemical vapour deposition, Ceram. Int. 43 (2017) 1354–1361.

[34] C. Liu, B. Liu, Y. Shao, Z. Li, C. Tang, Preparation and Characterization of Zirconium Carbide Coating on Coated Fuel Particles, J. Am. Ceram. Soc. 90 (2007) 3690–3693.

[35] D. Kim, Y.B. Chun, M.J. Ko, H. Lee, M. Cho, J.Y. Park, W. Kim, Microstructure evolution of a ZrC coating layer in TRISO particles during high-temperature annealing, J. Nucl. Mater. 479 (2016) 93–99.

[36] M.J. Matthews, M.A. Pimenta, G. Dresselhaus, M.S. Dresselhaus, M. Endo, Origin of Dispersive Effects of the Raman D Band in Carbon Materials, Phys. Rev. B. 59 (1999) R6585–R6588.

[37] G.A. Zickler, B. Smarsly, N. Gierlinger, H. Peterlik, O. Paris, A reconsideration of the relationship between the crystallite size La of carbons determined by X-ray diffraction and Raman spectroscopy, Carbon. 44 (2006) 3239–3246.

[38] B.D. Cullity, Elements of X-ray diffraction, Addison-Wesley, Reading, 1977.

[39] G. Wulff, Zur Frage der Geschwindigkeit des Wachstums und der Auflösung der Krystallflagen, Zeitschrift Fur Krist. 34 (1901) 449–530.

[40] C. V Thompson, Coarsening of particles on a planar substrate: Interface anisotropy and application to grain growth in this films, Acta Mater. 36 (1988) 2929–2934.

[41] G. Ehrlich, F.G. Hudda, Atomic View of Surface Self- Diffusion: Tungsten on Tungsten, J. Chem. Phys. 44 (1966) 1039–1049.

[42] R.L. Schwoebel, Step Motion on Crystal Surfaces. II, J. Appl. Phys. 40 (1969) 614–618.

[43] J.W. Evans, P.A. Thiel, M.C. Bartelt, Morphological evolution during epitaxial thin film growth: Formation of 2D islands and 3D mounds, Surf. Sci. Rep. 61 (2006) 1–128.

[44] J.B. Malherbe, Bombardment-induced topography on semiconductor surfaces, in: P. Chakraborty (Ed.), Ion Beam Anal. Surfaces Interfaces Condens. Matter Syst., Nova Science, New York, 2003: pp. 357–400.

[45] C.H. Chu, M.H. Hon, Morphology and IR transmission of β-SiC synthesized by chemical vapour deposition, J. Ceram. Soc. Japan. 98 (1993) 95–98.

[46] D. Sciti, S. Guicciardi, M. Nygren, Spark plasma sintering and mechanical behaviour of ZrC-based composites, Scr. Mater. 59 (2008) 638–641.

[47] D. Sciti, M. Nygren, Spark plasma sintering of ultra refractory compounds, J. Mater. Sci. 43 (2008) 6414–6421.

[48] S.K. Sun, G.J. Zhang, W.W. Wu, J.X. Liu, T. Suzuki, Y. Sakka, Reactive spark plasma sintering of ZrC and HfC ceramics with fine microstructures, Scr. Mater. 69 (2013) 139–142.

[49] X. Wei, C. Back, O. Izhvanov, O.L. Khasanov, C.D. Haines, E.A. Olevsky, Spark plasma sintering of commercial zirconium carbide powders: Densification behavior and mechanical properties, Materials (Basel). 8 (2015) 6043–6061.

[50] H. Ran, Z. Du, Thermodynamic assessment of the Ir--Zr system, J. Alloys Compd. 413 (2006) 101–105.

[51] J.M. Criscione, R.A. Mercuri, E.P. Schram, A.W. Smith, H.F. Volk, High temperature protective coatings for graphite: Part II, Wright Patterson AFB, OH, 1964.

[52] J.R. Strife, J.G. Smeggil, W.L. Worrell, Reaction of Iridium with Metal Carbides in the Temperature Range of 1923 to 2400 K, J. Am. Ceram. Soc. 45 (1990) 838–845.

# Chapter 7. Conclusions and Future work

## 7.1 Conclusions

Two methods were used in this study to synthesise ZrC, chemical vapour deposition (CVD) and spark plasma sintering (SPS). Firstly this study focused on a deposition process for the preparation ZrC layers from $ZrCl_4$-Ar-$CH_4$-$H_2$ precursors, using induction thermal CVD at atmospheric pressure. A vertical wall thermal CVD reactor was successfully built and used for the deposition of ZrC layers. This CVD reactor has the capability of depositing a variety of layers for various research and industrial applications. The process parameters and the CVD reactor geometry were designed to control the growth and quality of ZrC layers. $ZrCl_4$-$CH_4$-$H_2$-Ar mixtures were used for the deposition of ZrC layers. $ZrCl_4$vapour flow control was achieved by careful designing of the CVD vaporiser system and controlling the argon carrier gas flow and the vaporisation temperature. The amount of $ZrCl_4$ loaded and its surface area exposed to the carrier gas was also carefully managed. The ZrC layers were successfully deposited on graphite substrates at temperatures ranging from 1250 °C to 1450 °C in steps of 50 °C. The deposited ZrC layers were then studied according to their deposition condition, namely substrate temperature, precursor flow ratios and partial pressures, reactor geometry and deposition time.

The deposited layers were characterised by X-ray diffraction (XRD), (EDS), Raman Spectroscopy and Scanning Electron Microscopy (SEM).The deposition rate exponentially increased with temperature and its activation energy showed that the deposition mechanism was controlled by surface reactions. The XRD spectra together with a Rietveld analysis showed that the layers consisted of the ZrC with graphite and carbon in the layers.The 26.6° graphite peak overlapped with another graphite peak at about 26.2°.The latter indicates that the graphite inclusions were under high stress. Since ZrC is not Raman active, the Raman

spectra showed only D and G peaks of the excess carbon in the deposited layers. The presence of these two peaks shows that the graphite was highly disordered.

From the XRD spectra it was found that the ZrC lattice parameter remained constant at 0.46838 ± 0.00091 nm for all deposition temperatures. However, the average size of ZrC crystallites (and the graphite crystallites) depended on the deposition temperature and varied between 19.19 nm to 26.18 nm. A comparison of the graphite crystallite sizes determined by XRD and Raman showed that the constant in Tuinstra-Koenig formula must change from its normally accepted value to get agreement between the two sets of average size data.

The texture coefficients of the (111), (200) and (220) planes were determined for all deposition temperatures. These coefficients indicated preferred orientation for all three planes at the lower temperatures, i.e. from 1250 °C to 1400°C. At 1450 °C only the (220) plane grew preferentially. The results were explained in terms of standard crystal growth theory where minimization of the Gibbs free energy is the driving force. This is confirmed by SEM investigations of the layer surfaces at the different deposition temperatures. The morphology of the as-deposited layers was influenced by the deposition temperature. Clustering of the crystals occurred resulting in a cauliflower appearance on the surface.

Secondly ZrC was synthesised by SPS at various temperatures. The phase and microstructure evolution after the ZrC sintering process at 1700 $^{o}$C, 1900 $^{o}$C and 2100 °C was investigated. The relative density of ZrC prepared by SPS was seen to increase as sintering temperature increased. The grain size of ZrC substrates was calculated and it was found to increase as the sintering temperature increased. The increasing in grain size led to increase in hardness as the sintering temperature increased. The preferred orientation of the ZrC sintered at 1700 °C to 2100 °C was found to be the (200) plane. The surface of the as-sintered samples was observed to vary with sintering temperatures. The ZrC surface was generally uneven,

heterogeneous and had agglomerated granules with the number of pores decreasing with temperature.

Lastly, the interactions between Ir thin films and ZrC was also performed to investigate viability of Ir protective layers on ZrC for nuclear industry applications. The solid-state interactions, phase formation, and surface morphology were investigated. The GIXRD pattern of the as-deposited sample showed broad Ir peaks indicating that the deposited Ir film was polycrystalline. Interaction between Ir and ZrC was observed after annealing at 600 °C and 800 °C with the formation of two reaction phases, that is, $Ir_2Zr$ and IrZr respectively. SEM images showed that the Ir film was composed of small agglomerated clusters, deposited on ZrC. After annealing at 600 $^{o}$C and 800 $^{o}$C, the crystallites coalesced to form larger crystals.

**7.2 Future work**

In future to optimize and improve the processing of chemical vapour deposition (CVD) to obtain high quality ZrC layers, the following studies are recommended below:

- Computer simulations of the relevant physical phenomena that is difficult to measure.
- Achieving of the temperature distribution inside the CVD reactor and how it can be influenced by changes in induction coil frequency, power input to the coil and graphite reactor chamber thickness.
- A comparison of ZrC layer characteristics deposited in a hot-wall and a cold-wall reaction chamber, and a vertical-wall and a horizontal-wall reaction chamber to ascertain which reactor type can produce quality ZrC layers.
- To improve the synthesis of ZrC by spark plasma sintering (SPS) the time must be increased 20 minutes and the pressure must be reduced to 40 MPa.
- A comparison of ZrC layer characteristics after synthesis by spark plasma sintering (SPS), hot-pressing (HP) and CVD.

- Annealing Ir-ZrC samples at high temperatures ranging between 1000 $^{o}$C to 1300 $^{o}$C investigate the interaction between Ir thin film and ZrC.
- Annealing ZrC samples and Ir-ZrC in air at low temperatures such as 500 $^{o}$C to investigate oxidation and formation of $ZrO_2$.

# Appendix

The results of this investigation were presented in both international and national conferences and a number of peer review articles were published. This chapter lists all article and conference contributions from this investigation.

**Publications**

[1]**B.A.B Alawad**, S. Biira, H. Bissett, J.T. Nel, T.T. Hlatshwayo, P.L. Crouse, andJ.B. Malherbe, *"*CVD Growth of ZrC Layers at Different Temperatures*."* Physics and Materials Chemistry, Vol 4 (2016) pp.6-9.

[2]S. Biira, **B.A.B. Alawad**, H. Bissett, J.T. Nel, T.P. Ntsoane, T.T. Hlatshwayo, P.L. Crouse, J.B. Malherbe, *"*Influence of the substrate gas-inlet gap on the growth rate, morphology and microstructure of zirconium carbide films grown by chemical vapour deposition*"*, Ceramics International Vol 43 (2017) pp.1354-1361.

[3]S. Biira, P.L. Crouse, H. Bissett, **B.A.B. Alawad**, T.T. Hlatshwayo, J.T. Nel, J.B. Malherbe, "Optimisation of the synthesis of ZrC coatings in an RF induction-heating CVD system using surface response methodology*"*, Thin Solid FilmsVol 624 (2017) pp.61-69.

[4]S. Biira, **B.A.B. Alawad**, H. Bissett, J.T. Nel, T.T. Hlatshwayo, J.B. Malherbe, Deposition of ZrC layers in a vertical wall CVD system, *(*Proceedings of SAIP2016).

[5] **B.A.B. Alawad**, E.G. Njoroge, T.T. Hlatshwayo, T.T. Thabethe, M.J. Legodi, T.P. Ntsoane, J.B. Malherbe, Phase formation between Iridium thin films and zirconium carbide prepared by spark plasma sintering at relatively low temperatures,2018 Open Innovations Conference (OI), pp. 265 – 270.

[6] J.B. Malherbe, **B.A.B. Alawad**, S. Biira, T.T. Hlatshwayo, H. Bisset, T.P. Ntsoane , M. Mlambo, E.G. Njoroge, P.L. Crouse, Investigation of the temperature-dependent composition and morphology of ZrC layers deposited by CVD.

**Conferences**

[1] Advanced Metals Initiative (AMI), nuclear materials development network conference 2015, Port Elizabeth, South Africa October 28- 30, 2015. (Poster presentation).

[2]South African institute of Physics (SAIP), 2016, University of Cape town, South Africa 4-8 July 2016. (Posterpresentation).

[3] Advanced Metals Initiative (AMI), Ferrous metals conference 2016, Durban, South Africa October 17- 20 2016. (Invited delegate).

[4] IEEE 2018 Open Innovations Conference, University of Witwatersrand, Johannesburg, South Africa October 3 - 5, 2018. (Oral talk).